Epitaxial nanotemplates for strain modulated carrier confinement in Silicon

A Dissertation

Presented to

the faculty of the School of Engineering and Applied Science

University of Virginia

in partial fulfillment

of the requirements for the degree

Doctor of Philosophy

by

Christopher W. Petz

May

2012

APPROVAL SHEET

The dissertation

is submitted in partial fulfillment of the requirements

for the degree of

Doctor of Philosophy

AUTHOR

The dissertation has been read and approved by the examining committee:

Jerrold A. Floro
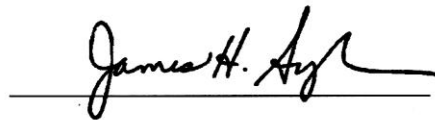
Advisor

James M. Howe

Lloyd R. Harriott

Petra Reinke

Jiwei Lu

Accepted for the School of Engineering and Applied Science:

Dean, School of Engineering and Applied Science

May

2012

Abstract

The fundamental goal of this thesis is to characterize and assess the effects of strain, chemistry, and growth orientation on the structure of complex epitaxial heterostructures. In this dissertation, we discuss artificial patterning, formation, and encapsulation of Ge quantum dots (QDs).

Precise spatial ordering of QDs may enable predictable quantum states due to direct exchange interactions of confined carriers. The realization of anticipated quantum states may lead to unique functionalities such as cluster qubits and spintronic bandgap systems. In order to define exemplary quantum architectures, one must develop control over QD size and spatial arrangement on the sub-35 nm length scale. We employ fine-probe electron-beam irradiation to locally decompose ambient hydrocarbons onto a bare Si (001) surface. These carbonaceous patterns are annealed in UHV, forming ordered arrays of nanoscale SiC precipitates that may template subsequent epitaxial Ge and Si growth to form ordered hybrid Ge/SiC or Si/SiC QD arrays on ultra-small length scales.

First, we investigate the templated feature evolution during UHV annealing and subsequent Ge epitaxial overgrowth to identify key mechanisms that must be controlled in order to preserve pattern fidelity and reduce broadening of the nanodot size distribution. We find that to obtain the narrow size distribution required for spintronic applications, one must precisely control the total thermal budget.

Next, we show that sub-10 nm 3C-SiC nanodots form, in cube-on-cube epitaxial registry with the Si substrate. The SiC nanodots are fully relaxed by misfit dislocations, and exhibit small lattice rotations with respect to the substrate. Ge overgrowth at elevated

deposition temperatures, followed by Si capping, results in expulsion of the Ge from SiC template sites due to the large chemical and lattice mismatch between Ge and C. Preliminary magnetotransport measurements of our templated nanostructures show significant promise for local strain-based confinement of carriers in ordered arrays.

Lastly, we have investigated low temperature epitaxial breakdown of inhomogeneously strained Si capping layers. By growing Si films on coherently strained GeSi quantum dot surfaces, we differentiate effects of surface roughness, strain, and growth orientation on the mechanism of epitaxial breakdown. Using atomic force microscopy and high resolution cross-sectional transmission electron microscopy we find that while local lattice strain up to 2% has a negligible effect, growth on higher-index facets such as {113} significantly reduces the local breakdown thickness. Nanoscale growth mound formation is observed above all facet orientations. Since diffusion lengths depend directly on the surface orientation, we relate the variation in epitaxial thickness to low temperature stability of specific growth facets and on the average size of kinetically limited growth mounds.

These experiments elucidate two technologically significant results: (1) a metric for selection of growth temperature in order to achieve high epitaxial quality Si encapsulation and (2) SiC based patterning routes can provide modulated carrier confinement potentials on relevant length scales for realization of high quality spintronic devices.

Acknowledgements

First and foremost, I would like to thank my advisor, Prof. Jerry Floro for his patient support, encouragement, and guidance throughout my graduate career. His openness for spontaneous, lengthy science discussion was invaluable for my rapid development as a scientist and as a critical thinker. Prof. Floro's genuine excitement for understanding nature and guiding the education thereof is truly inspirational.

I also thank my committee: Prof. Reinke, Prof. Liu, Prof. Howe, and Prof. Harriott, for their continued guidance and critical questioning of my research over the last five years.

I acknowledge our collaborators at the University of Pittsburgh, Prof. Jeremy Levy, and Dongyue Yang for directly facilitating our research, and guiding fruitful Skype discussions. Additional research support at NIST and the Virginia Tech NCFL was also very useful.

I thank the entirety of the University of Virginia Department of Materials Science and Engineering for the genuine welcoming vibe shared between all faculty, staff and students. The cohesive nature of this department is a very positive environment capable of fostering the development of top-notch scientists and engineers. In particular, I thank my closest colleagues, Dr. Kevin West, Dr. Jeremy Graham, Dr. Eric Rouya, Dr. Tabitha Apple, Dr. Wenjing Yin, Dr. Prakash Palaniswamy, Dr. Rupalee Mulay, Dr. James Wollmersauser, Dr. Kiril Simov, Joseph Kassim, Priya Ghatwai, Copeland Kell, Chris Duska, Chris Nolph, Ryan Comes, Brad Richards, and Harmonie Saholov.

And lastly, I greatly appreciate all of my friends and family, it was their support that provided the endurance to pursue a decade of higher education.

List of Figures

List of Terms and Symbols

a - acceleration or lattice parameter
A - Area or exchange coefficient
AFM - Atomic force microscopy
B - Magnetic field or wavefunction decay length
CBED - Convergent beam electron diffraction
CCD - Charge coupled device
D - Diameter
d - Interplanar spacing
DC - Direct current
DR - Dilution refrigerator
E - energy
ε - lattice mismatch
E-S - Erlich-Schwoebel barrier
EB - surface binding energy
E_{coh} - Cohesive film strain
E_{ex} - Exchange energy
EBID - Electron beam induced deposition
EBL - Electron beam lithography
F - Force
FCC - Face center cubic
FE - Field emission
FFT - Fast fourier transform
FIB - Focused ion beam
G - Shape factor
γ - Surface energy
h - height
HAADF - High angle annular dark field
HCP - Hexagonal close packed
h_{epi} - Critical epitaxial thickness
HRTEM - High resolution transmission electron microscopy
I - Current
iFFT - Inverse fast fourier transform
L - Nanodot separation
M - Biaxial modulus
m - mass
MBE - Molecular beam epitaxy
MD - Molecular dynamics
MFM - Magnetic force microscopy
N - Number of particles

P - Pressure
PBC - Periodic boundary conditions
PC - Phase contrast
PPMS - Physical property measurement system
PVD - Physical vapor deposition
QCM - Quartz crystal microbalance
QD - Quantum dot
QW - Quantum well
r - radius
R_g - deposition rate
RHEED - Reflection high energy electron diffraction
S-K - Stranski-Krastanov
S-W - Stillinger-Weber
SEM - Scanning electron microscope
SIMS - Secondary ion mass spectroscopy
STEM - Scanning transmission electron microscope
t - time
TEM - Transmission electron microscope
TRIM - Transport of Ions in Matter
UHV - Ultra high vacuum
V - Voltage, velocity, or volume
W - Cohestive elastic energy density or width
WL - Wetting layer
XTEM - Cross sectional transmission electron microscopy
Z - Pit depth

Brief Author Biography

Christopher W. Petz is originally from Tracy, CA. He received his Bachelors of Science, with Distinction in Materials Science and Engineering at the University of Washington in 2007. At UW, he completed undergraduate research under the advisement of Prof. Kannan M. Krishnan working on the development of aqueous Co nanodisks and incorporation with semiconducting polymer films.

Immediately following, Chris commenced his graduate work at the University of Virginia in 2007, completing his Ph.D. in 2012 while working in the HyperMBE laboratory of Prof. Jerrold A. Floro. A list of publications and presentations to-date is given below.

Publications:

1. C.W. Petz,D. Yang, J. Levy, J.A.. Floro. "Epitaxial Silicon encapsulation of highly misfitting SiC/Si(001) nanodots". *Appl. Phys. Lett.* In progress. (2012)

2. C.W. Petz,D. Yang, J. Levy, J.A.. Floro. "Thermal stability and formation of 2D ordered SiC/Si(001) nanodots". *J. Mat. Res.* Submitted. (2012)

3. C.W. Petz,D. Yang, J. Levy, J.A.. Floro. "Structure of Si-capped Ge/SiC/Si(001) epitaxial nanodots: implications for quantum dot patterning". *Appl. Phys. Lett.* **100**, 141603. (2012)

4. C.W. Petz and J. Floro. "Inhomogeneous low temperature epitaxial breakdown during Si overgrowth of GeSi quantum dots". *J. Appl. Phys.* **110**, 023508 (2011).

5. P.E. Hopkins, J. C. Duda, C. W. Petz, J. A. Floro. "Controlling thermal interface conductance through quantum dot roughening". *Phys. Rev. B.* **84**, 035438 (2011)

6. S. Light, C. Petz, I.Tsyba, P. Baluswamy, B. Rolfson. "Effects of reticle birefringence on 193nm lithography." *Proc. SPIE,* **6520**, 65201K *(2007).*

Presentations:

1. C.W. Petz, D. Yang, J.A. Floro, J. Levy. "Structure of Si-capped Ge/SiC/Si(001) epitaxial nanodots: implications for quantum dot patterning". *Oral presentation at 2012 Spring Materials Research Society Meeting*, San Francisco, CA, 10 April 2012.

2. C.W. Petz, D. Yang, J.A. Floro, J. Levy. "Heteroepitaxial growth of Ge quantum dots on EBL patterned SiC nanoprecipitates with sub-35 nm spacing". *Oral presentation at 2011 American Vacuum Society Meeting*, Nashville, TN, 2 November 2011.

3. C.W. Petz, D. Yang, J.A. Floro, J. Levy. "Directed self-assembly of ultrasmall Ge quantum dots with sub-35 nm spacing for quantum information processing". *Oral presentation at 2010 Materials Research Society Fall Meeting*, Boston, MA, 2 December 2010.

4. C.W. Petz, R. Comes, A. Ontman, S. Hull, J. Floro. ""Making Stuff" in Central Virginia: University of Virginia Outreach as a Part of the NOVA "Making Stuff" Series". *Oral presentation at 2010 Materials Research Society Fall Meeting*, Boston, MA, 29 November 2010.

5. C.W. Petz, P. Palanisamy, J. Duda, D. Yang, J. Levy, and J. Floro. "Surface morphological evolution during low temperature Ge homoepitaxial growth on

strained 2D and 3D Ge/Si (001) films." *Poster at North American Molecular Beam Epitaxy (NAMBE)*, Princeton, NJ, 9-12 August 2009.

6. C.W. Petz, K. Krishnan. "Soft lithography of conductive polymer mixed with aqueous magnetic nanoparticles." *Oral presentation at Mary Gates Undergraduate Research Symposium*, Seattle, WA, 18 May 2007.

7. C.W. Petz, K. Krishnan. "Synthesis and characterization of Co nanodisks and surfactant exchange." *Poster at Mary Gates Undergraduate Research Symposium*, Seattle, WA, 19 May 2006.

Awards and Funding:

1. Washington Space Grant: NASA Summer Undergraduate Research Program (SURP). (2005)

2. Outstanding UW-Materials Science and Engineering Undergraduate tuition scholarship. (2006)

3. Materials Research Society / WGBH PBS "Making Stuff" public outreach funding. (2010)

   Doris Wilsdorf Department of Materials Science outstanding student award. (2010)

Table of Contents

Chapter 1: Introduction

1.1 Goals and motivation

Miniaturization has allowed the semiconductor industry to scale computing speeds and efficiency with Moore's law for over 60 years. As we reach the finite minimum size of a single atom, quantum size effects at the nanoscale are causing well-known materials to behave differently. Although researchers continue to discover clever tricks and materials to maintain top-down device scaling (e.g. the use of interference lithography to circumvent the diffraction limit and the development of high-k dielectrics to withstand increasing heat dissipation and leakage current), we must remain vigilant for a replacement technology that may continue to advance computing power at an exponential rate. One new approach is built upon spin-based electronic (spintronic) systems [1–3], aptly named due to their exploitation of electron *spin* as the state variable. Since these alternative logic switches rely on the spin state rather than traditional non-linear current behavior, potential advantages of spintronic systems include non-volatility, increased speed, enhanced power efficiency, and (most importantly) reduced heat dissipation.

As one might expect, materials meant to manipulate the properties of single electrons are incredibly sensitive to defects and processing conditions. Using the nanofabrication techniques introduced by Guise et al. [4–6], our goal is to develop unique nanostructures to explore the fundamental spin phenomena of patterned Ge/Si(001) quantum dots (QDs) as demonstrated theoretically by Pryor et al. [7] and Levy [8–11]. A thorough study of process conditions and the resulting nanostructure will allow us to fully understand the spin-physics of our devices.

1.2   Heteroepitaxial semiconductor growth: the case of Ge/Si(001)

Silicon and Germanium are the most prevalent semiconductors used for commercial device fabrication. Falling directly below Carbon on the periodic table, Si and Ge are diamond structured group IV semiconductors. Because of their half-full valence bands (yielding 4 unpaired electrons), Si and Ge readily bond to many other elements and thus can be favorably alloyed or doped to fine-tune their electrical, optical, and thermal properties. In addition to the high natural abundance of Si, its flexibility in terms of structure, properties, and processing allows wide applicability for data storage, logic devices [12–14], light emitting diodes [15] , solar cells [16], and thermoelectrics [17–19].

Figure 1-1 shows the Si-Ge phase diagram, which exhibits 100% solid solubility in the diamond phase. As a bulk alloy, SiGe is most commonly employed in the source and drain elements of a modern transistor. SiGe has replaced polycrystalline Si in this application due to its ability to grow epitaxially and eliminate physical defects inherent in poly.

Ge-Si

LIQUID

DIAMOND_A4

Temperature / K

x Si

Ge

Si
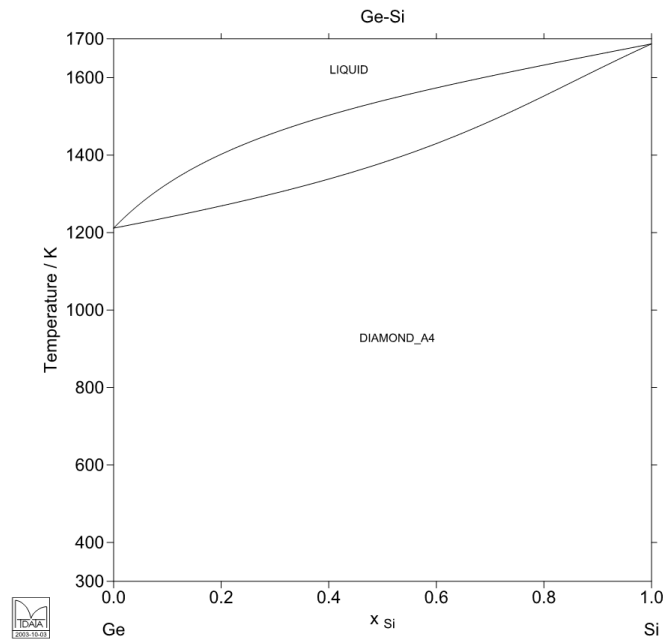
Figure 1-1: Calculated Ge-Si phase diagram [20]

From a semiconductor performance point of view, Ge can also be used to augment the operation of Si. By growing an epitaxial layer of Si on top of a SiGe (virtual) substrate, the resulting Si layer will be physically strained. Stretching of the Si bonds ultimately results in enhanced electron mobility, and hence increased logic throughput.

As briefly discussed here, though the Si-Ge system is simple, a number of clever tricks resulting purely from the lattice parameter variation in Si and Ge have been used to enhance the performance of conventional semiconductor device technology. However, as device scaling is facing many quantum mechanical limitations: (1) several atom wide channels, and (2) even thinner gate oxides, developing a thorough understanding of semiconductor surfaces and interfaces is crucial.

Over the last 30 years, researchers have intensively studied the heteroepitaxial growth of Ge films on clean Si (001) surfaces. The resulting surface structures and interfacial properties of Ge/Si(001) exhibit a complex material interaction that is conceptually rich in fundamental materials science with great potential for future spintronic device applications. Much interest in this system has surfaced due to the possibility of customizable strain-induced three-dimensional Ge/Si(001) nanostructures. The size and shape of these so-called Ge quantum dots (QDs) can be tuned on a length scale that is typically inaccessible from top down nanofabrication techniques. As such, the possibility of incorporating emerging spintronic technology based on Si-Ge offers an attractive alternative to III-V functional semiconductors since they are inherently compatible with existing group IV production facilities.

1.2.1   Quantum dots

Ge/Si(001) QDs evolve via the Stranski-Krastanow (S-K) mode of heteroepitaxial thin film growth [21]. Ge grows pseudomorphically upon Si where the cohesive film strain, ε_{coh} , is a function of lattice mismatch, via Equation 1-1:

$$\varepsilon_{coh} = \frac{a_{film} - a_{subst}}{a_{subst}} \qquad\qquad \text{Equation 1-1}$$

for Ge/Si(001), ε_{coh} = -4.2%. S-K growth is typical for moderately strain systems and is signified by the initial growth of a 2D wetting layer, followed by nucleation of 3D islands, as shown in Figure 1-2.
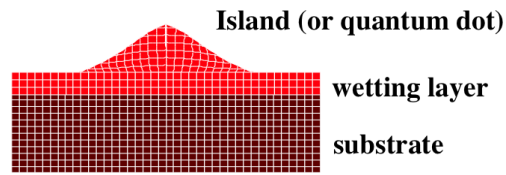
Figure 1-2: Schematic representation of the S-K growth mode.

In the case of Ge/Si(001) the equilibrium wetting layer thickness is 3 monolayers (ML). Subsequent Ge layers relax by faceting [22,23] to specific crystallographic planes that balance strain and surface free energy. Furthermore, the wetting layer thickness at which island relaxation occurs and the ultimate island size may be tuned by $Si_{1-x}Ge_x$ alloying [24–26]. Here, the strain is a function of alloy composition and can be described by equilibrium thermodynamics and elasticity theory. Line scans extracted from AFM data shown in Figure 1-3 describe the profile, faceting, and relative SiGe strain state of typical pyramid and dome shaped QDs. These island shapes are ubiquitous in the $Si_{1-x}Ge_x$/Si (001) system [27]. In this case, $Si_{1-x}Ge_x$ islands with x=0.5 are shown.
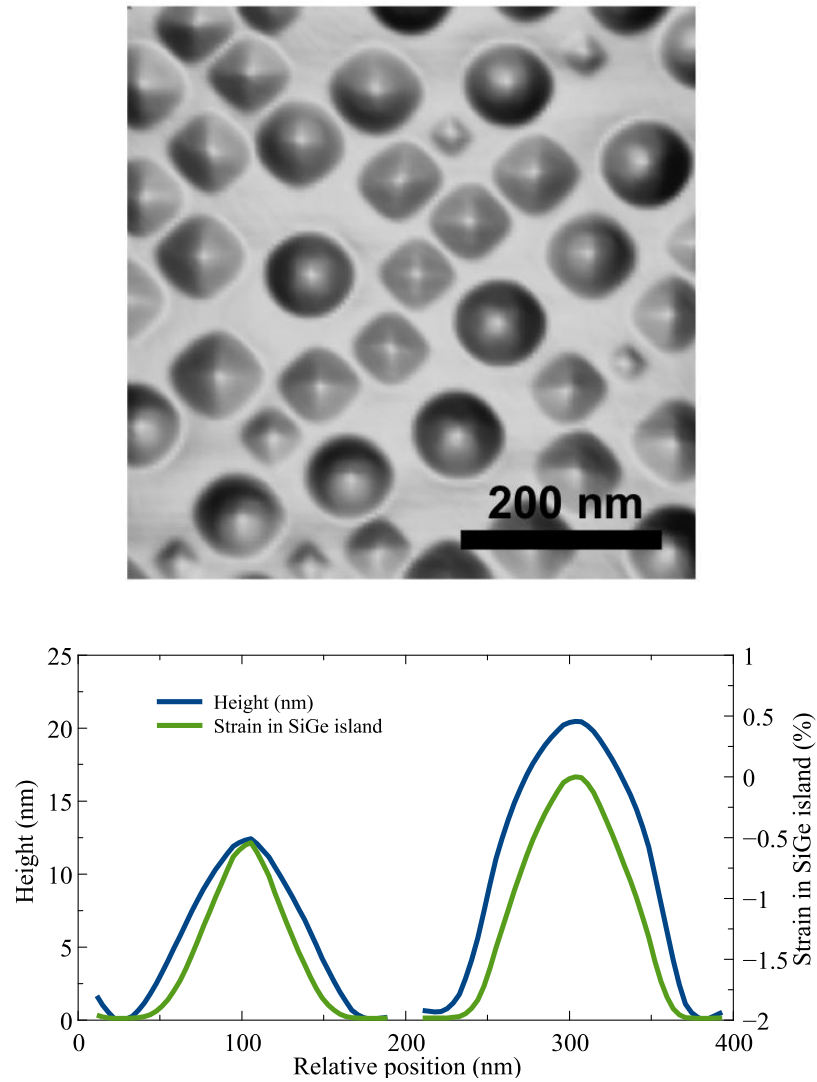
Figure 1-3: An AFM topography image along with island profiles and estimated strain for the $Si_{0.5}Ge_{0.5}/Si(001)$ system. Strain is calculated from Equation 1-3.

An additional AFM image of $Si_{0.5}Ge_{0.5}/Si(001)$ islands is shown in Figure 1-4(a). By using a simple high-pass filter, abrupt changes in surface angle are highlighted which delineates surfaces facets. Figure 1-4(b-d) are the resulting high-pass filtered images, including enlargements of {105} faceted pyramids and multiply faceted ({105}, {113}, and {15 3 23}) domes.
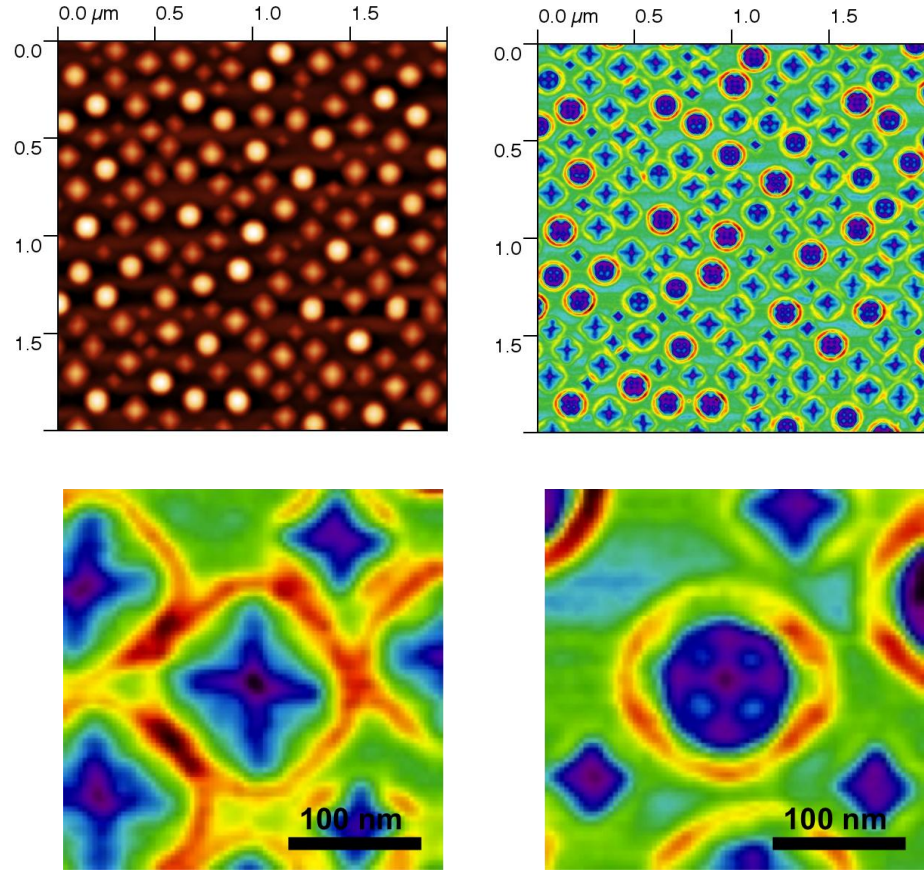
Figure 1-4: An example of facet delineation using a high-pass filter. In this particular scan, we can observe {105}, {113}, and {15 3 23} facets. The bottom two panels are selected huts and domes showing faceting as observed with AFM.

Ge/Si(001) growth at near-equilibrium growth conditions (e.g. low deposition rate and high temperature) allows one to investigate the thermodynamic aspects of strain-driven self-assembly in great detail. In general, the critical wetting layer thickness exhibits a total film stress such that the energy gain from 3D roughening is greater than the related cost of increased surface area. À la classic nucleation and growth, the total change in energy (ΔE_{tot}), is a function of surface energy (γ), cohesive elastic energy density (W_{coh}), island shape (G_{island}), island volume (V_{island}), and the change in surface

area, (ΔA). This relationship is shown in Equation 1-2. A detailed analytical solution for this equation has been demonstrated by Lu, et al. [28] for the formation of Ge/Si(001) huts; the resulting energy balance as a function of nucleation volume is shown in Figure 1-5.

$$\text{E}_{tot} = \left(\gamma_{2D\ film} - \gamma_{island}\right) \cdot \Delta A - \left(G_{island} \cdot W_{coh}\right) \cdot V_{island} \qquad \text{Equation 1-2}$$
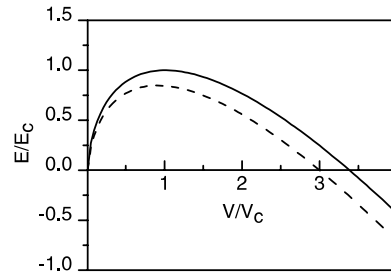
Figure 1-5: The hut formation energy as a function of volume. The solid curve is based on Equation 1-2, and the dashed curve includes edge terms as described by Lu, et al. [28].

After surmounting the wetting layer thickness (magnitude depends on Ge_xSi_{1-x} composition), slight topographic surface roughening perturbations nucleate regularly faceted {105} pyramidal structures. This four-fold equilibrium shape has an 11° contact angle with the substrate and forms with a square bottom along <100>. At low growth temperatures (300-500°C), some pyramids elongate along one of the <100> directions, which is a lower energy coarsening mechanism than adding atomic planes to large {105} facets [29]. Such elongated structures are known as 'huts' and are hence kinetically controlled features. With continued Ge deposition 2D islands nucleate and continuously exchange material with pyramidal structures, and with sufficient Ge, they eventually develop into pyramids.

In order to further relieve energy higher aspect ratio dome structures nucleate with increased Ge coverage. As deposition continues, higher volumes of material exchange between adjacent islands, and with the wetting layer [30], such that large {105} facets dominate the surface, when this energy surmounts an activation energy barrier to shape transition, many large pyramids experience an abrupt change to complex {113} and {105} faceted dome structures. Dome structures have a 25° contact angle with the substrate, then flatten to an 11° angle ({105} surface) nearing a flat (001) top. Though this shape transition accompanies a large increase in surface area, these larger QDs allow a greater volume of Ge to exist at larger distances from the fully compressed Ge at the hetero-interface. The amount of Ge strain relaxation in the QD has been directly measured by others [31–34] and is given by Equation 1-3 as a function of QD height.

$$a_y(h) = a_{bottom} + (a_{top} - a_{bottom})(\frac{h}{h_{max}})^2 \qquad \text{Equation 1-3}$$

From this equation, we estimate the residual strain at the apex of pyramids and domes to be 0.9% and 0.0%, respectively. This was demonstrated in Figure 1-3.

At the highest Ge coverages, the film has sufficient energy to nucleate misfit dislocations at the hetero-interface. These dislocations accommodate nearly all interfacial strain resulting completely relaxed "superdomes". Such relaxed nanostructures thus have a minimal attachment barrier and behave as a sink for adjacent strained material. Wild growth of "superdomes" thus consumes all islands in the vicinity carving out a wide Ge depletion region.

1.3   Nanoscale patterning

To enable the application of quantum dots for data storage or logic devices, is it of

paramount importance to precisely define their position in space. Many techniques have

been developed to achieve this goal at the nanoscale, including emerging optics that

utilize extreme ultraviolet (EUV) for parallel resist-based patterning [35] or focused ion

beams (FIBs) for direct write solutions [36,37]. These techniques both generate pits to

direct strain induced QD formation at geometrically defined points on the wafer.

Although these techniques have demonstrated accurate placement of QDs, they are

fundamentally limited in the 50-100 nm length scale. In this study, QD spacings of less

than 35 nm are required to demonstrate spin-coupling, so we turn to an alternative

patterning route, utilizing energetic electron beams[*].

Electron beam lithography (EBL) is the technique of fine scale pattern generation

using an electron source, typically in an SEM or TEM [38]. Originally, EBL was used to

write 2D patterns in photoresist, but this method is still tied to the limitations of difficult

post-processing, namely wet/dry etching. Alternatively, electron beam induced deposition

(EBID) can be used to direct deposition via localized dissociation of a precursor gas at

the beam-substrate intersection. Though similar to FIB, owing to the much lower mass of

energetic species (electrons versus ions), EBID avoids implantation damage and the

deposited material quality is superior to that of FIB.

In this study, we utilize EBID for carbon-based pattern formation via a controlled

form of so-called "contamination lithography". This technique takes advantage of the

---

[*] A summary of patterning techniques and their capabilities is listed in Appendix 1.

hydrocarbon background pressure in a moderate SEM vacuum as the carbonaceous

precursor gas. Using an SEM, we have achieved sub-8nm "contamination deposits" with

spacings down to 22.5 nm [4–6], as shown in Figure 1-6. Others have realized sub-5 nm

features using TEM optics [39]. In Chapter 5, we explore the full atomic structure of

these carbon-based nanopatterns and their effect on Ge/Si(001) heteroepitaxy.
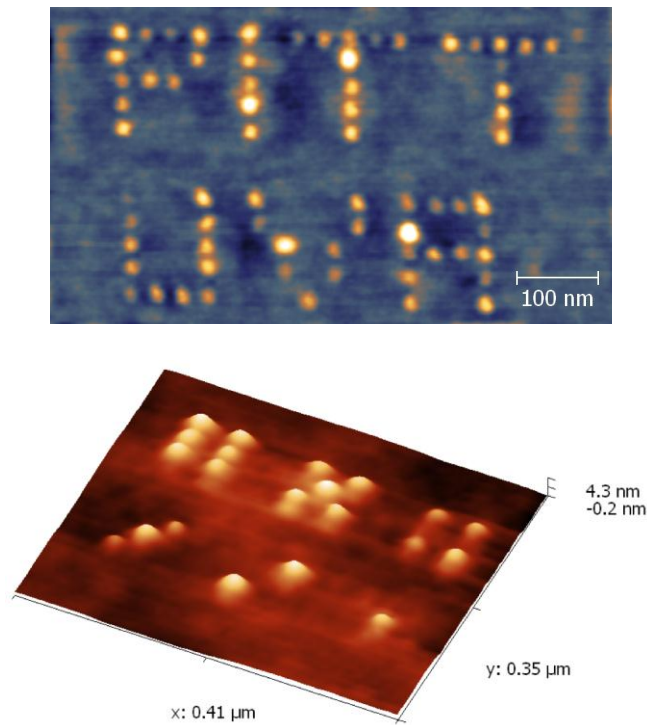
Figure 1-6: Nano-dice with unit spacing of 45 nm. The minimum spacing is along the "six", showing isolated features with 22.5 nm spacing.

1.4   Spintronic properties of Ge/Si(001) quantum dots

In a study by Pryor, Flatte, and Levy [7], the band structure was calculated for an

embedded, strained-induced Ge quantum dot, see Figure 1-8. This model establishes the

critical length scales for realization of quantum confinement and spin-based electrical

interactions. First and foremost, in the proposed model, it is found that the quantum dot diameter must be less than 10 nm in order to confine single electrons. This imposes the greatest challenge for Ge/Si quantum dots since this length scale is less than the size dictated by thermodynamic strain driven QD formation. Thus, it will be necessary to invoke process methods to (1) increase the interfacial strain or (2) tailor the growth kinetics to form metastable nanostructures.

Additionally, due to the steep strain and composition gradients at the Ge/Si interface, the band alignment is expected to be type II. This differs from type I band alignment in that the embedded Ge material forms a staggered gap, imposing a barrier only to electrons (Figure 1-8). This barrier is predicted to be quite weak, allowing a wavefunction decay length of 10-15 nm (Figure 1-8, red curves). As a result, QD separations must be approximately 35 nm to experience direct exchange via wavefunction overlap. We have achieved interdot spacing down to 22.5 nm in this study, which is expected to have an antiferromagnetic exchange interaction energy of about 1.35 MeV (T ≈ 15.7 K).
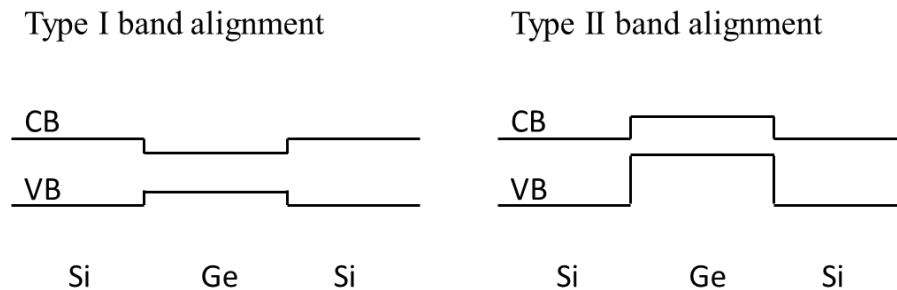
Figure 1-7: Schematic illustration of Type I and Type II band alignments.
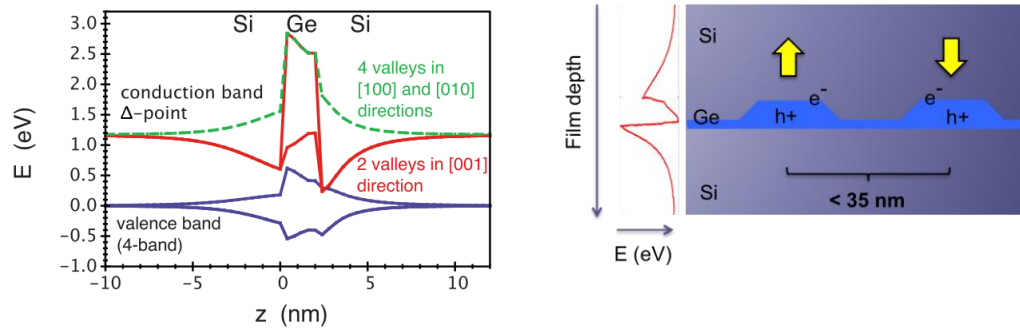
Figure 1-8: (A) Band edge diagram of an embedded Ge QD. Image taken from Pryor et al. [7] (B) Adapted schematic showing the geometrical location of strain-induced quantum wells. Holes are expected to be tightly bound in the Ge QD, while electrons are expected to be weakly bounded to the Si/Ge interfaces above (and below) the QDs. Arrows denote the suggested antiferromagnetic spin coupling behavior.

Pryor, et al. [7] determined that the magnitude of the exchange interaction depends on the interdot separation, L, and the electron wavefunction decay length, B. In that work, it is found that the potential well depth (and hence wavefunction decay length) is directly related to the magnitude of the interfacial strain. Since the strain is different at the island base versus the apex, it follows that there is a variation is electron wavefunction decay length. Equation 1-4 is the relationship for base-localized states (BLS), where B=12nm. A is the exchange coefficient, 10 meV for Ge/Si.

$$E_{ex} = A \, e^{\frac{-L}{B}}$$

Equation 1-4

Potential device architectures based on direct exchange coupled QDs will be introduced in Chapter 5. It was the main thrust of this dissertation to develop and characterize patterned QDs at the lengthscales discussed here as part of a larger effort to perform magnetotransport measurements. A detailed process and structural analysis of such nanostructures is also presented in Chapter 5.

1.5   Low temperature epitaxy

An ongoing desire for the field of semiconductor crystal growth is to achieve high quality thin films with reduced processing temperatures. The benefits of this are twofold: (1) compatibility with auxiliary semiconductor processing and (2) high quality, metastable alloys and nanostructures. For example, a long standing fabrication issue is the so-called "doping problem" wherein the doping levels for desired electrical properties are greater than the equilibrium solid-solubility of the constituent materials (e.g. Mn [40], Sn [41], or Sb [42,43] in Ge and Si). In order to facilitate super-saturation of dopants, metastable incorporation at low growth temperature is possible, but growth of the host material is diffusion limited, resulting in the detrimental incorporation of defects and an amorphous transition. Additionally, successful low temperature growth is expected to produce sharp interfaces during heteroepitaxy and to stabilize ultrasmall QDs from coarsening. One goal of this dissertation is to investigate low temperature epitaxial breakdown and the amorphous phase transition in the presence of multiply-faceted Ge/Si(001) QDs.

Understanding the growth of epitaxial thin films at low temperatures is critical to control fine scale atomic structure of surfaces [44], [45]. Early reports by Eaglesham [44,46], Gossman [43] and Bratland [47] have investigated homoepitaxial growth of Si/Si(001) and Ge/Ge(001), respectively. In both materials, a temperature-dependent epitaxial breakdown thickness, h_{epi}, is observed, above which defect nucleation and amorphous phase transition occur. The existence of a limiting thickness is primarily attributed to kinetic roughening during low temperature epitaxy.

Several factors affect the rate and magnitude of surface roughening, including H-adsorption, kinetic roughening, and misfit strain. Adsorbed H on semiconductor surfaces is detrimental to adatom mobility since H-termination of dangling bonds locally alters the surface reconstruction [48] and inhibits surface diffusion of adatoms to ideal epitaxial positions. Similarly, kinetic roughening is an effect of limited mobility at low temperatures, which causes proliferation of step edges and even formation of shallow (<3°) pyramidal mounds. As these pyramids coarsen and impinge, the epitaxial layer can nucleate stacking faults and microtwins which further devolve into deep {111} faceted cusps. Eventually, surmounting defects on heavily faulted surfaces initiates the epitaxial-amorphous transition. This morphology progression is illustrated in Figure 1-9. Alternatively for heteroepitaxial films, misfit strain provides an additional driving force for roughening that might enhance epitaxial breakdown at low temperatures.
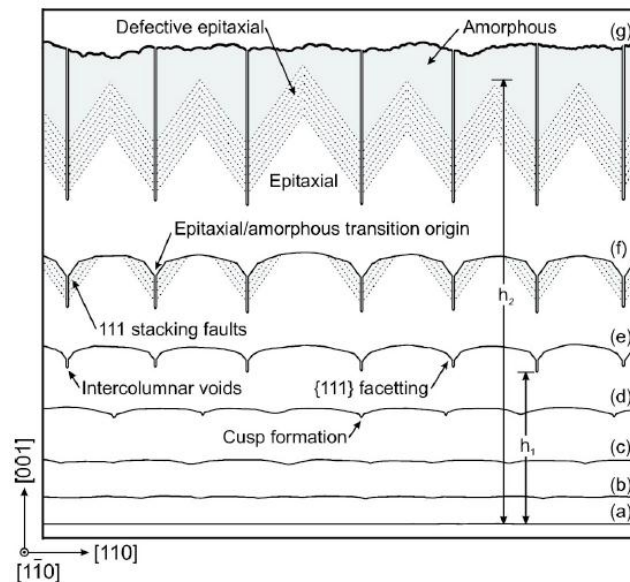
Figure 1-9: Schematic diagram illustrating the microstructural and surface morphological evolution of Ge homoepitaxial film growth at low temperatures. [47]

Many investigators have implied that film strain also has a significant effect on the measured critical epitaxial thickness [49]' [50], yet no quantitative relationship has been suggested in an applicable heteroepitaxial system. In a recent study by Bratland, Sn doping was shown to enhance h_{epi} with surfactant effects at low Sn-concentration (0.1 at.%) and reduce h_{epi} at high Sn-concentration (>2.0at.%) due to increased strain in the range of 0.29-0.90%. This establishes a baseline, but additional work is necessary to understand growth processes of technologically important Si capping layers for heteroepitaxial QD systems. In Chapter 4, we present a detailed study of the evolution of low temperature Si overlayers in the vicinity of inhomogeneous strain and multiply faceted QDs.

Chapter 2: Experimental Methods

2.1   Molecular Beam Epitaxy

All of the growth experiments included in this dissertation were conducted in our custom, homebuilt Hyperthermal Molecular Beam Epitaxy (HyperMBE) chamber at UVa. HyperMBE is unique from other MBE systems in that it is designed to access a broad window of kinetic deposition parameters. Typical Group IV MBE utilizes thermal evaporation and/or electron beam evaporation of deposition materials. The benefit of these techniques is that operation is completely in UHV, minimizing the chances of contamination from process gasses. These evaporation techniques also have certain disadvantages including potential thermal loading of the sample, extensive outgassing, contamination of source material, and poor rate stability. Such growth techniques may be considered *thermal deposition* wherein "thermalized" atoms with low energies (e.g. ≤ 1 eV) are used. This holds a constraint on thin film growth such that high substrate temperatures (500-700ºC) and slow deposition rates are required for smooth layer-by-layer film growth or to promote coherent Ge/Si(001) self-assembly of QDs.

In contrast, our HyperMBE employs three variable-distance magnetron sputter guns for deposition of Ge, Si, and Al. These sources are operated with DC power up to 80W. Deposition rates can be varied between 0.05Å/s and 6.5Å/s depending on power and substrate-target separation, with no thermal loading of the sample. Using *Transport of Ions in Matter* (TRIM) modeling, we estimate ejected species to have energies in the range of 1-20eV upon exiting the sputter target (see section 2.2 for more detail). Though the precise degree of deposition flux thermalization during transit to the substrate in an

Ar ambient is unknown, we can calculate the mean free path of ejected atoms to be approximately 3cm in 3 mT of process gas. (The mean free path is plotted in Figure 2-1 as a function of pressure). By varying the working distance of the sputtering source (1-12cm), one may effectively tune the degree of thermalization *on average*. As a result, deposition with high energy species enables the possibility of hyperthermal growth, implying enhanced adatom mobility. Thus, increased surface diffusion rates facilitate high quality thin film growth at higher deposition rates and lower temperatures. The effects of adatom energy on film growth are summarized by Ensinger [51] in Figure 2-2.
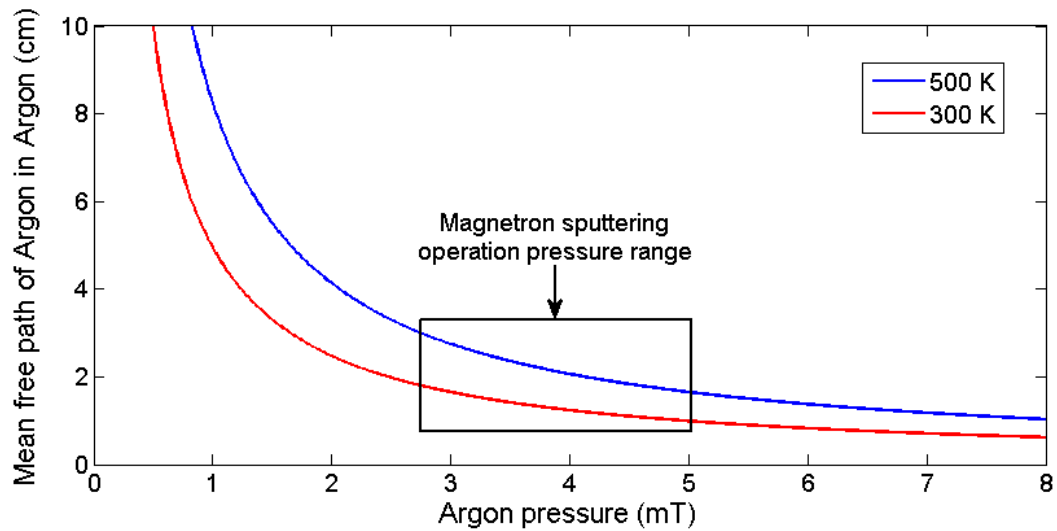
Figure 2-1: Mean free path of Argon as a function of pressure.
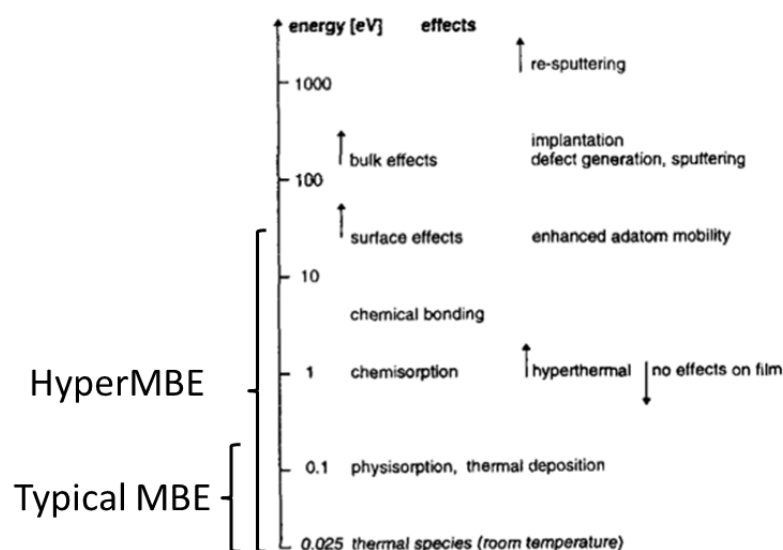
Figure 2-2: Effects of low-energy ion bombardment on thin film growth at different energy levels [51]. Growth effects are analogous for energetic growth species during sputter deposition.

Our HyperMBE was developed to achieve necessary UHV vacuum levels for Si processing, < 5 E-10T. To do so, the MBE is load-locked (see Figure 2-3B) using a transfer chamber that achieves 5E-9T via a single 300 L/s turbomolecular pump. Upon transfer to position G, clean Si wafers undergo thermal treatment for carbidization, oxide desorption, and thin film deposition with control of the precise sample position via a 5-axis manipulator (F). UHV pumping on the reactor (A) includes a 600 L/s turbomolecular pump, an ion pump at F, and dual titanium getter pumps. Finally, *in situ* real-time surface diffraction analysis is conducted via reflection high energy electron diffraction (RHEED) at H. RHEED is conducted at glancing angle (<4º) with a 20 keV electron beam through a magnetically shielded aperture (Ø=1 mm). The aperture tube covers approximately ½ of the beam path and is double-differentially pumped with two small turbomolecular pumps at Figure 2-3H. In our particular setup, the additional precaution

of shielding and differential pumping has been necessary to prevent electron scattering

due to stray magnetic fields resulting from the magnetrons.

A – MBE Chamber
B – Load Lock Chamber
C – Sample Loading Portal
D- Transfer Arm

E – Manual Gate Valve
F – Manipulator
G – Sample Location
H – RHEED Gun
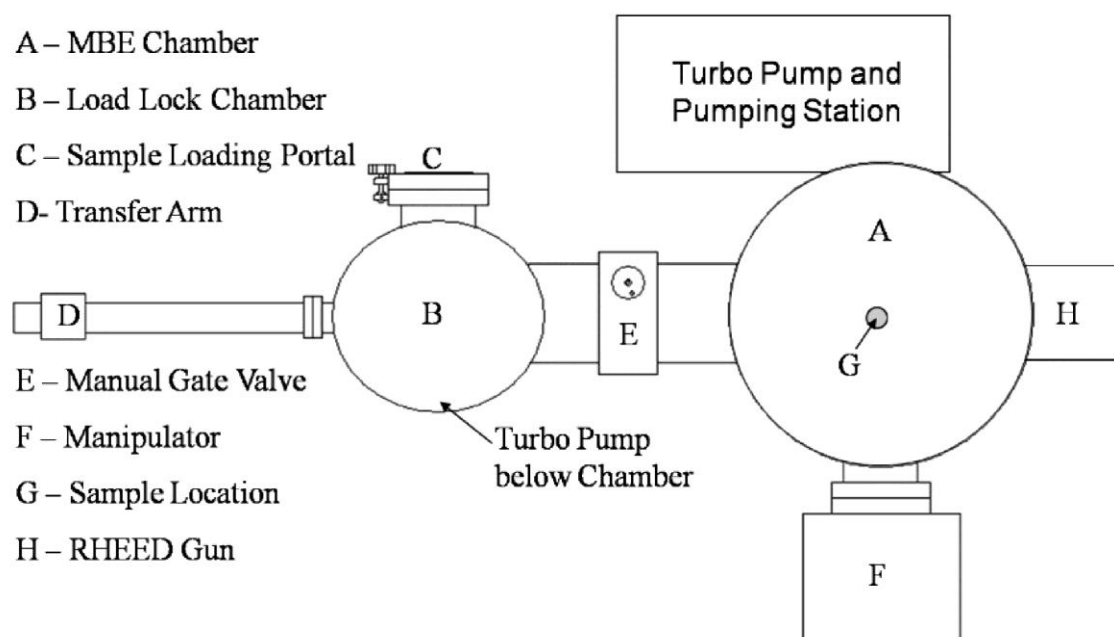
Figure 2-3: Top view of the UHV chamber showing key components for film synthesis. Borrowed from Copland Kell masters thesis (2009) [52].

The layout for all deposition sources is shown in Figure 2-4 below. Our main

deposition species, Si and Ge, employ 2" sputter targets of 99.9999% (6N) purity. Mn

and Al are dopant species, requiring much lower deposition rates and are deposited using

thermal (Knudsen cell) evaporation and 1" target magnetron sputtering[†], respectively.

[†] It is important to note that due to the reduced size of the Al magnetron target (1"), fewer permanent magnets can physically fit inside the source. Consequently, this limits the minimum working Ar pressure required to maintain a stable plasma. We have experimentally determined that the 1" sputter gun requires a partial pressure of 20 mT, compared to 3mT for the 2" Si/Ge sputter sources.

Plasma ignition for magnetron sputtering requires an argon pressure of 1-4 mT, to

achieve this, the HyperMBE is back-filled from UHV with high-purity gas. Since the

pressure must be increased by 7 orders of magnitude, the initial impurity concentration

must be less than 10ppb. Additional information on deposition rate calibration via *in situ*

quartz crystal microbalance (QCM) and *ex situ* secondary ion mass spectroscopy (SIMS),

can be found in Appendix 2.
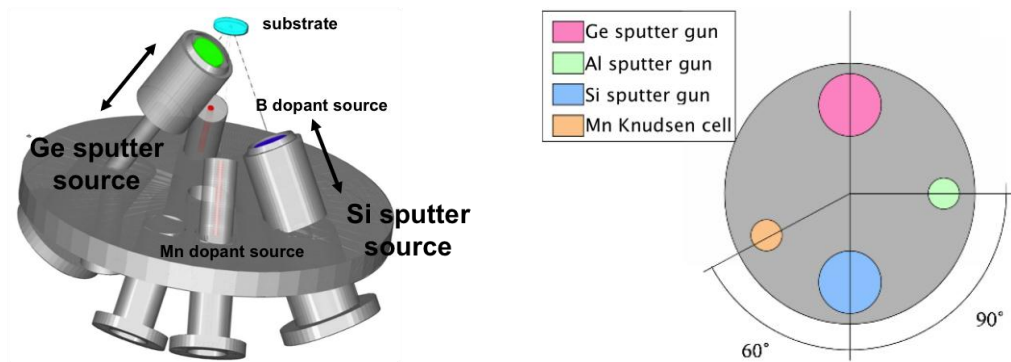
Figure 2-4: Layout of deposition sources in the HyperMBE. Figure courtesy of Copland
Kell masters thesis (2009) [52].

2.2   Energetics of deposition via magnetron sputtering

As mentioned earlier, one may achieve a wider kinetic window of deposition flux

by utilizing magnetron sputtering. Magnetron sputtering is a PVD technique that relies on

the physical bombardment of energetic ions onto the source material to generate

deposition species, e.g. Ar+ into Si. An atom is ejected (sputtered) from the source

material if the energy of the bombardment is greater than the surface binding energy

(E_B) [53]. E_B has been experimentally determined to be approximately the heat of

sublimation, which for Silicon is: 4.96 eV/atom.

In order to ignite a glow-discharge plasma an electric field is applied in the vicinity

of the sputter target. By tuning the strength of the electric field, one can control Ar+

energy and hence the sputtering yield (this also directly scales with the deposition rate).

However, the energy distribution of the ejected target atoms also scales with the incident

Ar+ energy. This energy spread is defined by the Thompson distribution [54], shown in

normalized form in Equation 2-1:

$$\frac{dN/dE_T}{N} = \frac{2E_B E_T}{(E_T + E_B)^3} \qquad \text{Equation 2-1}$$

where dN/dE_T is the number of particles in an energy interval dE_T, E_B is the surface

binding energy and E_T is the kinetic energy. This function is plotted in Figure 2-5 for

various E_T. The result is a Maxwell-Boltzmann distribution with a maximum centered at

~ ½E_B and features a long high-energy tail.
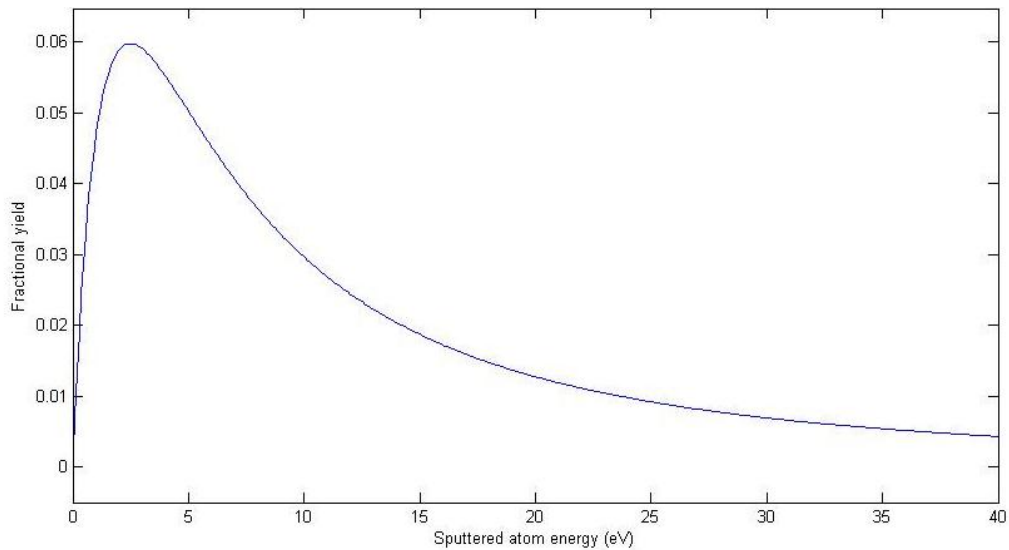
Figure 2-5: Normalized energy distribution of sputtered atoms (Si)

When using sputtering as a deposition source, one must aware of the possibility of high energy vapor species resulting from the tail of the Thompson distribution. With increased electric field, the energy spread broadens, increasing the yield of deposition species with energies far in excess of E_B, which are capable of re-sputtering material from the substrate. Fortunately, since sputtering is typically operated in a high background pressure of inert gas (1-10 mT), there is a high probability of thermalization due to vapor collisions.

As shown earlier, in Figure 2-2, the deposition energy range between 10-100eV may permit enhanced adatom mobility. To reach this energy range, it is required to minimize thermalization by reducing the background pressure and the working distance between the target and the substrate. By doing so, one runs the risk of encountering deposition flux that may re-sputter the substrate, but there exists great benefit in the ability to achieve quality epitaxial growth independent of substrate temperature. Preliminary experiments have been conducted in this high-energy regime and are presented in Chapter 7.

2.3   Electron beam lithography

Electron beam lithography is a method of generating patterned features in a serial fashion at the nanoscale. Typically, a focused electron beam (~1 nm diameter) is rastered across a specimen coated in photoresist resist while a beam blanker quickly modulates the beam. This results in irradiation of only selected areas of the photoresist, which may be subsequently developed and etched via standard photolithography processes. Although the serial nature of EBL results in much longer processing times than parallel

photolithography processing, the driving force for development of EBL is derived from the subversion of the diffraction limitation inherent in optical lithography.

The ultimate feature resolution of an EBL system depends mostly on the electron source and column optics. Moderate resolution systems utilize LaB_6 filaments (such as the Raith 50 EBL at UVa). The highest resolution systems employ tungsten field emission (FE) sources which have increased brightness and minimal energy spread of the electron beam. Using SEM optics, point spacings ~20 nm pitch have been achieved [55,56], while TEM optics can produce <10 nm spacing [39]. All patterns generated for the present study were generated using a Raith e_LiNE with a FE source at the University of Pittsburgh.

To achieve the finest resolution in our studies (<20 nm), the electron optics must be precisely aligned. During initial process development for SiC pattern formation, several trial runs were performed on the UVa Raith 50. Amidst this process, I worked with another graduate student to replace the existing LaB_6 filament, install new apertures (specifically 50μm), and fix minor vacuum issues. After maintenance was completed, I performed a full column alignment, including repositioning of the smallest beam-blanking plates.

2.3.1   Electron beam induced deposition

The process of EBID patterning of Ge QDs developed by Guise takes advantage of low level hydrocarbon contamination on a material surface. During their initial work, a controlled partial pressure of ethylene (C_2H_4) was emitted into an Auger spectroscopy system in which a hot Tungsten filament was used for electron irradiation at about

2keV [6]. During careful spectroscopic analysis, the deposition of elemental Carbon was observed on the Si surface. Subsequent annealing experiments showed evidence of SiC evolution at temperatures above 630ºC. This process is illustrated in Figure 2-6.
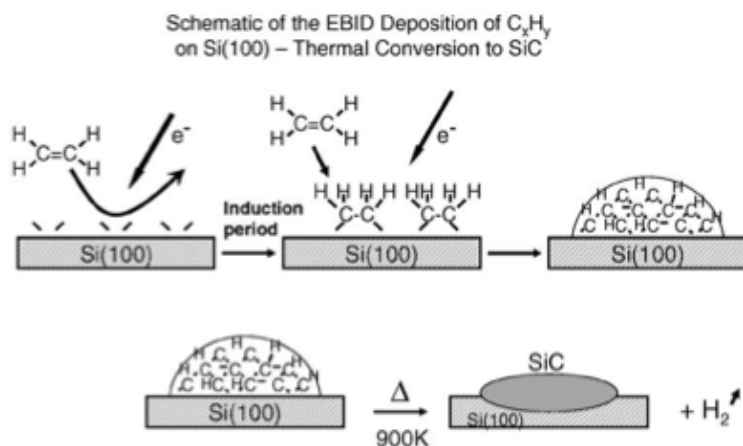
Figure 2-6: EBID of ethylene gas onto a Si(001) substrate and subsequent conversion to SiC [6].

The EBID process has been studied in depth by many groups [38,57–60]. It is first important to understand the complex electron-substrate interactions. Primary electrons of energies typically in the range of 1-30keV penetrate the surface and scatter into a tear-dropped shaped interaction volume that increases with electron energy. Due to inelastic collisions in the substrate, additional scattering events emit secondary and backscattered electrons with energies <50eV and >50eV, respectively [38]. As the C-C and C-H bond energies are less than 5eV, any of the incident *and* scattered electrons involved during irradiation may aid in the EBID process. However, since each energetic incident electron (20 keV), generates tens of secondary electrons, most of the EBID carbon is assumed to be caused by secondary electrons. Thus, the final width of the

amorphous C_xH_y dot is proportional to the width of the teardrop-shaped electron-bulk interaction volume. At low incident electron energy, when the interaction volume is small, the emission of secondary electrons is too low to cause significant EBID. Alternatively, high incident electron energies result in deeper bulk-penetration and wider interaction volumes. Thus, at high energy we experience the limitation of broad EBID area and reduced EBID rate. Optimization of the appropriate EBID energy has been conducted by others [38,39], and we use an energetic electron beam of 20keV for the current study.

Taking this process a step further, high-resolution electron beam lithography was used to obtain square pattern arrays of nanoscale carbide precipitates [4]. As shown in Figure 2-7, carbon is locally deposited in the EBL system, and annealed in UHV at ~920°C to form SiC. The substrate temperature is then lowered to 400°C for deposition of <2 ML Ge. This volume of Ge is below the critical thickness for spontaneous strained island nucleation on Si(001). Finally, the array is annealed at 700°C to increase the Ge adatom mobility and further assist island nucleation and growth in the patterned region.
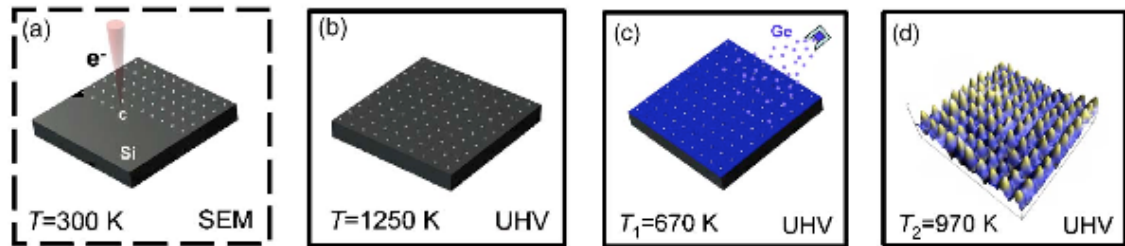
Figure 2-7: EBID and MBE process used by Guise, et al for sub-35 nm pitch Ge islands [5].

The work by Guise, et al has provided a significant basis for our research and leaves many interesting growth questions to be answered. First and foremost, are the Ge islands actually epitaxial and are they regularly faceted? What is the island size/shape distribution and what controls this? SiC has a large lattice mismatch with Ge, and there is no stable Ge-carbide, so does Ge actually segregate to these sites, and if so, why? What are the kinetics of Ge self-assembly? And finally, can we alter the growth kinetics using HyperMBE to obtain a narrower island size distribution? It is the goal of this dissertation to develop this capability at UVa and explore these questions.

2.3.2   Sample preparation for EBID

As mentioned above, collaborators at the University of Pittsburgh generate our patterns with a Raith e_LiNE lithography system operated at 20keV. This system uses a field emission filament and the exposure parameters have been optimized to minimize the electron-surface interaction volume and obtain sufficient carbon deposition. An example of a 35 nm as-patterned array is shown in
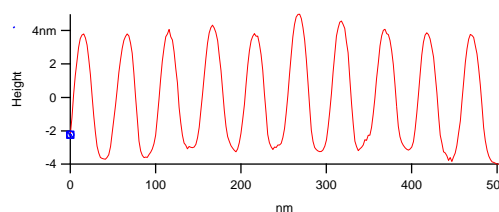
Figure 2-8: (Left) As-patterned EBL Carbon arrays with 35 nm spacing. Exposure using 20keV and 1.0pAs per C-island. (Right) Resulting line scan indicated on left image.

. The shape of the carbonaceous islands has a narrow size distribution, with excellent uniformity.
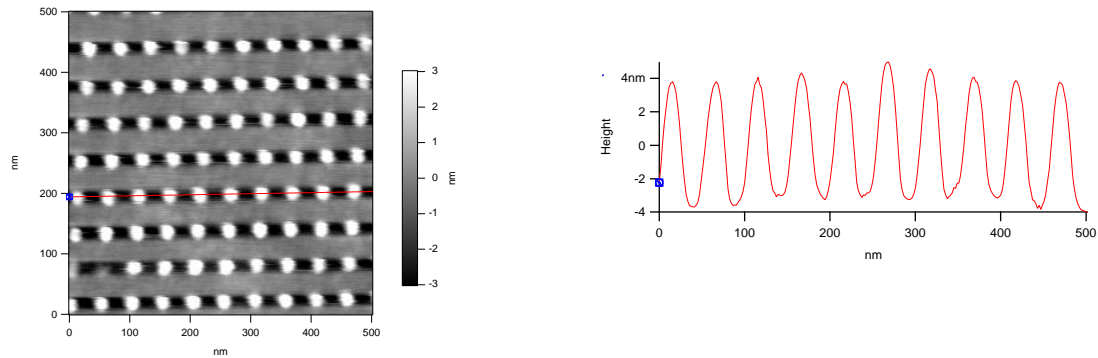
Figure 2-8: (Left) As-patterned EBL Carbon arrays with 35 nm spacing. Exposure using 20keV and 1.0pAs per C-island. (Right) Resulting line scan indicated on left image.

After patterning, substrates are exposed to UV ozone (UV-O$_3$) at UVa. This has proven to be one of the most sensitive processing steps. Wafers must be exposed long enough to remove excess hydrocarbons before introduction to UHV but not so long as to completely volatize the C arrays [5].

Once introduced to the HyperMBE, patterned samples are ramped up to 600°C in about 10 hours. This slow temperature ramp is used to minimize pressure bursts from sample outgassing. SiO$_2$ desorption and (nominal) SiC formation takes place concurrently during heating to ~830°C for 30 min. Samples are then quenched to room temperature for observation or cooled to 600°C for Ge deposition of 1-2 ML.

2.4 Specimen cleaning

Prior to insertion in vacuum, all wafers are chemically cleaned, although the requirements vary. For the best device quality MBE grown films, Si wafers are subject to a "full" IMEC, RCA, and Shiraki cleaning procedure [61]. IMEC is a solution of H$_2$SO$_4$ and H$_2$O$_2$ that attacks all hydrocarbons. The RCA and Shiraki processes utilize HCl and H$_2$O$_2$ to create a thin oxide at the wafer surface. By iterating between these solutions and

HF (or buffered ammonium fluoride), all metallic impurities near the Si surface are encapsulated in oxide and subsequently removed. In the final step a passivating sub-oxide, SiO_x, is generated to protect the Si surface during sample loading and annealing in UHV.

When stringent device or electrical measurements are not necessary, a "full" clean is not necessary. In this case, we perform an IMEC clean, followed by an HF dip and final passivation via $UV-O_3$ irradiation.

Finally, for patterned samples, a "full" clean is performed before sending wafers for EBL at the University of Pittsburgh. At Pitt, the wafer oxide is stripped via HF before patterning, then, once returned to UVa, the patterned wafers are subjected to a final $UV-O_3$ clean to remove spurious hydrocarbon contamination.

Chapter 3: Analysis Methods

3.1   Reflection high energy electron diffraction

Reflection high energy electron diffraction (RHEED) is a surface sensitive technique typically used for in situ monitoring of a substrate and/or growing film. Although RHEED typically operates at high energies (10-30keV), it is performed at a glancing angle (<5º), thus the surface penetration is on the order of <10 nm. Figure 3-1 shows a schematic of the RHEED implementation in the HyperMBE.
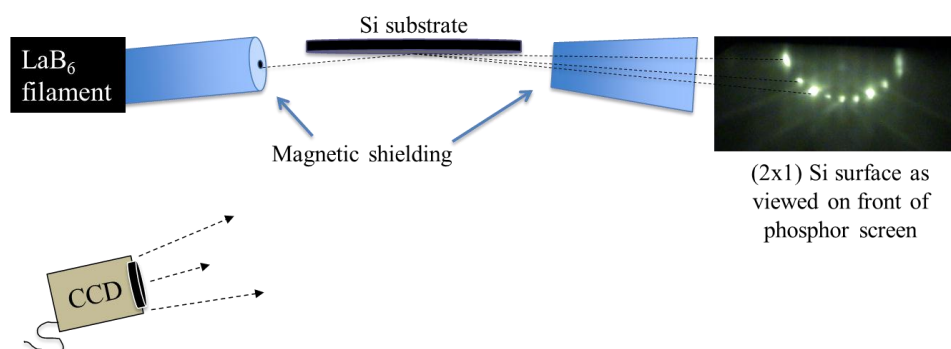
Figure 3-1: Schematic layout for RHEED in the HyperMBE.

Since the HyperMBE at UVa is based upon magnetron sputtering, we have taken great care to shield the electron beam path from stray magnetic fields. To do this, ideally one would use (1) a cylinder to cover the incident beam path between the electron source and the substrate and (2) a cone shaped shield between the substrate and the phosphor screen to shield the scattered electrons. However, due to the geometry of our viewing ports, we must view the RHEED screed from the front, thus shielding of the scattered beam-path is impossible. An important side note concerning front-viewing screens, is that

one must use a non-coated phosphor screen, and view the phosphor side directly.

Typically (for back side viewing screens) an electron transparent film is used to protect

the phosphor from scratches on the electron-incident side. However, when viewing from

the front, as in our MBE geometry, the protective coating scatters the reflected

fluorescent signal, blurring the diffraction pattern.

Despite our best efforts, we are unable to completely decouple the electron beam

from the magnetron sputtering sources. For example, when linearly translating the Si or

Ge guns, one easily observes a shift and distortion in the diffraction pattern. Similar

effects are also observed while modulating the DC electric field or operating the shutters.

We have mechanically positioned the RHEED source and double differential pumping

system with coarse alignment taking into account typical sputter source positioning.

Further alignment is controlled by two-sets of perpendicular deflection coils ($X_1 Y_1$,

$X_2 Y_2$), as labeled in Figure 3-2.
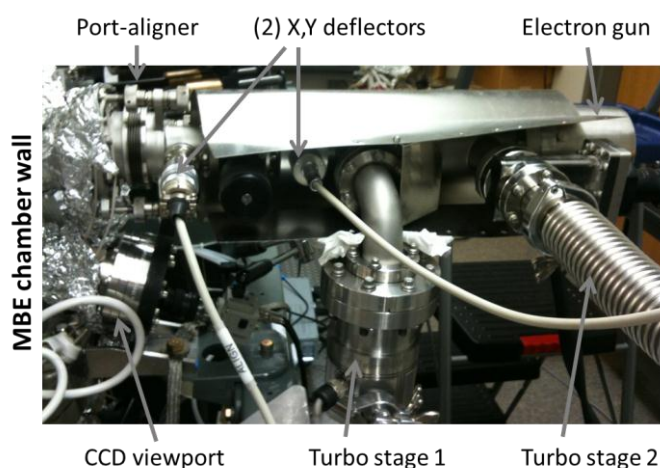
Figure 3-2: RHEED setup with two deflector coils and double differential pumping.

Once the incident beam is aligned onto the phosphor screen, adjustment of the beam is controlled via grid and focus. The grid control is similar to the condenser system in an electron microscope and is used to control the brightness of the electron beam. The focus knob is used to control the shape of the electron beam. Best conditions for electron diffraction exist in a compromise between grid and focus as shown in Figure 3-3.
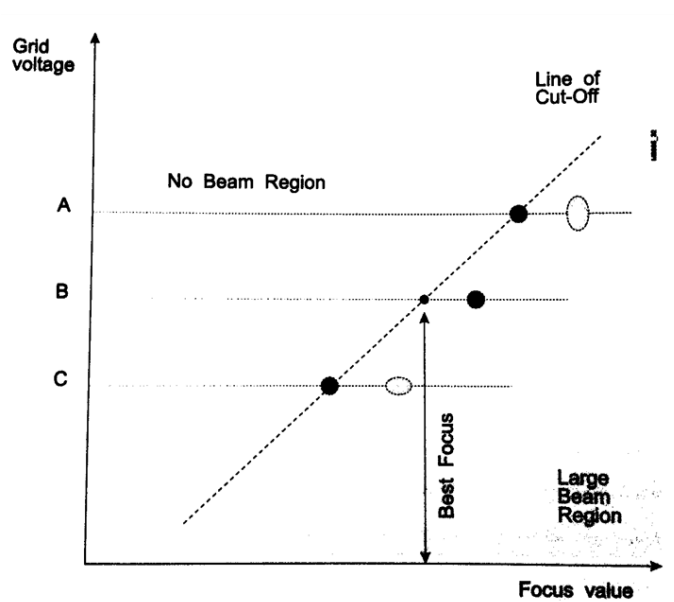
Figure 3-3: RHEED best focus as a function of focus value and grid voltage. [Image taken from Staib manual.]

The most relevant diffraction condition for investigation of Si(001) is along the <110> zone axis. In this direction, we observe the following diffraction patterns associated with: (1) SiO_x, (2) Si 2x1 reconstruction and (3) transmission diffraction through QDs in <110>. Examples of these surface diffraction patterns are shown in Figure 3-4.
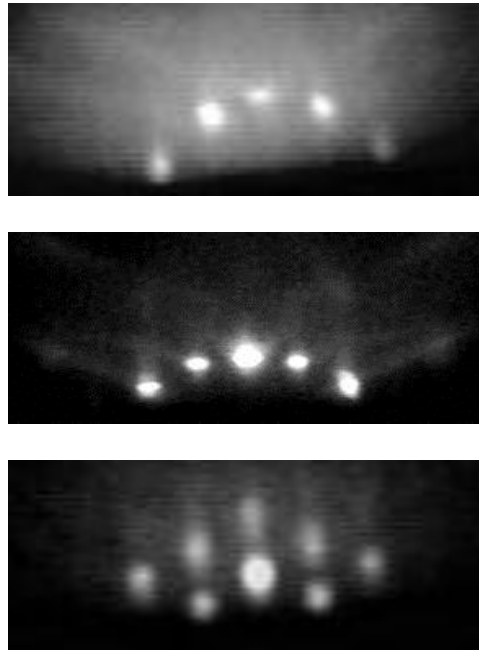
Figure 3-4: Typical RHEED patterns during Ge/Si sample processing in the HyperMBE. Top: (1x1) SiO2 surface prior to deoxidation. Middle: (2x1) surface reconstruction of Si after oxide desorb at 780°C. Bottom: transmitted diffraction through QD "roughened" Ge/Si surface, showing (1x1) geometry. All patterns are viewed along the <110> zone axis.

3.2   Atomic force microscopy

Atomic force microscopy (AFM) is the primary surface analysis technique used in our lab. While qualitative information about film quality is extracted from real-time RHEED, post-analysis with AFM allows topographical measurement of all surface nanostructures including quantum dots, pits, and contamination. For all measurements reported in this dissertation, we use an NT-MDT Solver Pro. This instrument is equipped with two scan-heads referred to as the Universal head (scan-by-sample) and Smena head (scan-by-tip). Images of the two scanning heads are shown in Figure 3-5.

Figure 3-5: (Left) Universal head for scan-by-sample and (Right) Smena head for scan-by-tip mode. Both are capable of contact and semi-contact topography scanning.

The Universal head is a stationary output device that accepts interchangeable tip-holders which allow access to different signals such as piezo force microscopy (PFM), magnetic force microscopy (MFM), etc. The universal head contains only the laser and photodiode for signal acquisition, while in-plane positioning is controlled by a separate piezo sample holder that rasters the specimen. The maximum scan range is 10um.

The Smena head does not have interchangeable tip holders and is thus less versatile in terms of signal collection. In this mode of operation, a stationary sample holder is used while the tip is rastered by the scan-head. The advantages of the Smena head include (1) a larger (100um) scan range and (2) 2D positioning closed loop operation for precise tip placement.

3.2.1   Topography measurement techniques

Topographic imaging with AFM is generally accomplished via two methods, namely contact or tapping modes. In contact mode, a tip is simply dragged across a surface, from which we can directly measure topographic features from the magnitude of

the cantilever deflection. The primary disadvantage to contact mode is that due to the static tip interaction, the signal is prone to distortion from lateral forces and capillarity effects during measurement in ambient. Alternatively, tapping mode (or semi-contact mode) is performed by oscillating the cantilever at its resonant frequency (see Figure 3-8) and measuring the change in amplitude. The force of intermittent contact with the surface causes a reduction in the amplitude. The Z-position piezo adjusts the tip height to maintain constant amplitude, and the magnitude of this feedback loop can thus be used to determine the topography. Tapping mode is not prone to the potential distortions of contact mode, but must be operated at slower scan speeds.

When using tapping mode, one can simultaneously capture phase contrast (PC) images of the surface. PC-microscopy is the measurement of the different in phase between the free cantilever oscillation and the phase-shifted oscillation as the tip comes in and out of contact with the surface. PC-microscopy is sensitive to material properties such as friction, adhesion, and local surface slope. Since the tip contact area is directly related to the surface slope, phase contrast is strong at facet edges. Figure 3-6 shows an example of a typical tapping mode AFM scan of a Ge/Si(001) QD surface and the resulting PC image. All pyramids have a distinct boundary due to the transition from scanning the (001) to the {105} surfaces. Domes exhibit the greatest contrast since the {113} sidewall represents a greater change in surface slope.
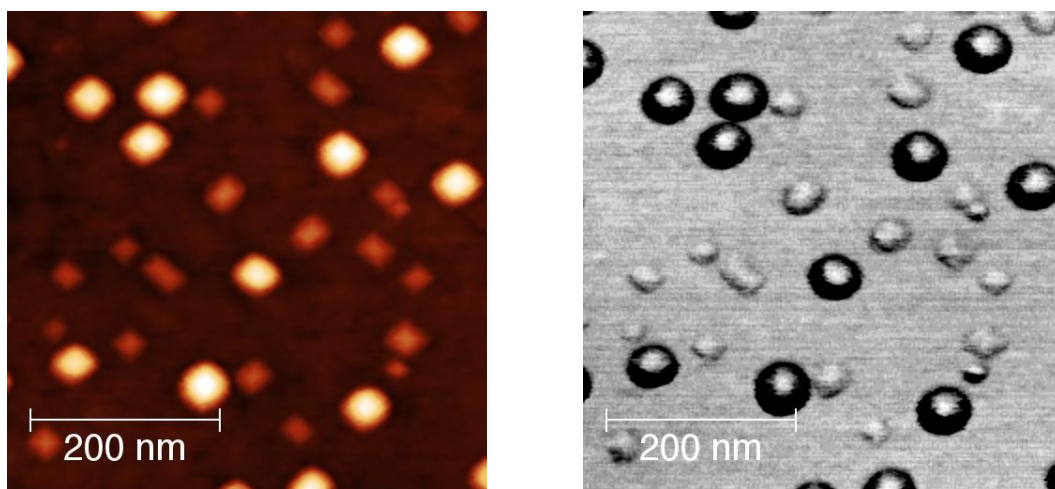
Figure 3-6: Example of topography and phase contrast microscopy using semi-contact mode.

3.2.2   General practice

Setup of the Solver Pro for basic topographic scanning involves 3 simple steps: (1) alignment of the laser on the cantilever, (2) determination of the resonant frequency, and (3) careful engagement of the tip. More detailed instructions can be located online, but tips for use of our system will be included here.

3.2.2.1   Alignment of the laser on the cantilever

Locating the AFM cantilever with the laser is simple, following the alignment procedure in chapter 1, part 3 of the NT-MDT manual. Once a laser diffraction pattern is observed on the table, it is recommended to place the scan head on the AFM podium and image the cantilever with the optical microscope. For best results, position the laser at about 2/3 of the cantilever length then manually wobble the laser positioning screws to maximize the laser signal under the "Aiming" tab. If positioned correctly, the intensity of

the laser should be 17-24 (relative units). If the signal is less than 17, the laser is not properly centered, and if the signal is much greater (e.g. >30), then the laser is reflecting off the chip. Proper laser alignment is shown in Figure 3-7.

Figure 3-7: Proper alignment of the laser on an AFM cantilever.

3.2.2.2   Determining the resonance

Finding the resonant frequency of the AFM cantilever is crucial for high quality imaging. To do this, the Nova software scans through a range of oscillation frequencies and measures the magnitude of the laser signal on the photodiode. This signal, referred to as "mag" has an optimum value of 20 nA with a Gaussian shape centered at the resonant frequency, as shown in Figure 3-8. The shape and magnitude of the signal is a function of: (1) stable positioning of the chip, (2) the preamplifier gain, and (3) the driving voltage (amplitude). We have found the most common reason for poor resonance mag signal is imperfect seating of the chip in the holder. If the AFM chip positioning is centered and secure, good results have been obtained for amplitudes of 0.07-0.7 V, and preamplifier gains of 5-30.
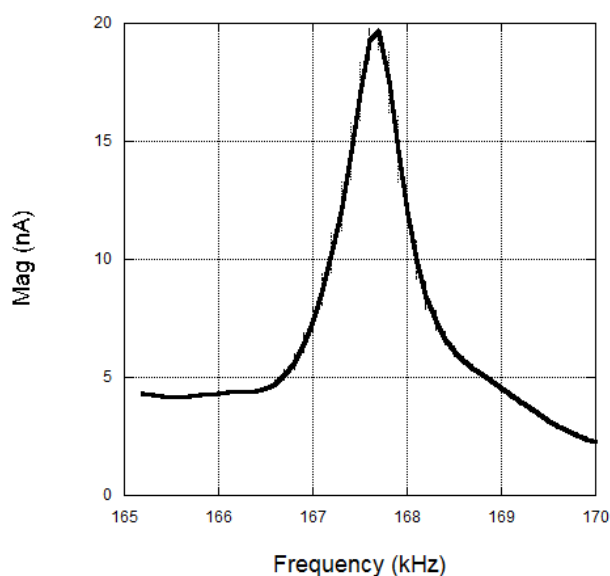
Figure 3-8: Example resonant frequency of a properly aligned AFM tip.

3.2.2.3 Landing the tip

Finally, an automatic routine for tip landing is controlled by the Nova software. This incrementally steps the tip towards the surface while monitoring the mag signal until it reaches a predefined setpoint. For best results, we use a setpoint equal to ½ the mag signal and a low feedback gain (FB) value of 0.05. As the tip approaches the sample, the mag will decrease slowly at first due to damping of the tip oscillation, then the mag will abruptly drop to zero when there is a strong van der Waals interaction. The feedback gain is then used to control Z-positioning of the AFM tip in order to maintain the Mag setpoint. The Mag signal during a typical landing procedure is shown in Figure 3-9. The tip-sample interactions are further illustrated as a function of separation during the

landing process in Figure 3-10. Depending on the scan mode, the operational tip-sample

separation is described by the red-highlighted regions.
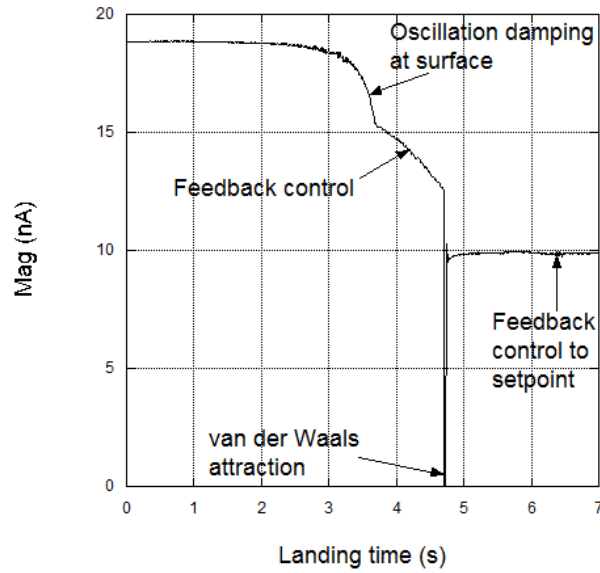
Figure 3-9: Mag signal during an ideal landing procedure.
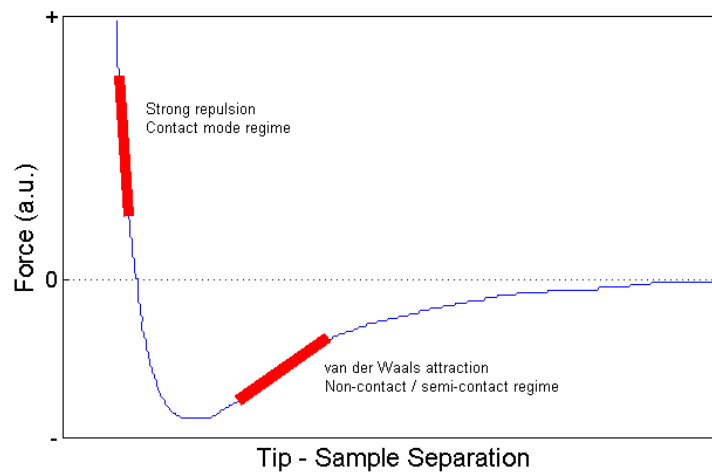
Figure 3-10: Tip-sample interaction forces as a function of separation distance.

For patterned specimen studied in this dissertation, it has been difficult to locate

small regions of interest (~15um^2). We have developed a scheme using hierarchical

fiducial marks. Prior to cleaning, Si wafers are scratched with a "+" (using a diamond-tipped scribe), which is optically visible. This scratch is used as the origin for EBL patterns and for coarse AFM tip positioning during surface analysis, as shown in Figure 3-11.
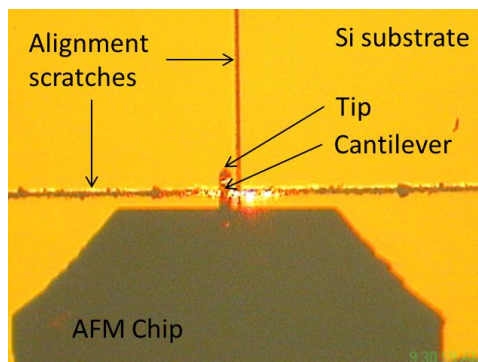
Figure 3-11: Alignment of the AFM tip for landing near EBL patterned regions.

Since the macro area scratches tend to generate massive debris, it is necessary to position the carbon templated arrays at least 50um away. In order to locate these offset arrays, we create 45° lines of carbon nanodots using a 10x dose. These lines of enlarged features are easy to locate and can be followed by the AFM tip to the pattern area of interest, a full pattern schematic is shown in Figure 3-12 and AFM of a 10pAs nanodot line is displayed in Figure 3-13. Additionally, an oblique SEM view of the templated fiducial nanodots is shown in Figure 3-14. The increased electron dose causes enhanced vertical over lateral growth rate. As a result, the steep fiducial nanodots are easy to find with AFM, but not ideal for templated Ge growth. More details on the volume evolution of carbon deposition is provided in Chapter 5 and studied in detail by van Dorp, et al. [38]
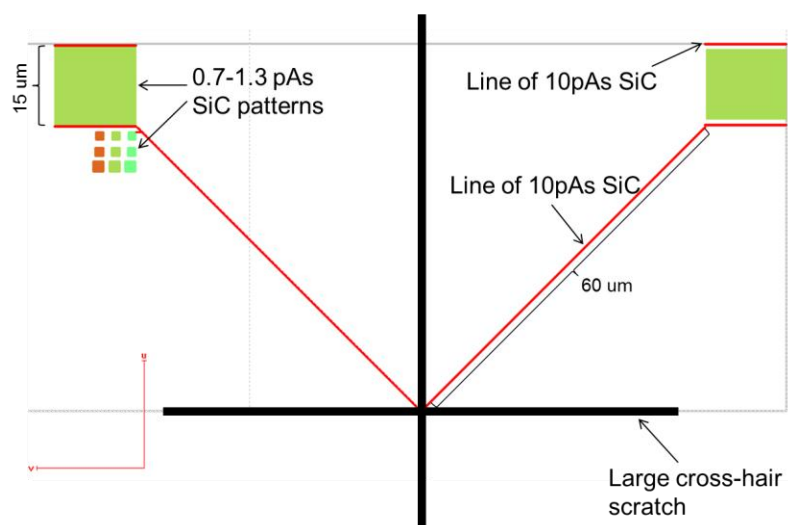
Figure 3-12: Schematic showing hierarchical fiducial marks.
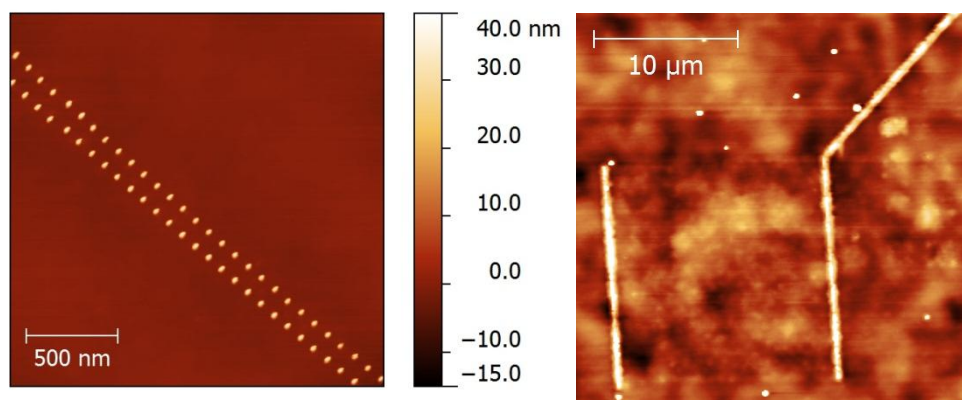
Figure 3-13: Large bumps are patterned via EBL with 10x dose as fiducial markers.
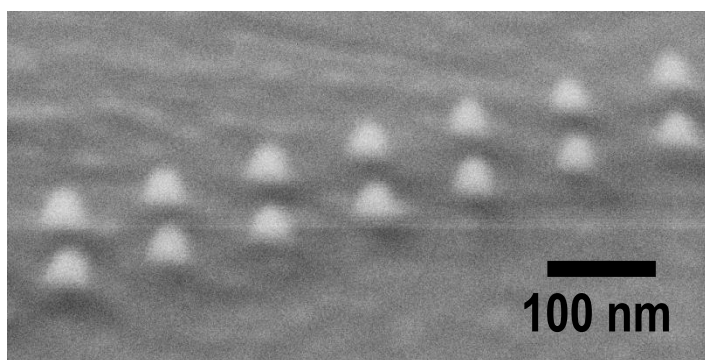
Figure 3-14: Oblique SEM view of 45º fiducial nanodots after carbidization.

3.2.3 AFM tips

In this study, most of the imaging was completed using NT-MDT NSG01 cantilevers. The NSG01 has a moderately weak cantilever (resonant frequency 150 kHz), thus allowing operation at lower driving voltages. As a result, the force constant is also low, 5N/m, compared to that of the stiffer NSG10 tips (240 kHz, 12 N/m). The use of lower force, lower frequency tips allows for increased tip lifetime at the expense of increased sensitivity to absorbed surface layers (e.g. water), although the latter has never caused an issue. Both the NSG10 and NSG01 cantilevers use the same size tip which has a radius of <10 nm. In practice, the best tips have radius ~ 6nm. The tip shape is pyramidal, see Figure 3-15, and the length of the sharp point is specified to be ~50 nm.
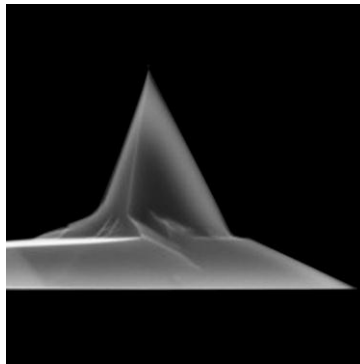
Figure 3-15: SEM image of a typical NSG01 AFM tip showing pyramidal shape.

3.2.4 Island size analysis using AFM data

Post processing of AFM images is a tricky task that can often lead a researcher astray when taking quantitative measurements of surface features. It is very important that one understands the mathematical principles behind each image processing routine built into the software package of choice. All of the work shown here uses the Gwyddion

software package, which is available free and open source (www.gwyddion.net). This software was developed by Petr Klapetek [62,63].

Most raw data sets are non-planar and have a combination of tilt and bow. To account for this, we first use plane leveling and polynomial subtraction (max 4th order). Although greater orders of polynomial subtraction are available, using higher order order subtraction can distort *real* surface topography. In Figure 3-16, six small 2D patterns are shown, note that after flattening the entire 15um field of view is level and we can still see the *real* background surface roughness.
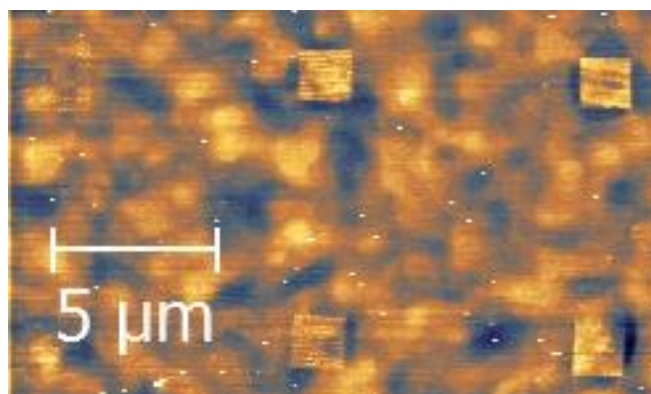
Figure 3-16 Example large area scan for quick identification of patterned arrays. Also note the large amplitude background surface roughness.

By zooming into individual arrays, we can resolve the patterned nanodots. By isolating the surface of each nanodot, one may calculate its containing volume. Of course this would be tedious for a large number of dots, so we turn to a batch processing technique called "flooding". Using the threshold tool, we can select an inverse flood plane that "fills" the surface from the top down (the filled area is marked by a green mask). If we had a perfectly level image, each nanodot could be captured perfectly by

filling to the substrate-nanodot interface. Figure 3-17 shows that for a 100 nm spacing pattern it is relatively easy to mark each nanodot.
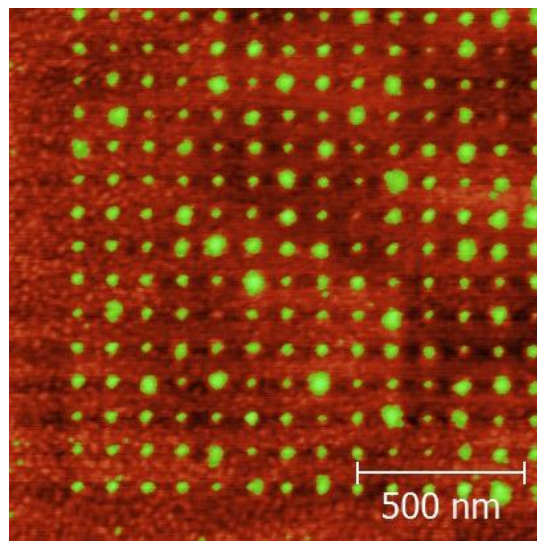
Figure 3-17 Example case showing simple volume analysis via peak finding with Gwyddion software package.

Unfortunately, it is not as simple to mark each nanodot for patterns with finer spacing. At 50 nm and 35 nm spacing the distribution of nanodot sizes is typically broader, and the largest adjacent dots begin to impinge. In addition, even small deviations in background roughness tend to washout the smallest dots. Figure 3-18 shows a worst case scenario for a 50 nm pattern with a broad distribution on a rough surface. Here, many of the dot masks cover multiple dots while several dots are not masked at all.
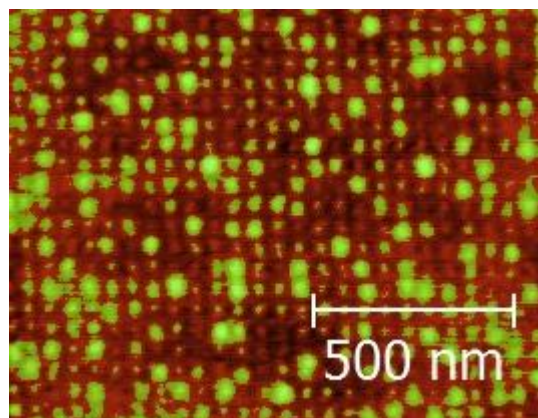
Figure 3-18 In many cases, it was difficult to find a single flood plane for the entire AFM scan. This was especially difficult for narrow spacing arrays.

In this case, it is sometimes necessary to choose two separate flood heights and manually curate the masks to remove all duplicates. In Figure 3-19, one can see that using this method allows identification of a greater fraction of dots. When this process fails (e.g. too many non-masked nanodots, or too many overlapping masks), the AFM scan must be repeated.
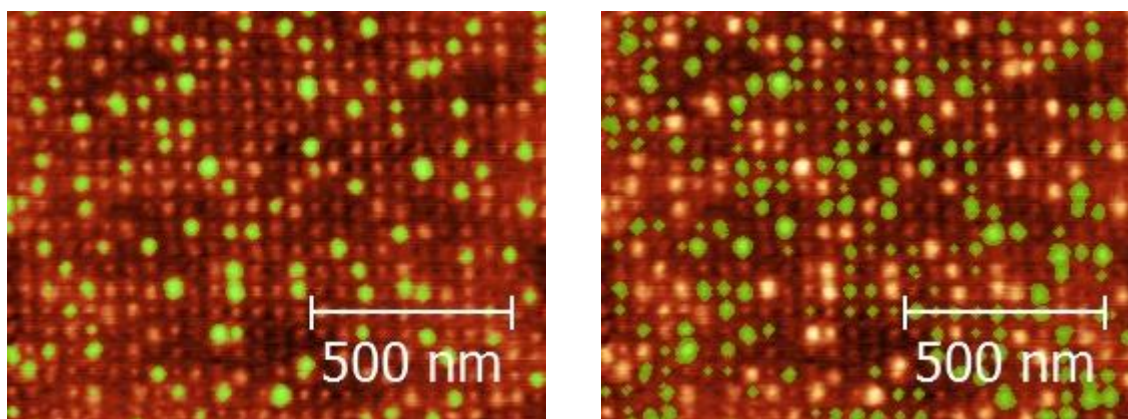
Figure 3-19 Requires using multiple flood heights to pick out different sized features. In (b) a lower flood height was used an the duplicates were removed manually.

Once the masking process is completed, several physical quantities can be extracted from each nanodot. In particular, we collect the nanodot volume, surface area, perimeter, sidewall angle, and max height. In this study, direct comparison of template size distributions is calculated using these volume measurements. For quantitative comparison, an estimate of the error due to tip convolution is derived in Appendix 3 and plotted in Figure 3-20. The volume error is derived as a function of tip radius, island sidewall angle, and island diameter (width). Since the islands investigated here are approximately equal to the tip radius, volume error is numerically calculated to be nearly 15-30%, as indicated by the black star on Figure 3-20. This 'black star' is placed on our typical tip radius (x-axis = 6nm), and at the average volume of an optimal array with the smallest nanodots (y-axis = 300 nm^2).
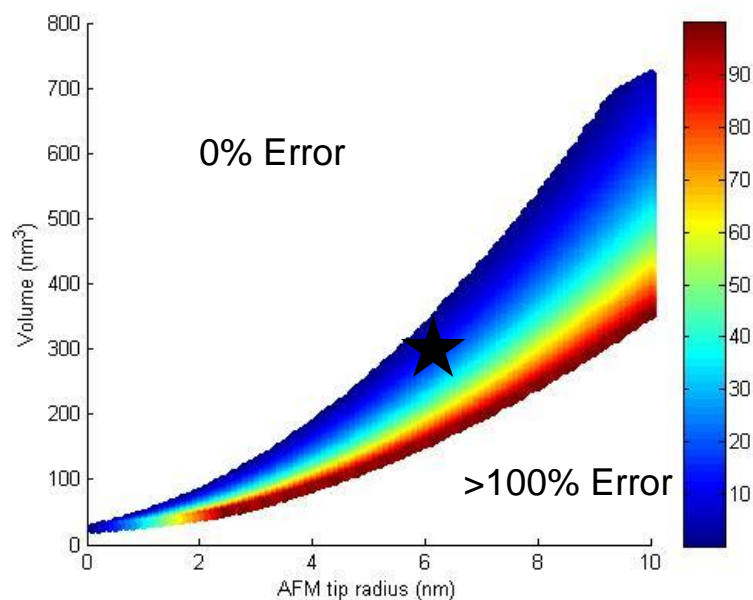
Figure 3-20: Analytical estimation of tip convolution. The vertical colorbar denotes the percent error in volume estimation based on the schematic and calculations in Appendix 3.

Using TEM, we have measured the real width and height of several SiC nanodots, as shown in Figure 3-21. These nanodots range in diameter from 7-15 nm. We compare this range with existing AFM statistics in Figure 3-22 (red box). The TEM observed diameters fall directly in the center of the AFM probability curve, suggesting that AFM dilation of the island diameters is minimal.
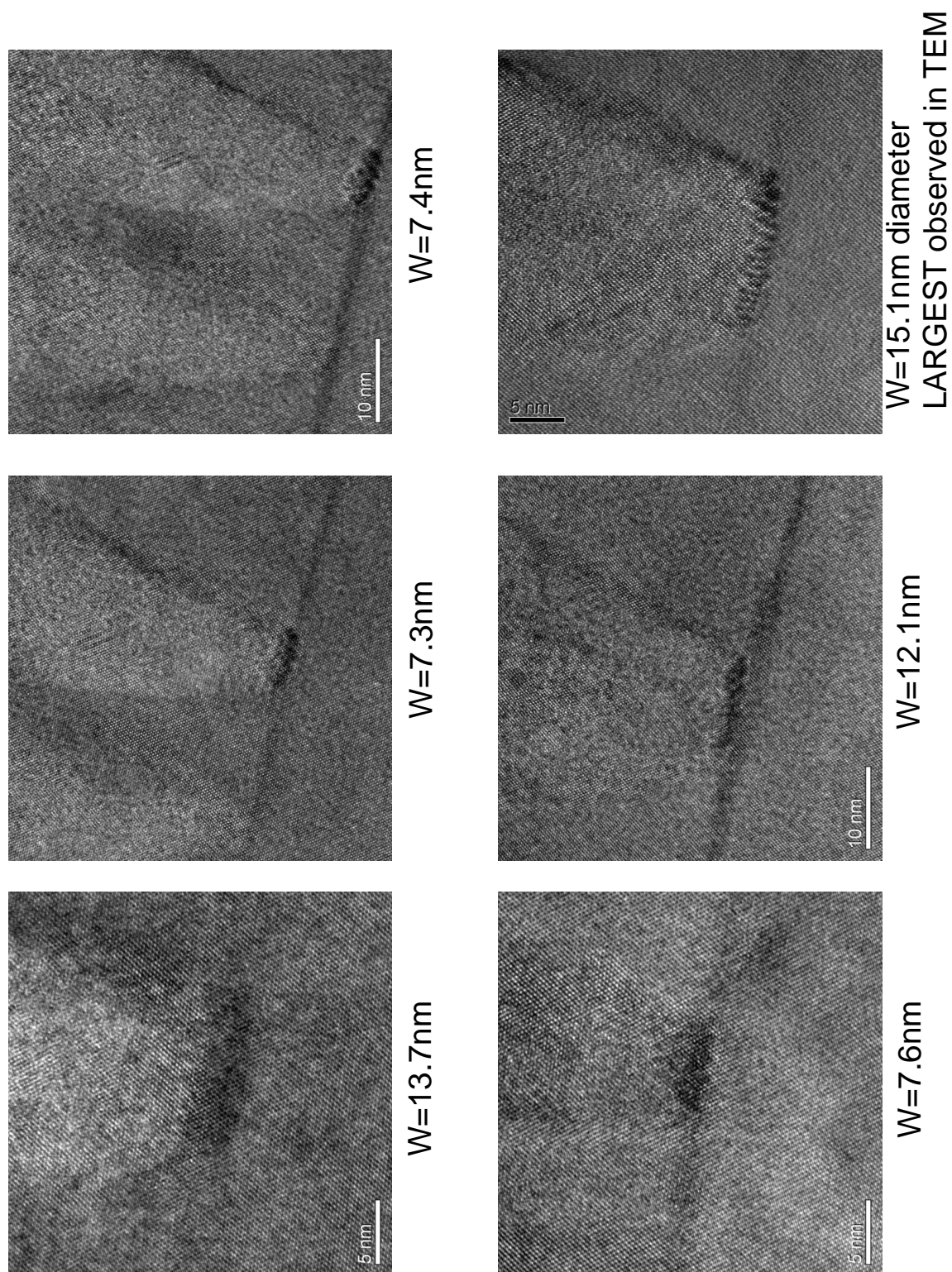
Figure 3-21: Six SiC nanodots as observed with cross-sectional HR-TEM. The width and height can be directly measured for comparison with AFM measurements.
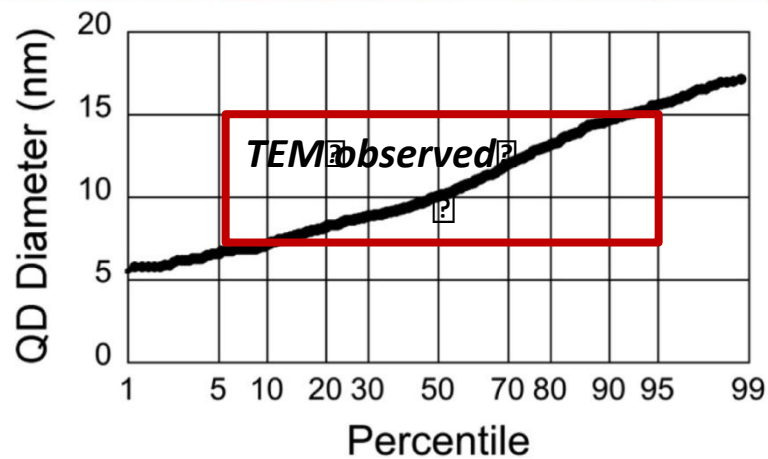
Figure 3-22: Full QD diameter statistics as measured by AFM. The red box encompasses the range of SiC island sizes that were directly observed with TEM.

3.3   Transmission electron microscopy

Transmission electron microscopy is an invaluable tool for precise structural analysis of thin films and nanostructures. Full 3D characterization of material quality is crucial to understand complex growth processes. For this dissertation, two microscopes were extensively used: a JEOL 2000FX operated at 200 kV with a LaB_6 filament, and a Titan 80-300 operated at 300 kV with a tungsten field emission filament. In this section, advanced analysis techniques used in this dissertation will be described in order to facilitate later discussion.

3.3.1   High angle annular dark field

High angle annular dark field (HAADF) is a Z-contrast imaging technique. Using this method, incoherent elastically scattered electrons are collected on an annular detector at high angles (typically 75-150 mrad). Incoherent electrons do not carry phase

information so they cannot constructively (or destructively) interfere; thus the total intensity is the sum of each individual scattered electron.

HAADF is performed with a focused scanning electron probe and the image contrast mechanism is simply the total collected intensity at the annular detector during beam raster. Since specimen information is mapped to real space using select scattered electrons, HAADF is appropriate a dark-field technique. In principle, higher-Z atoms have a greater scattering cross section (much like Rutherford scattering), and generate greater scattering angles. A schematic of the annular detector is shown in Figure 1-22. Examples of HAADF images are shown in Figure 3-24 and 24. Brighter regions represent areas with increased Ge content, owing to its larger Z than Si or C. Furthermore, when the electron probe is smaller than the atomic spacing, it is possible to achieve single atomic resolution (Figure 3-25). In this case, the contrast in each atom column is directly related to the average-Z.
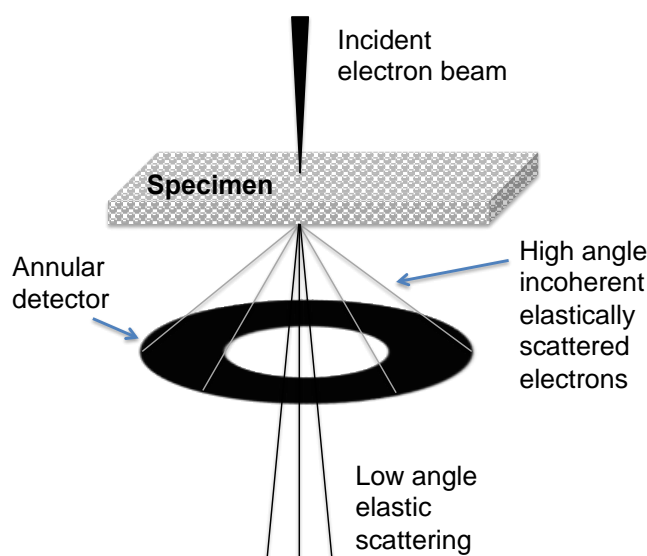
Figure 3-23: Schematic illustration of high angle annular dark field microscopy.
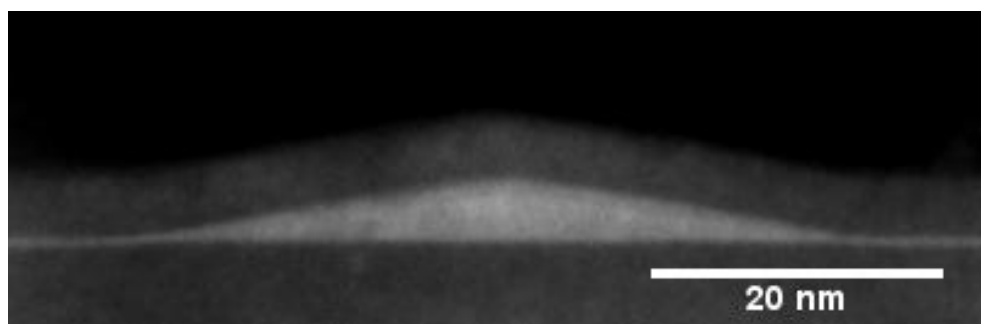
Figure 3-24: Example STEM/HAADF image of a Si encapsulated SiGe hut structure. The greater average Z in the island, due to the presence of Ge, leads to increased high angle scattering and a brighter intensity.
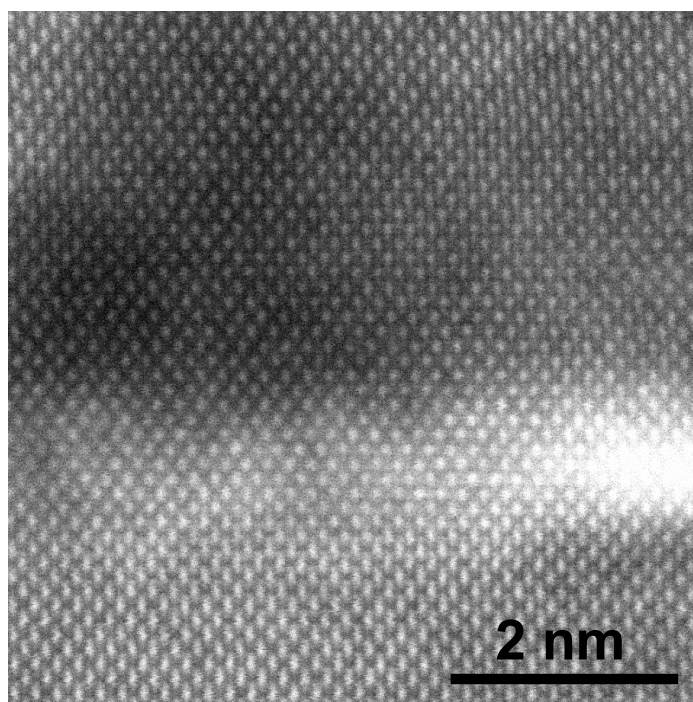
Figure 3-25: Example high resolution STEM/HAADF image from a different specimen showing atomic resolution with Z-contrast. The bright contrast is from higher-Z Ge, the dark contrast is SiC.

When performing STEM/HAADF measurements, it is important to note a few

practical notes. First, when using a highly focused electron beam, thin specimen may be

quickly damaged by either rapid carbon deposition and/or physical stress under the energetic beam. To avoid these issues, it is recommended to plasma clean each specimen prior to insertion in the TEM and to always be aware of your beam position, e.g. always "park" the beam away from your area of interest between image acquisition. Second, in order to achieve atomic resolution and quantitative Z-contrast, the specimen thickness must be <30-40 nm.

3.3.2   Convergent beam electron diffraction

During typical electron diffraction, parallel illumination with the electron beam is used. The electron beam is thus a planar wave with a characteristic Ewald sphere. Alternatively, by converging the beam to a point at the specimen plane, the illumination is now in the form of a cone with multiple convergence angles. As a result, in the diffraction plane, an enlarged disk, rather than a focused point, represents each reflection. An example CBED pattern of Si with a near-<110> zone axis is shown in Figure 3-26.
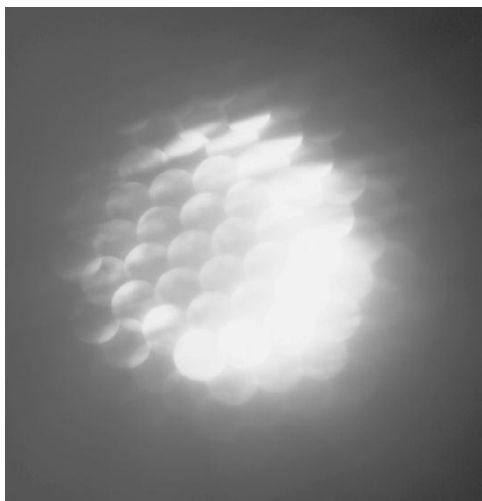
Figure 3-26: Example CBED pattern of Si near the <110> zone axis.

The primary advantage of convergent beam electron diffraction (CBED) is that by using cone-shaped illumination, one can resolve structural data through diffraction from nanoscale regions, <10 nm. Furthermore, by broadening the intensity profile of each diffraction disk, it is possible to resolve small deviations in spot intensity and background information, such as Kikuchi bands. When a specimen is precisely aligned on zone axis, the spot intensity for each diffraction order is uniform and the Kikuchi bands are centered about the transmitted spot. Thus, by measuring the shift in Kikuchi bands, it is possible to determine the exact zone axis for proximal nanoscale regions in a specimen. The relationship between offset zone axes can be interpreted as deviations in crystallite orientation and/or physical bending of the then TEM specimen. For analysis conducted in Chapter 5, we measure deviations in zone axis between adjacent regions (within 100 nm) on a Si single crystal. For our purposes, we assume the sample bending is negligible due to the rigidity of Si.

3.3.3 Sample preparation for cross-sectional TEM

The key to good microscopy is quality sample preparation. Ideally, for high resolution imaging, the specimen must be less than 50 nm thick. In this dissertation work, two methods are used: mechanical polishing [64,65] and FIB lift-out.

A schematic of the process for mechanical polishing is outlined in Figure 3-27. As shown, a Si wafer is cleaved along the <110> direction into 1 mm x 2 mm pieces. These pieces are glued face-to-face using two-part epoxy and then mounted to a pyrex sample chuck with crystal-bond. Next, sides 1-3 are polished individually using diamond lapping cloths; Table 1 lists suggested operating conditions for each polishing stage. It is

important to polish the narrow ends to avoid flaking, see Figure 3-27 (bottom left). After polishing the third specimen edge, mount to a wide hole copper grid and polish the fourth, and final edge. Note: stationary, manual polishing with a 1um diamond suspension is recommended for edges 3 and 4 only.

Table 1: Suggested parameters for specimen polishing.

Specimen side	Lapping film	Speed	Final surface
1,2	80μm	80 RPM	Uniform aligned scratches
	30μm	45 RPM	Uniform aligned scratches
	15μm	45 RPM	Uniform aligned scratches
3	80μm	80 RPM	Uniform aligned scratches
	30μm	45 RPM	Uniform aligned scratches
	15μm	45 RPM	Uniform aligned scratches
	6μm	20 RPM	Few remaining scratches
	3μm	20 RPM	Mirror w/ few scratches
	1μm	10 RPM	Mirror finish w/o scratches
	Diamond suspens.	Stationary	Mirror finish w/o scratches
4	80μm	80 RPM	Uniform aligned scratches
	30μm	45 RPM	Uniform aligned scratches
	15μm	45 RPM	Uniform aligned scratches
	6μm	20 RPM	Few remaining scratches
	3μm	20 RPM	Mirror w/ few scratches
	1μm	10 RPM	Mirror finish w/o scratches
	Diamond suspens.	Stationary	Mirror finish w/o scratches

Polish

2 4 1

3

Diamond
lapping film

(3) Polish each edge
on a diamond lapping
film per the table
below.

Important note:
The cleavage planes of Si are {111},
so each edge will be inclined. When
the specimen is thin, inclined edges
tend to fracture and can damage the
specimen in the latter polishing
stages. To avoid this, it is important
to planarize all four edges per step
(3).

(2) Glue two
specimen together,
film sides touching.
Use 1 drop of glue
from the end of a
toothpick.

Film

(1) Cut two
specimen to 1mm x
2mm pieces

(111)

(001)

[110]

(11-1)

[-1-10]

Figure 3-27: Schematic procedure for mechanical polishing of TEM specimen.

3.3.4 Focused ion beam lift-out

Alternatively, focused ion beams can be used to cut thin specimen from precise locations in a large sample. In this dissertation work, it was critical to lift-out TEM specimen from EBL patterned areas that could not be located by manual polishing techniques[‡]. Figure 3-28 shows a partially milled cross-section using SEM imaging in a dual-beam FIB (left), and a low magnification view of the finished lamella in the TEM (right). To form the cross-section, material around the area-of-interest is milled at an oblique angle exposing two parallel, vertical sides. A needle is then manually positioned on the lamella and "soldered" in place using *in-situ* EBID Pt. Following, the vertical edges are milled and the bottom is undercut in order to release the specimen from the substrate.

Finally, upon lifting out the lamella, it is lightly milled using low energy (1-3 keV) Ga+ ions. This light milling smooths the surface and carefully thins the specimen from 1um down to <30 nm. It is important to note that the FIB milling process can damage the quality of crystalline material in very thin regions of the specimen. In some cases material may be amorphized during the final-milling process; films that are already defective from growth are even more subject to amorphization.

[‡] Cross-sectional TEM specimen preparation by FIB was performed by Prof. James Schiffbauer at the Virginia Tech Nanoscale Characterization Facility and Laboratory (NCFL)
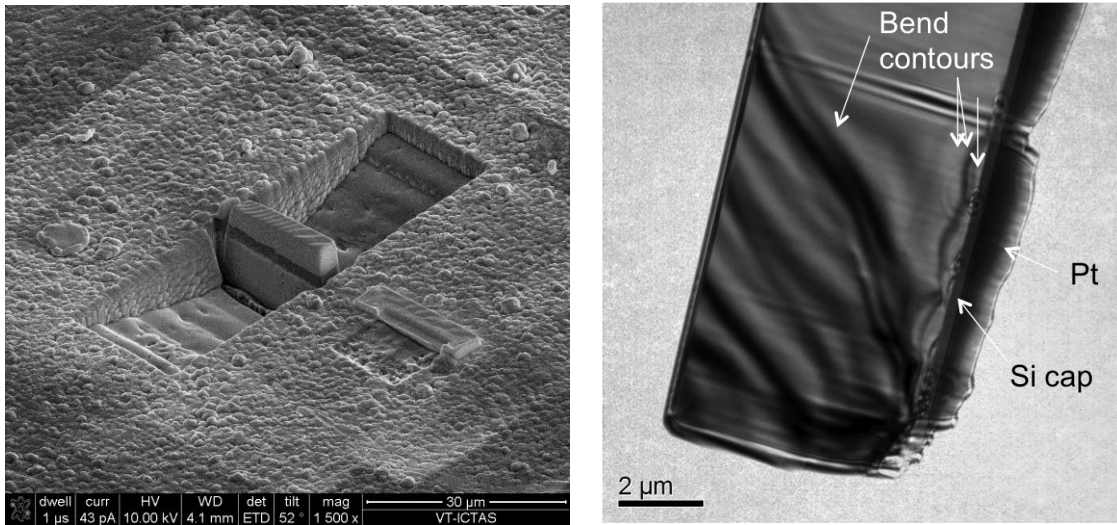
Figure 3-28: (left) Partially FIB milled cross-section TEM specimen. (right) Finished cross-sectional TEM specimen (FIB completed at the Virginia Tech NCFL by Prof. James Schiffbauer).

3.3.5 Beam damage under 300 kV high tension

When using high-resolution imaging techniques and large accelerating voltages, the possibility of specimen beam damage is greatly increased. Any electron that penetrates the specimen with an energy greater than the atomic cohesive energy, is capable breaking bonds and shifting atomic positions. With increased magnification, the electron fluence for a given area greatly increases, thus increasing the number of broken bonds and rate of atomic displacement. The extent of specimen damage will depend on the specimen thickness and the strength (and deformation mechanisms) of the material under investigation [66]. Damage may be worse in films that are already defective or dislocated.

Using the Titan 80-300 at UVA, we have observed the appearance of {113} defects and stacking faults in Si specimen. Figure 3-29 shows a {113} defect growing in the

substrate after about 5 minutes of beam dwell time in this 1um^2 area. Alternatively,

stacking faults may form, as shown in Figure 3-30. These faults have a recognizeable

"triplet" periodicity between diffraction spots in reciprocal space, also shown in Figure

3-30.
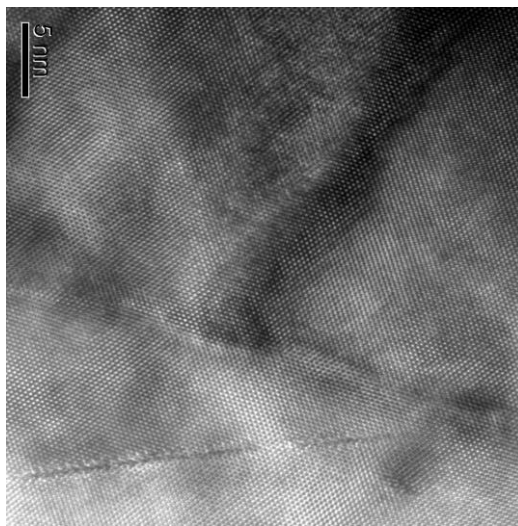
Figure 3-29: Example image of an embedded SiC nanodot. However, under long beam-dwell times, one observes the formation of {113} defects.
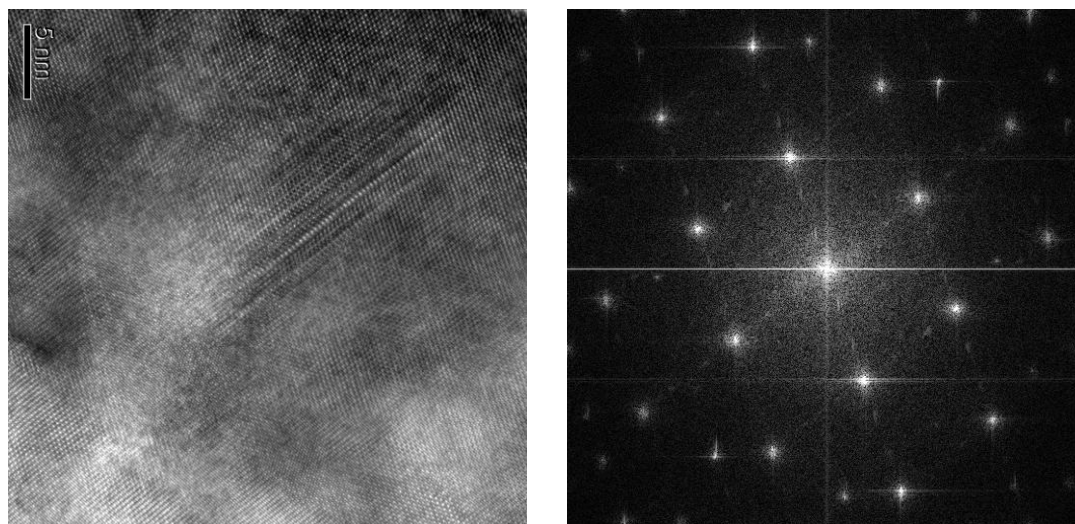
Figure 3-30: Stacking faults can nucleate from beam damage in diamond systems (left). The fast fourier transform (FFT) of the HR-TEM image, shows the triplet periodicity associated with extended stacking faults (right).

3.4 Molecular dynamics models

Molecular dynamics (MD) is a computer model built to simulate the physical interactions of an assembly of atoms (or molecules) based upon the classical Newtonian equations of motion, Equation 3-1.

$$\vec{F_i} \; = \; m_i \vec{a_i} \; = \; m_i \frac{d\vec{v_i}}{dt} \; = \; m_i \frac{d^2\vec{x_i}}{dt^2} \qquad\qquad \text{Equation 3-1}$$

Using these equations, the forces between atoms are calculated numerically and used to determine the kinetic and potential energies of each atom for time steps in the range of 1 femtosecond − 1 picosecond.

To perform an MD simulation, only two inputs are necessary: the initial condition of the system (atomic arrangement and initial velocities) and the interatomic potential for each pair of interacting species. Thus, for a binary system composed of A and B atoms, three potentials are necessary to describe the forces between A-A, B-B, and A-B atoms.

The simplest model is the Lennard Jones potential that describes the van der Waals interactions of a non-interacting monatomic species (i.e. Ar). This potential interaction is plotted in Figure 3-31. At T=0K, the equilibrium interatomic separation is defined by the minima in the potential well and with increasing temperature the maximum atomic displacement is defined by the edges of the well (along the abscissa). The phenomena of melting and vaporization are captured by the asymmetry of the potential well, such that at these high temperatures the maximum atomic displacement tends toward infinity. However, this model does not account for bonding between atoms via electrostatic interactions.
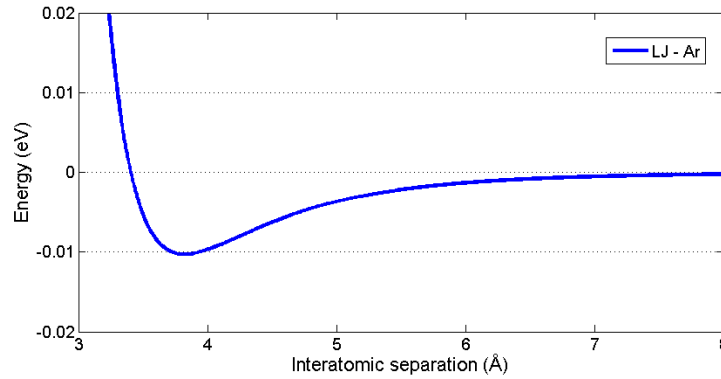
Figure 3-31: Tabulated Lennard-Jones potential for Ar.

To model electronically interactive systems such as metals and insulators, several many-body potentials have been developed including the embedded-atom model (EAM), the Keating potential, and the Stillinger-Weber potential (S-W). The S-W potential was developed specifically for use in semiconductors to derive the tetrahedral bonding arrangement of covalent solids. To do so, this model uses a two-body term to capture the decaying bond strength between adjacent atoms and a three-body term to favor the tetrahedral bond angle ($\cos\Theta_{ijk} = -1/3$). The S-W potential correctly predicts the structure of covalent semiconductors, but cannot reproduce the Si(2x1) surface reconstruction due its deviation from the tetrahedral bond angle.

In this work, we utilize the Tersoff potential which is a *bond order* potential [67–69]. This means that the bond strength between like atoms is not always constant, but depends rather strongly on the local atomic coordination. Thus, the Tersoff potential is more accurate for surfaces and heterointerfaces where the bonding configuration may deviate from the bulk. Figure 3-32 shows a plot of the Tersoff interatomic potential for

Si-Si, C-C, and Si-C as a function of interatomic separation. We use the Si-C potential

outlined for specific use in multicomponent systems [68] along with a volume correction

factor for the cutoff distances [70]. The cohesive energy was used as a fitting parameter

and as a result, we observe the greatest potential well for C-C (diamond) and a reduced

well depth for Si-Si. The Si-C potential is simply a numerical average of its constituents.
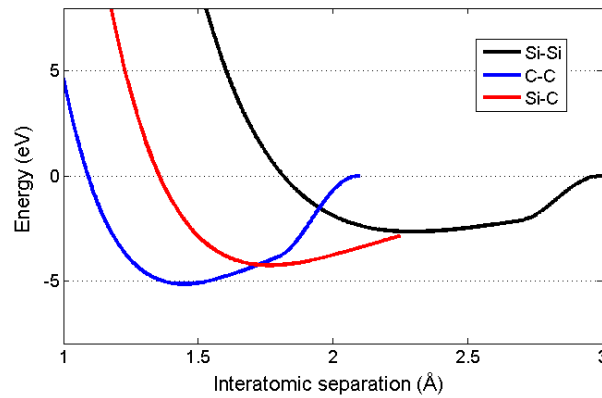
Figure 3-32: The tabulated Tersoff potential based on the parameterization given by
Tersoff [68] and modified by Tang et al. [70]

All simulations run for this work utilize the code developed by the research group

of Prof. Leonid Zhigilei. This code is written in Fortran 90 and runs on the UVa

computing cluster. In particular, we are interested in studying a strain-relaxed interface

between Si and SiC using a *quasi-dynamic* approach [67–69,71–73]. Simulation details

and results are described in detail in Chapter 6.

Chapter 4: Low temperature epitaxial breakdown

4.1   Surface morphological evolution during encapsulation of quantum dots

Ge/Si self-assembled semiconductor quantum dots (QDs) might be spin-functionalized by substitutional incorporation of transition metal dopants such as Mn. However, to suppress Mn clustering and germanide and/or silicide formation, low temperature (<160°C) epitaxial growth of the Ge films is necessary. While this has been successfully performed by others using homoepitaxial growth of GeMn/Ge [40], QD formation via the Stranski-Krastanov mode requires unacceptably high growth temperatures to promote surface mobility.

Investigations into the low temperature epitaxial growth of Group IV semiconductors have provided useful insights on surface-mediated mechanisms for breakdown of the crystalline structure under conditions of limited adatom mobility. Existing research in this area has examined Si homoepitaxy [44,45], Ge homoepitaxy [47,74–76] and to a lesser extent, strained Ge/Si heteroepitaxy [49]. Coincident of the initial goal of this study, we attempted dopant incorporation into QDs via Ge homoepitaxy on a pre-formed three-dimensional canvas of strained Ge QDs on Si (illustrated in Figure 4-1). Quenching of the Ge QDs after formation provides stable QDs in a temperature regime capable of accepting a small flux of transition metal adatoms. Dopant atoms may be trapped within these QDs by subsequent Ge "capping". In this study, we have observed mostly conformal Ge homoepitaxy at T < 150°C on strained Ge QDs, preserving the existing pyramidal morphology. However, the key for realization of

device quality encapsulation is defect-free low temperature epitaxy on inhomogenously strained/faceted QD surfaces.

A desired result of this study is to determine the critical low temperature epitaxial thickness, h_c, during encapsulation as a function of local strain and/or growth facet.
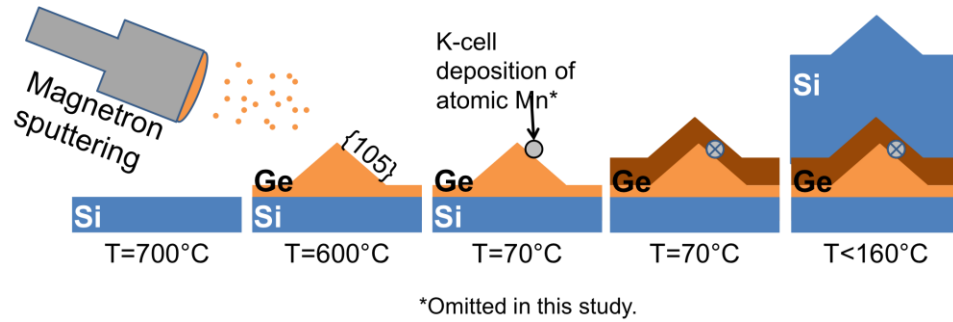
Figure 4-1: MBE growth procedure for Ge QD growth and low temperature epitaxial encapsulation of Mn.

4.1.1   Experimental methods

Ge/Si(001) and $Ge_{0.5}Si_{0.5}$/Si(001) QDs were grown via ultra-high vacuum molecular beam epitaxy (MBE) (base pressure = 10^{-10} Torr). Alloy dots are grown to provide larger islands that facilitate detailed transmission electron microscope observations of the breakdown interface. Ge (GeSi) heteroepitaxy proceeded at 600℃ (740°C) via (co-)deposition of Si and/or Ge with a total flux of 0.1-0.3 Å/s to a thickness of 8.5 Å (31 Å). The surface was then cooled to 160°C for 30 min in UHV for Ge and/or Si capping at 0.1 Å/s. The capping temperature of 160°C was estimated based on prior thermocouple-based calibrations of temperature vs. heater current. This growth temperature was chosen to provide a measurable epitaxial breakdown thickness (h_1)

relative to Si(001) homoepitaxy which was experimentally determined by Eaglesham to be approximately 30 nm [44]. We examined multiple Si cap thicknesses between 10 and 85 nm.

4.1.2   Initial surface analysis studies via AFM

At the beginning of this study, *standard* Ge QDs were grown at 600ºC and cooled to 160ºC for low temperature encapsulation with additional Ge. Deposition at such low temperatures is expected to yield surface roughening caused by kinetically limited adatom diffusion and the rapid nucleation of defective material [44,46,47,75,77]. To our surprise, AFM surface analysis of samples with at least 42nm capping thicknesses shows negligible change in the shape and size of the QD morphology, see Figure 4-2. The surface angle histograms are calculated by extracting the local slope from orthogonal directions for each AFM data point (x,y) and determining the resultant surface normal[§]. We find that the maximum angles positioned at the half-max correspond with the expected 11º and 25º facets of the {105} and {113}. Since no shift is observed in the location of these surface angles, one might expect that the faceting behavior is fully intact, however this is in disagreement with the real time surface diffraction via RHEED. Figure 4-3 shows that after 25 nm of low temperature Ge overgrowth, the surface is completely amorphous.

[§] The Matlab code can be found in Appendix 4.
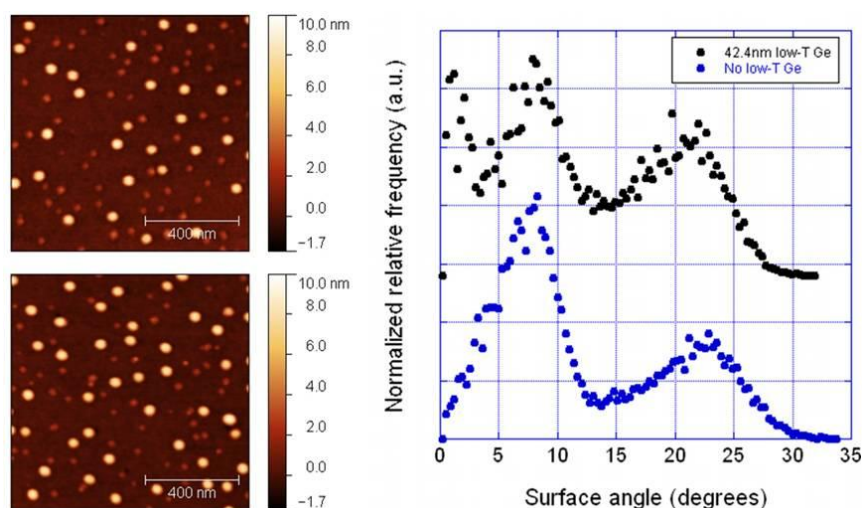
Figure 4-2: Representative AFM images and extracted surface angle histograms of QDs with increasing low-temperature Ge thickness showing negligible effect on surface morphology. Relative changes in peak intensity are due to statistical variation in the relative hut and dome island distribution from day-to-day.
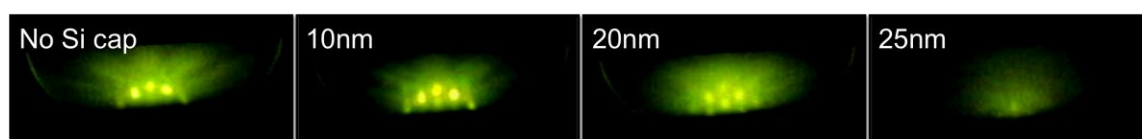
Figure 4-3: RHEED during low temperature Ge/Ge(QD) encapsulation. Before capping, the diffraction pattern shows 3D diamond cubic transmission spots along the <110> zone axis. Kikuchi bands and main spots blur during deposition and are completely lost after 25 nm.

4.1.3 Preliminary TEM investigation of Ge/Ge(QD)/Si(001) nanostructures

To assess the structural evolution of the low temperature Ge encapsulated QDs,

we performed cross-sectional HR-TEM using the JEOL 2010F[**]. The Ge indeed

transitions to an amorphous structure during the low temperature growth phase. The

[**] This TEM measurement was conducted with the help of Dr. Prakash Palanisamy (currently at Intel-Portland).

crystalline-amorphous interface is found to be quite rough (Figure 4-4A), surprising given the conformality of the Ge overlayer. Additionally, isolated positions have extended epitaxial thicknesses before amorphous breakdown, as seen in Figure 4-4B. The width of these regions is roughly equivalent to that of the pre-deposited QDs, but since the QDs and the cap are chemically indistinguishable, it is not possible to correlate extended epitaxial thicknesses with the local morphology.
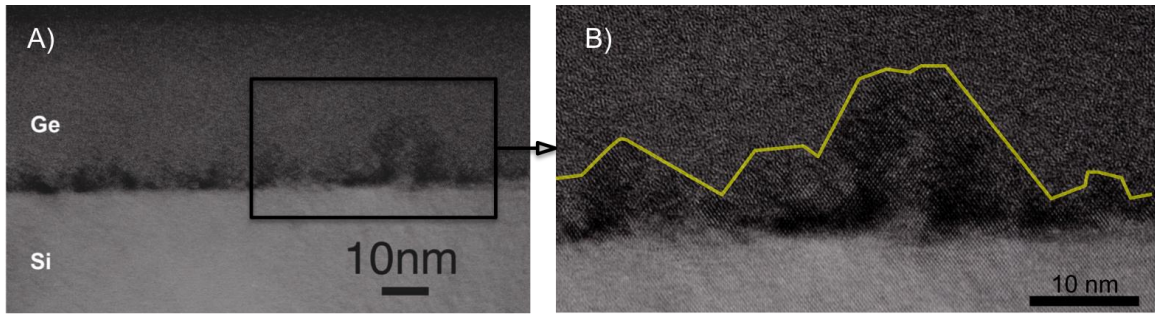
Figure 4-4: Cross-sectional HR-TEM of low temperature encapsulated Ge/Ge(QD)/Si(001) films.

In order to proceed with this work, we chose to study Si encapsulation of larger, $Ge_{0.5}Si_{0.5}$/Si(001) alloy QDs. Since GeSi alloy QDs exhibit the same faceting behavior [78], and Si has a lower mobility than Ge at reduced temperature, this system allows us to establish a lower bound for future low temperature epitaxial growth studies. Additionally, the use of Si/GeSi/Si(001) allows both Z-contrast and larger QD surface facets for ease of TEM imaging. The results of this modified study are presented in Section 4.2.

4.1.4 Room temperature Si homoepitaxy

At the limit of room temperature growth, step-flow is observed beyond film thicknesses of 3nm. This epitaxial thickness is greater than the predicted critical thickness for Si homoepitaxy at 25ºC [44]. Monolayer step heights of 1.36A were resolved with AFM, as shown in Figure 4-5. This observation lends confidence to the quality of our low temperature growth processes.
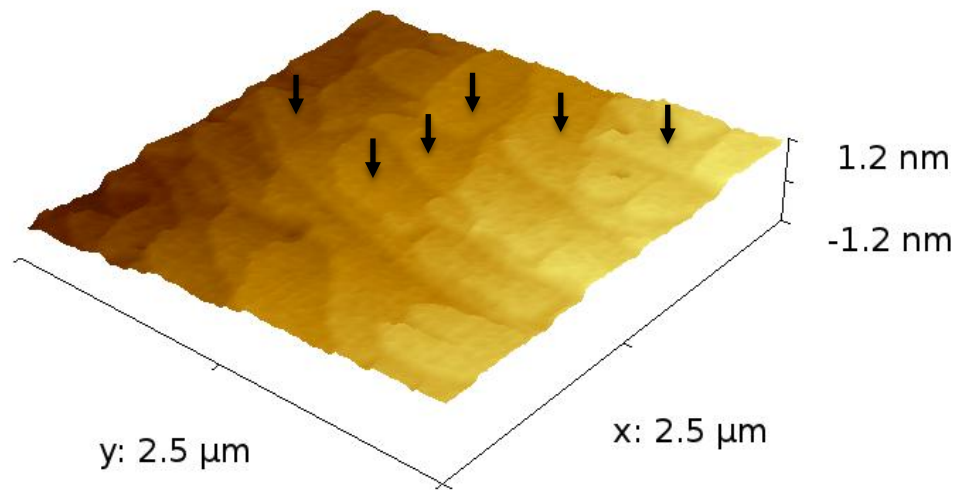
Figure 4-5: Step-flow growth during room-temperature Si(001) homoepitaxy. Several terraces are denoted with black arrows.

4.2 Epitaxial breakdown during Si overgrowth of GeSi quantum dots

To gain additional insight into the correlation between strain, growth orientation, and epitaxial critical thickness, we examine low-temperature growth of Si "capping layers" on GeSi/Si (001) self-assembled quantum dots. We pose the question of how epitaxial breakdown processes are modified for low-temperature growth of Si over quantum dots, which notably present different growth facets, inhomogeneous misfit

strain, and a pre-roughened surface morphology on the mesoscale. While low temperature homoepitaxial growth has been extensively studied by others on a variety of semiconductor surfaces, an investigation of the epitaxial breakdown interface on inhomogeneous surfaces should contribute to a more fully-developed understanding of the mechanisms for breakdown.

A variety of mechanisms for epitaxial breakdown have been suggested, including the role of defect accumulation [79], continuous breakdown [80], hydrogen absorption [48,81], and kinetic roughening [44,47,74–76,82–85]. A common picture emerging from these studies is that during low temperature homoepitaxial growth on (001) surfaces of Group IV semiconductors, {111} facets are eventually exposed at the growth surface upon which extensive faulting can occur, directly leading to breakdown of epitaxy. Here we utilize well known GeSi/Si(001) QD nanostructures as a 3D canvas for low temperature epitaxial overgrowth of Si at 160°C. This system allows us to examine the roles of both inhomogeneous strain and local island faceting on the epitaxial breakdown process. A similar study was recently reported where Si overgrowth was carried out at higher temperatures than used here, resulting in larger breakdown thicknesses [86]. That work attributed breakdown to fault generation on {111} through strain-induced partial dislocation introduction. By reducing the Si growth temperature, we can better pinpoint the localized regions for the initiation of breakdown during overgrowth. We find that breakdown occurs much earlier over {113} island facets, but other facets such as {105} do not affect the breakdown relative to {001}, and perhaps even augment the critical thickness. In addition, no effect of local strain variations on the epitaxial breakdown thickness are observed here.

Bratland, et al., have recently ascribed kinetic roughening effects as the primary

mechanism for {111} faceting and eventual epitaxial breakdown during Ge

homoepitaxial growth [47]. They showed that shallow growth mounds form due to the

presence of Erlich-Schwoebel (E-S) barriers and where mound intersection occurs,

local {111}-faceted cusps form. Extensive faulting occurs during subsequent growth

on these {111} cusps, followed by an abrupt transition to the amorphous structure

at larger thicknesses. They define h_1 as the mean initial thickness at which defect

generation begins, corresponding to the formation of {111} cusps, and h_2 as the

mean thickness at which the layer has become fully amorphized. We also observed

nanoscale mound formation on the surface of our Si cap layers, at length scales much

smaller than the buried quantum dots, that appear to be intimately linked to epitaxial

breakdown.

4.2.1   Epitaxial breakdown and defect delineation

AFM topography scans with representative line profiles are shown in Figure 4-6,

comparing morphology of samples with and without low temperature Si caps. For our

growth conditions , island areal density is ~60 um^{-2}, showing a clear bimodal distribution

of Stranski-Krastanow "pyramids" and "domes" with average diameters of 140 nm and

160 nm, respectively. The pyramid and dome morphologies, which form in order to

reduce the compressive biaxial lattice mismatch strain, are ubiquitous in Ge_xSi_{1-x} alloy

QD growth [27,78]. Pyramids are bound by {105} facets, while the domes are bound by

{113}, {15 3 23}, and {105} facets [87]. AFM shows that a 12 nm thick Si cap grown at

160°C leads to some broadening of the surface features, but most of the representative surface angles are retained. Furthermore, the roughness of the wetting layer regions between the dots, and on the dot facets appears to be identical for the capped and uncapped samples. Hence the surface of the Si cap layer is almost completely conformal to the underlying quantum dot array, despite the occurrence of partial amorphous breakdown as we will demonstrate below. We have also found this to be true for complete epitaxial breakdown of low temperature Si and Ge overlayers on Ge/Si(001) and GeSi/Si(001) quantum dot surfaces.
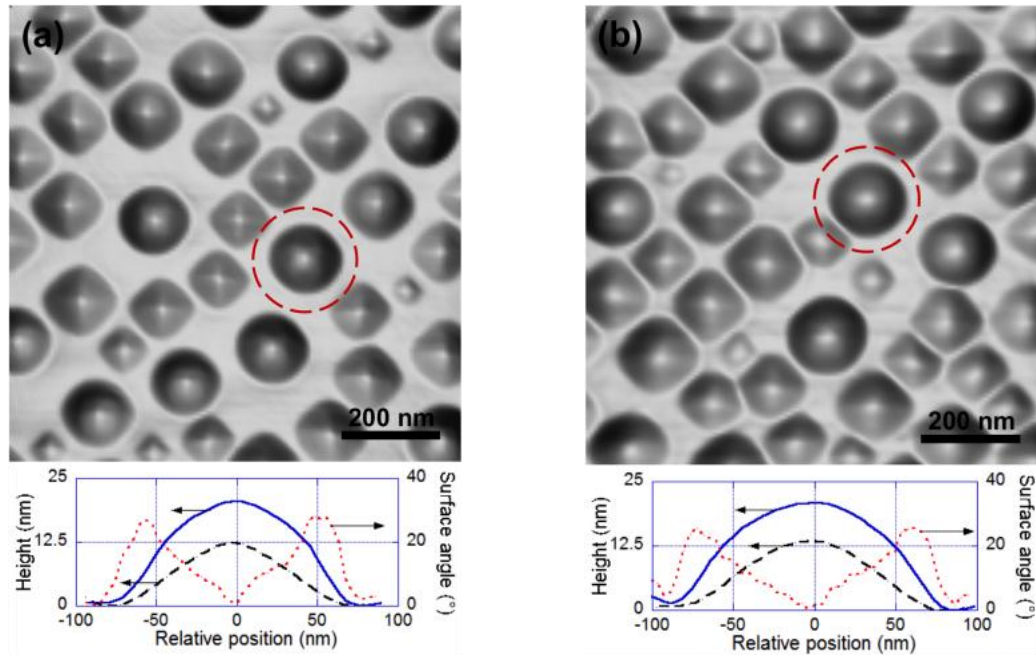
Figure 4-6: AFM topography images and associated linescans of typical pyramids (black dashed line) and domes (solid blue line). The red dashed lines on the graphs are associated with the local surface angles of the indicated domes in the [110 azimuth]. (a) uncapped $Ge_{0.5}Si_{0.5}$ quantum dots. (b) Morphology after low temperature growth of a 12 nm Si cap, where partial amorphization has occurred as indicated by RHEED and TEM.

To examine how epitaxial breakdown and amorphization of the Si cap correlate with the underlying quantum dots, we employed a defect-sensitive organic peracid etching (OPE) technique [88,89]. OPE consists of premixed $CH_3COOH:H_2O_2$ (3:1) and HF. This solution creates peracetic acid that behaves as a weak oxidizing agent. The oxidation rate is determined by the H_2O_2 concentration and subsequently limits the rate of material removal by HF. The mechanism of accelerated material removal at defect sites is based upon increased potential energy due to missing bonds, impurities, and dislocation strain fields. Selectivity for defective Si is only about 2x over that of perfect Si, which has an approximate etch rate of 3 nm/min, so some etching of "good" material is unavoidable. Figure 4-7 shows the OPE etched surface of the Si capped sample after 1 minute in solution. The Si cap over the pyramids and wetting layer exhibits modest, relatively uniform etching. But the Si over the domes shows significant, inhomogeneous etching, indicating the localized formation of defective and/or amorphous structure in these regions. In particular, the linescan comparison shown in Figure 4-7 demonstrates that etching was fastest over regions roughly over the {113} facets of the buried dome clusters. The etched GeSi dome profiles exhibit sidewall angles of 40° although measurement of such steep angles is limited by the finite radius of the AFM probe.
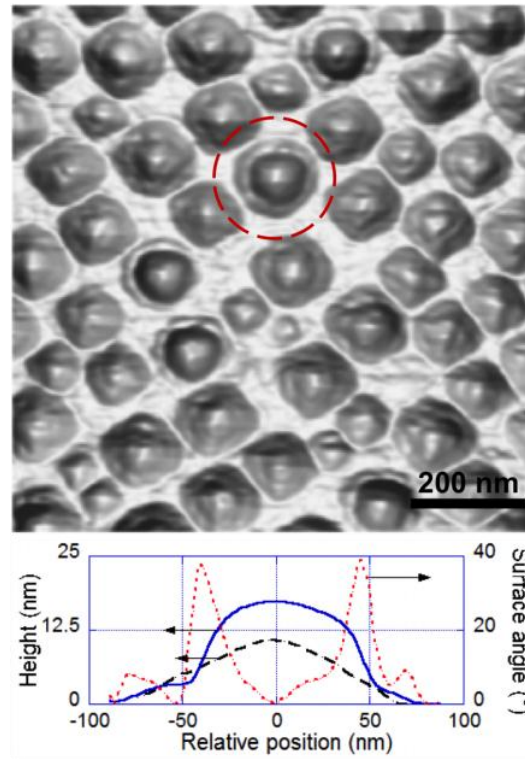
Figure 4-7: AFM topography and associated linescans of SiGe islands with a defective epitaxial Si cap after OPE etching for 1 minute. A typical hut (black dashed line) and dome (solid blue line) are shown along with the local surface angles of the etched dome.

4.2.2   The breakdown interface

To provide a detailed microscopic view of the defective epitaxial breakdown interface, we performed cross-sectional TEM and EELS analysis. For the 12 nm thick low temperature Si capping layer, for which RHEED indicates partial amorphization, we observe defect free epitaxial growth above the (001) wetting layer and the {105}-faceted pyramids [90], as shown in Figure 4-8. In agreement with AFM, the Si cap appears perfectly conformal to the underlying pyramid. Epitaxial breakdown is observed to occur above dome clusters, as shown in Figure 4-9, but the breakdown front is localized. Similar breakdown morphologies were observed over all 8 domes surveyed in the XTEM

specimen. Underfocused bright-field imaging in Figure 4-9(a) shows a buried dome, where the position of the Si surface is readily identified (black arrows) by examining through-focus conditions. The XTEM indicates that the Si cap surface is again conformal to the buried dome, in agreement with AFM. Si EELS mapping (not shown) confirms this result. Figure 4-9(a) shows that epitaxial breakdown occurs along the side facets of the dome island, in agreement with the OPE results of Figure 4-7. Note that at the apex of the GeSi dome, the crystallinity of the 12 nm cap is fully retained.
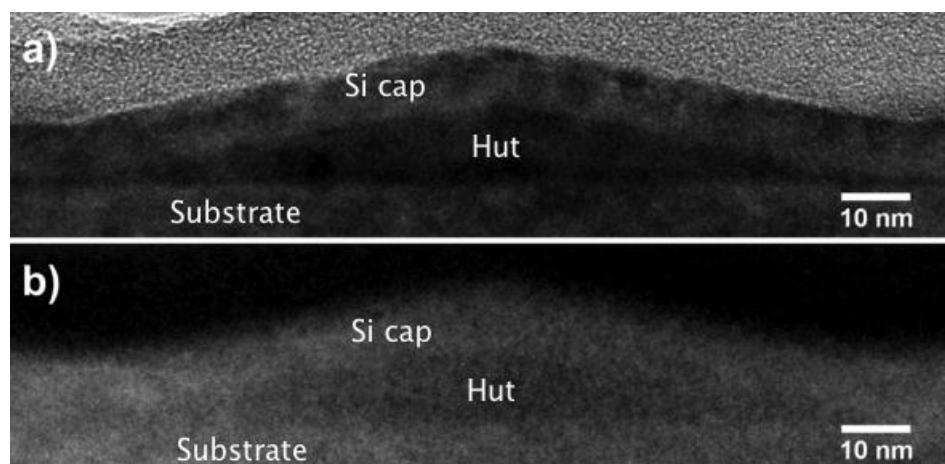
Figure 4-8: TEM bright field cross-sectional image of a buried GeSi pyramid and its associated Si EELS map, for the sample capped with 12 nm Si at 160°C. The mottled contrast in the bright field image is due to specimen thinning artifacts.
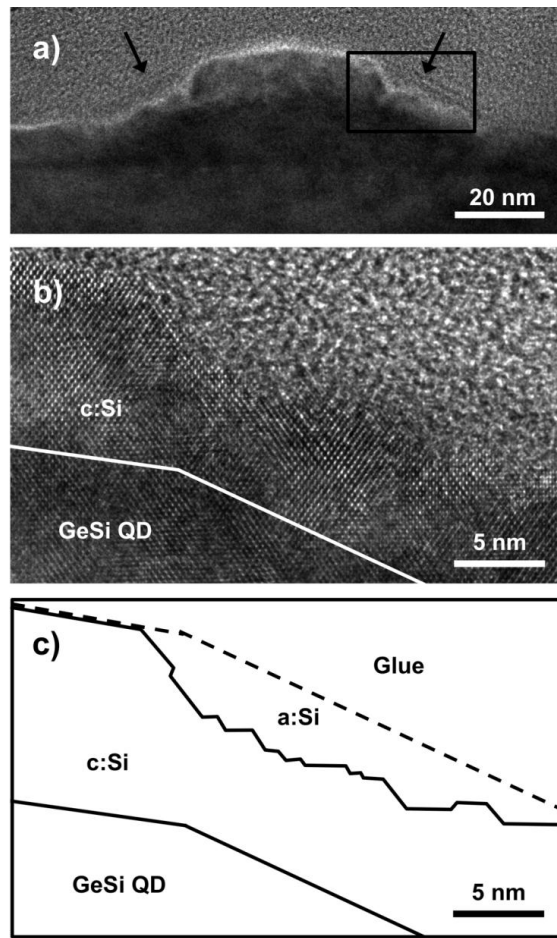
Figure 4-9: Cross-sectional TEM of a GeSi dome, arrows in (a) indicate the amorphous Si-cap free surface in underfocused conditions ($\Delta f=-500$ nm). HRTEM of the crystalline-amorphous interface from the indicated box is shown in (b) and a corresponding sketch of this interface is shown in (c).

A high-resolution TEM image of the breakdown interface is shown in Figure 4-9(b) and shown outlined in Figure 4-9(c). The breakdown interface is composed of alternating {111} and {001} facets, with an average slope to the interface of about 25°, corresponding to an overall {113} facet. This correspondence suggests that Si overgrowth on the prominent {113} facet of the GeSi dome cluster is where epitaxial

breakdown first nucleates. Reduced epitaxial breakdown thicknesses on {113} surfaces have been observed by others [91,92].

To examine the complete transformation to defective epitaxy (h_1) across the sample, an 85 nm Si cap was grown at the nominally identical temperature of 160°C. Figure 4-10 shows a cross-section micrograph of typical pyramid and dome islands. Breakdown begins over the wetting layer at a thickness $h_1 = 47$ nm above the planar wetting layer regions, and above the {105} faceted pyramids. This breakdown thickness is also retained at the dome perimeters. However, Figure 4-10 clearly shows that breakdown occurs earlier over the dome {113} facet (as shown for the 12 nm cap), while over the apex of the dome, h_1 is estimated to be 55 nm, even larger than over the wetting layer regions. It must be acknowledged that the latter estimate is challenging due to the complex contrast in this region of the XTEM specimen.
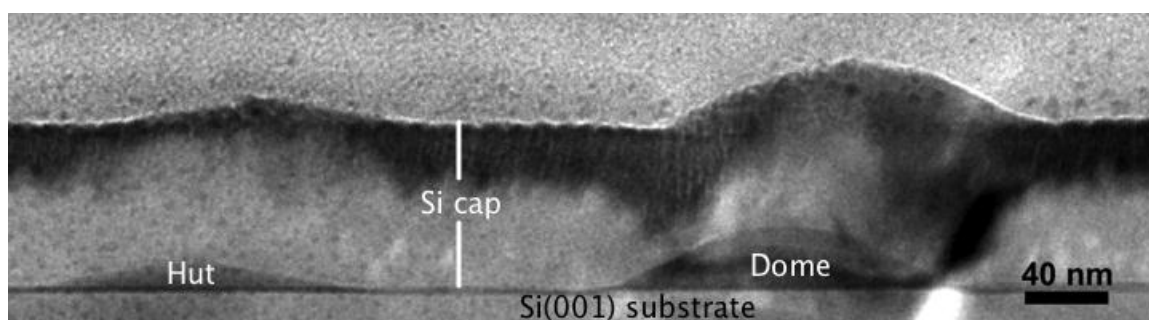
Figure 4-10: TEM bright field cross-sectional image of GeSi islands capped with 50 nm of Si at 160ºC. The sharp contrast features on the far right are associated with a bend contour of the thin specimen and are not related to the defective epitaxial region.

Our AFM measurements of the 85 nm thick Si cap surface (not shown) indicate that the cap conformally replicates the underlying islands, with no increase in local-scale

roughness. However, Figure 4-10 demonstrates that the surface of the thick cap actually

exhibits a fine-scale scalloped morphology indicating growth mounds have developed at

this thickness. These mounds have a lateral size of about 12 nm over the wetting layer

regions, with a peak-to-valley height of 2-3 nm. Such fine-scale but high-aspect features

were not detected by the AFM tip, which had a nominal 10 nm radius. Further, although

more difficult to visualize, it does appear that mounds are forming on the Si cap over the

dome clusters as well, but these mounds appear to be even smaller, of order 4 nm lateral

size. The presence of mounds over both the (001) and {113} are also indicated by the

cooperative formation of void trails that are readily visible in Figure 4-10.

Finally, we observe two abrupt increases in angle of the h_1 interface above the dome:

from 25° to 54° near the {113}/{105} intersection, and from 54° to 70° directly above the

dome apex. These appear to correlate back to changes in local faceting of the GeSi

quantum dots. The increase to 54° is correlated with a transition from growth over {113}

facets to growth over the domes' {105} facets. The increase in angle towards 70° is then

associated with oriented (001) epitaxy which retards impingement of the bounding

defective sublayer.

4.2.3   Discussion and conclusions

Our clear observation of enhanced epitaxial breakdown of Si over the {113}

facets of the overgrown GeSi domes is consistent with previous reports on Si

homoeptiaxy [92]. In the context of a picture wherein formation of {111} facets, and

associated fault generation, is required to nucleate the amorphous phase, the {113}

structure could be conducive to exposure of {111} planes. The unreconstructed {113} surface consists of single atomic terraces of alternating {111} and {001} [93]. This is shown in Figure 4-11. While the Si {113} is a true facet, and is known to exhibit a stable 3x2 reconstruction at lower temperatures [94], we will assume for simplicity that the reconstruction is broken during low temperature growth. In Figure 4-11, a single monolayer-height step is shown, which generates a 2-unit wide {111} facet. Hence, any local roughening of the {113}, e.g., step bunching or mound formation, naturally generates extended {111} facets. While this simple picture provides an appealing qualitative explanation for why epitaxial breakdown thickness is reduced on the {113}, we cannot say for sure that the reconstruction has been broken during low temperature growth of Si over the GeSi island. It is noted, however, that any tensile strain in the Si cap layer growing over the partially-relaxed island should contribute towards destabilization of the 3x2 reconstruction due to its large inherent tensile bond strain.
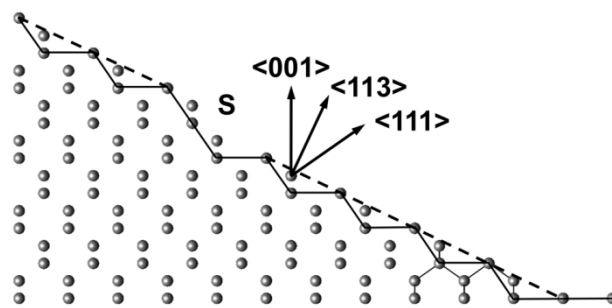
Figure 4-11: Crystallographic orientation of a Si {113} surface. The dashed line follows the average {113} terrace surface, while the heavy black line delineates local {111} and {100} segments. A single monolayer-height step is indicated by an "S" illustrating the ease of generating extended {111} facets.

Bratland, et al. [47], linked nucleation of the amorphous phase to the formation of growth mounds having a critical aspect ratio. The critical ratio was related to a peak-to-valley distance that is larger than the temperature-dependent diffusion length. [47,83] They attributed mound formation to the presence of E-S barriers on the crystalline Ge surface, although their mounds tended to be much larger, and occurred in much thicker films, than observed in our case. We also observe breakdown coupled to mound formation on the Si (001) surface that appears qualitatively quite similar to their work. The presence of E-S barriers on Si (001) is not established, although step bunching and mound formation have been observed previously and attributed to alternative roughening mechanisms [82,95,96]. Additionally, we note that growth mound formation has been observed on *fully amorphous* Ge, Si and metal alloy films [97,98]. In this work we also observe mound formation on {113}. The smaller size of the mounds implies reduced overall diffusivity on this surface and correlates with the smaller breakdown thickness.

We find that the growth mounds are accompanied by void trails (see Figure 4-10), as was observed previously [47]. Void trail formation is intimately linked to local surface roughening and mound formation [97,99]. The trails are tilted by about 15° with respect to <001>. Similarly, the surface-replicas of the huts and domes are all offset in the same direction relative to the underlying GeSi islands, and in the same direction as the void trails, but at an angle of 23°. In the limit of zero adatom mobility, the tilt angle of the void trails relative to the film plane should equal that of the incident flux (in our case, 30°). That the tilting of the mounds is considerably smaller than the incidence angle of the Si flux suggests that some surface transport over the nanoscale mounds is

occurring. The larger tilt angle of the GeSi island surface-replicas is consistent with relatively reduced transport due to the much larger length scale of these features.

Strain does not appear to affect the epitaxial breakdown process in these films. We note that the Ge wetting layer and both the pyramid and dome islands are fully coherent. Growth of Si over the wetting layer will not impose any elastic strain in the Si cap. However, over the islands, which partially relax due to their 3D geometry, there will be local strains imposed on the Si. Continuum elastic modeling indicates that the apex of the dome is expected to exhibit almost complete strain relaxation [32,100,101], and therefore the Si cap should be strained up to 2% tensile when it overgrows the apex; these relative strains are illustrated in Figure 4-12. Another region of potentially large strain in the overgrown Si cap would be above the perimeter of the dome cluster, where the dome and the Si substrate are under excess compression. Similar, but smaller, strains will be imposed in the cap by the pyramids. Careful inspection of several domes and pyramids in our specimen indicates that Si breakdown is not occurring over the apices or the perimeters of the underlying islands.
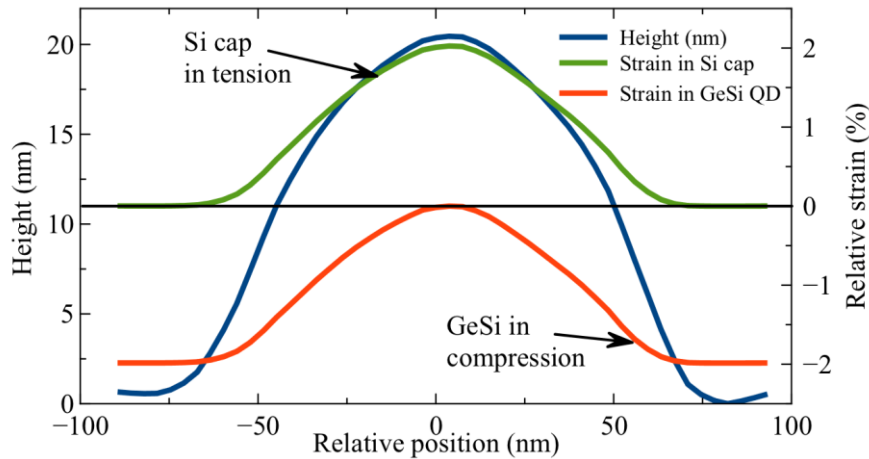
Figure 4-12: Example line scan of a GeSi dome (blue) and corresponding relative strains in the dome (red) and the subsequent Si cap (green).

In recent work by Lin, et al. [86], Si was grown over Ge/Si(001) QDs at 300°C, resulting in $h_1 \approx 30$ nm over the QDs and, we estimate, 100 nm over the wetting layer. Such thicknesses are much larger than observed here due to their higher growth temperatures. They observed stacking faults localized over the buried QDs that appeared to originate at the perimeters of the Ge dome islands, where compressive stress is present in the Si cap. They attributed the formation of faults to passage of partial dislocations due to the stress. We did not observe this breakdown mode, perhaps due to the lower growth temperature used here, where growth mounding and roughening, especially on the {113}, promotes breakdown before the critical thickness for shear-related mechanisms. Also, the Ge content in our islands, and hence the strain in the Si cap is smaller in our experiments than that for Lin, et al. [86] However, though we observe no direct correlation of strain on h_1, we note that strain does impact the relative stability of surface

reconstructions and adatom diffusivity; thus a hybrid picture of epitaxial breakdown involving kinetic- and strain- effects is required.

In conclusion, during low temperature Si overgrowth of GeSi coherently strained islands and wetting layer, we show that the low temperature epitaxial thickness, h_1, depends primarily on the mesoscopic facet orientation of the Si, which is conformally inherited from the islands. Globally, epitaxial breakdown occurs earliest over the {113} facets due to the ease of creating local {111} surfaces associated with step formation. We observe kinetically limited growth mounds on all QD related facets and note that the mean mound width is directly related to the epitaxial thickness and thus to the local surface diffusivity. The small mound size on {113} vis-à-vis {001} implies reduced diffusivity on this surface, further enhancing the tendency to breakdown. Finally, we show that h_1 for Si is independent of coherent strain of at least 2%, suggesting that at these low strain levels the initiation of defects is dominated by kinetic growth mound formation.

Chapter 5: Precision EBID patterning of quantum dots

5.1   Motivation

New device paradigms utilizing logic based on spin interactions in confined

systems have gained considerable interest for the exploration of the basic physics of

quantum structures and of new computing architectures. For example, a linear chain

containing an odd number of antiferromagnetically coupled spins would act as an $S = \frac{1}{2}$

cluster qubit, whose behavior would mirror that of a standard, single spin $s = \frac{1}{2}$

qubit. [10] The advantage of a cluster qubit is that there is greatly reduced sensitivity to

the detailed coupling between spins inside the cluster, and control of magnetic fields to

minimize decoherence is now necessary only on the scale of the cluster length, i.e., about

an order of magnitude increase in length scale for a 9 spin linear cluster. When large

arrays of qubits are created, artificial spintronic band gaps can be realized with electrical

properties that depend purely on the geometrical arrangement [8].

While cluster qubits have the advantage of being much less sensitive to the

intracluster exchange, it is still necessary to stably position spins sufficiently closely to

develop exchange coupling energies comparable to $k_B T$. Recently, Pryor, et al. [7],

predicted observable exchange coupling behavior between electrons localized by adjacent

heteroepitaxial Ge quantum dots embedded in Si. As illustrated by Pryor, and shown in

Figure 5-1, strain-induced changes in the band edges of Ge and Si can lead to formation

of shallow minima in the Si conduction band *above* and *below* the Ge QDs that would

confine electrons. Confinement was sufficiently weak that wavefunction decay lengths

were of order 10 nm. It was shown that for adjacent Ge QDs separated by 24 nm, the

exchange interaction energy could be as large as 1.3 meV.
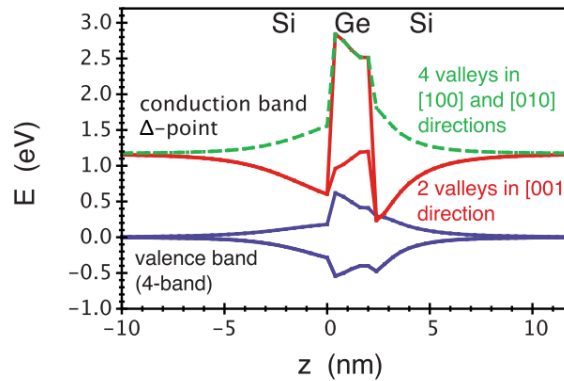
Figure 5-1: Band edge diagram of an embedded Ge QD. Image taken from Pryor et al. [7]

Epitaxial self-assembly of Ge QDs on unpatterned Si (001) at 600°C results in

coherent islands in the so-called pyramid and dome morphologies [21,102]. During the

growth of this film, the first 3-4 ML of Ge grows as a thermodynamically stable planar

wetting layer, and all Ge deposition beyond this critical thickness forms the QDs. Clearly

this process results in QDs with random spatial arrangements. In order to obtain

deterministic placement of dots, directed self-assembly is required.

Guise et al. [4] developed a localized electron beam-induced deposition (EBID)

approach for nanofabrication of carbon dot arrays. In this method, fine-probe electron-

beam irradiation locally decomposed ambient hydrocarbons onto a bare Si (001) surface.

These carbonaceous patterns were annealed in UHV to form ordered arrays of nanodots,

assumed to be SiC, that locally modified the Si substrate surface. When overgrown with

Ge, an island denuded region was observed at the perimeter of these nanodot arrays,

suggesting Ge migration to the pattern sites and directed self-assembly of Ge islands preferentially at the SiC sites [4].

This investigation required that we reproduce the results of Guise et al, using a different molecular beam epitaxy (MBE) chamber, and slightly modified cleaning methodologies. We ultimately obtained arrays of structures very similar to those reported by Guise in addition to aperiodic patterns with reduced pitch (Figure 5-2). Structures with spacing as small as 22.5 nm are readily produced. The MBE growth conditions are reasonably similar to those reported by Guise, et al. [103]

In this chapter we discuss the effects of various process conditions on nanodot uniformity in Sections 5.2-5.3. This is followed by a full structural analysis of the SiC nanotemplate in Section 5.4. Overgrowth of the SiC nanotemplates with Ge and Si is then discussed in Sections 5.5-7 and 5.8, respectively. The chapter then concludes with a description of other interesting observations in Section 5.9.
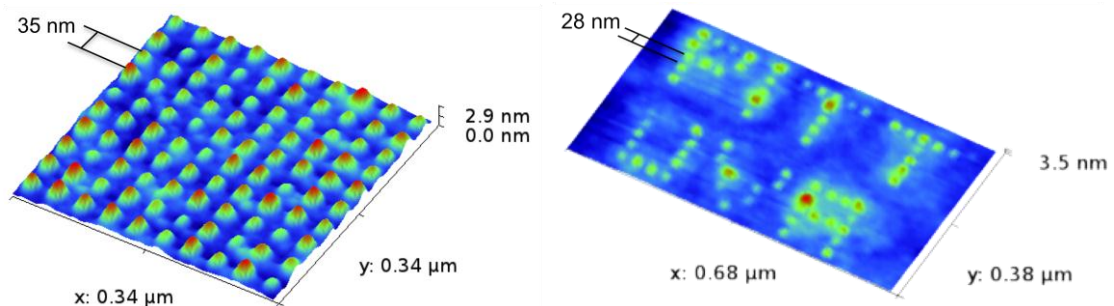
Figure 5-2: (left) Square array of SiC nanodots with 35 nm pitch. (right) Arbitrary SiC pattern with minimum spacing of 28nm.

5.2   Methods

The films ultimately examined here consisted of Si (001) wafers with a template of SiC nanodots, upon which were grown 1.3-3.0 ML of Ge, in some cases followed by a 50 nm Si cap layer. The entire process flow is illustrated in Figure 5-3.

Si wafers with a miscut of 0.1° were cleaned via a modified IMEC/Shiraki process and passivated in the final step by oxidation in a UV-ozone environment. The SiO_2 layer was then stripped in a dilute HF solution immediately before loading into a Raith e_LiNE electron beam lithography system (P_{base}~10^{-7}T) operating with an accelerating voltage of 20 keV and emission current of 21 pA. Focused electron beam irradiation of ambient hydrocarbon adsorbates on the Si(001) surface yielded islands of carbonaceous material, that we'll refer to as C_xH_y. Square arrays of NxN "C_xH_y" nanodots were written, with interdot spacings of 100, 50 and 35 nm, and N as large as 300. Previous studies by Guise, et al. have characterized the size of these islands as a function of exposure time [5] and for this study we used an optimized exposure time of 3-6 ms. Next, the templated nanodots were exposed to UV-ozone to eliminate excess hydrocarbon contamination between the patterned sites. Since this also simultaneously etched the patterned nanodots, UV-ozone exposure was critically controlled to prevent their complete removal. The patterned wafers were then inserted in to the ultra-high vacuum (UHV) molecular beam epitaxy (MBE) chamber (P_{base}=1x10^{-10} Torr) and radiatively heated during an overnight temperature ramp to 500°C. All samples dwelt at 500°C for at least an hour prior to oxide desorption at 780°C. Throughout the deoxidation process, the surface structure was monitored with reflection high energy electron diffraction (RHEED) to ensure that a smooth, 2×1 reconstructed surface developed, as

indicated by the presence of a Laue ring of diffraction spots. During the oxide desorption at 780°C, it will be shown that the C_xH_y nanodots are converted to SiC. Upon cooling to the growth temperature, 1.3 ML of Ge was deposited via magnetron sputtering in 3 mTorr of getter-purified Ar at a rate of 0.1 Å/s. In these experiments, we examine the effect of two differing growth strategies: direct deposition of Ge at 600°C with no further annealing, and Ge deposition at 400°C with subsequent annealing at 700°C. The latter conditions were picked to mimic those shown by Guise, et al., to be optimal for directed self-assembly [4]. For transport measurements and TEM investigation, Ge/SiC features are encapsulated with 50 nm Si at 300°C. This low capping temperature was chosen to ensure conformal Si growth whilst maintaining single crystalline epitaxy [104].
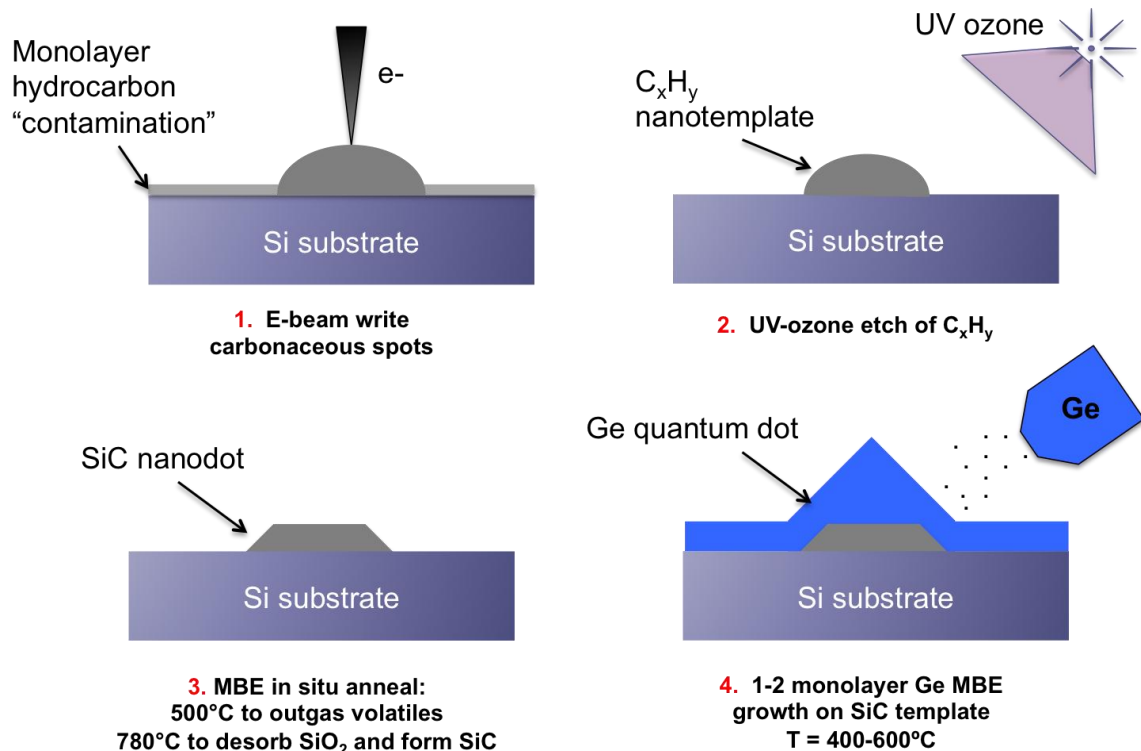
Figure 5-3: Process flow for (1) carbon templating, (2) UV-ozone cleaning, (3) carbidization, and (4) Ge deposition and annealing.

After each templating run, the integrity of the carbon patterning is evaluated using SEM. Figure 5-4 shows typical 2D arrays with 100 nm, 50 nm, and 35 nm spacing. Note that deviations in periodicity along 1-D chains result from EBL stitching errors.
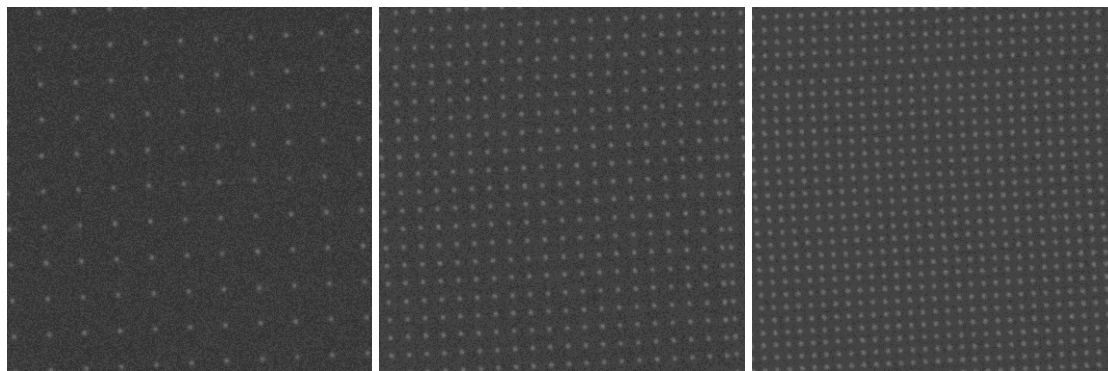
Figure 5-4: SEM images of templated carbon dots. Each image is a 1um x 1um section of larger 2D arrays. From left to right, the template pitch is 100 nm, 50 nm, and 35 nm.

Another important requirement of this work is to obtain the distribution of feature volumes along the process flow, e.g. before and after each deposition and annealing step. To do this we first thoroughly characterized the template morphology after Ge growth, using AFM. Next, we selectively removed Ge enriched content (C_{Ge}>0.6), using H_2O and H_2O_2, [105,106] and then measured the morphology again on the identical area of the template, giving a direct feature comparison. In some cases an HF etch was performed instead, with only minor differences in the results.

Ex-situ atomic force microscopy (AFM) was performed with an NT-MDT Solver Pro-M in semi-contact mode using NSG01 tips with radius < 6 nm. Obtaining accurate topographic measurements of nanoscale islands is non-trivial when the feature radius is near that of the AFM tip. At this small size limit, the extent of tip-convolution is predominantly a function of island aspect ratio [107] (see Appendix 5). Via AFM

measurements, we typically observe Si/Ge/SiC nanostructures with diameters (Ø) between 5-25 nm and aspect ratios of 0.10-0.20. After simple geometrical comparison of AFM measurements with cross-section transmission electron microscopy (TEM), we find that the volume overestimation due to tip convolution is about +20%. We are primarily interested in the relative change in volume as a means of assessing our process conditions, thus the effects of tip convolution are neglected in all measurements, noting that our reported island volumes and linear dimensions represent an upper bound.

Transmission electron microscopy (TEM) was performed on an FEI Titan 80-300 operated at 300 kV. Cross sectional TEM specimen were prepared by focused ion beam lift-out and thinning using a Ga+ beam down to 1 keV. Samples were examined in the <110> zone axis.

5.3   Process development for uniform arrays

For device applications involving interactions between quantum dots, such as exchange coupling or tunneling, it is critically important to control the variability in size and spacing of the composite Si/Ge/SiC/Si(001) patterned nanostructures. While control of template *spacing* is predominantly limited by the resolution of the EBID process, the composite island *size* depends on all subsequent process steps. Two aspects in this process are of key importance – the UV-ozone clean and the detailed thermal budget seen by the template. In particular, a relatively low-temperature dwell at 500°C, which was used to drive off adsorbates from the sample prior to desorption of the passive oxide at 780°C, had a surprisingly strong effect on the final size, and the distribution of sizes, of

the templated features. We have iterated on different Si surface preparations, sample transportation times, alignment marking systems, EBL exposure parameters, and UV-O_3 exposure conditions.

5.3.1 EBID dose effects

It was first critically important to determine an EBID carbon dose that would maintain pattern fidelity throughout the sample cleaning process yet result in discrete nanodots. van Dorp and Hagen have thoroughly reviewed the EBID process, including the time, volume, and height evolution of various material deposits. [38] In general, the deposit height grows at a greater rate than the diameter[15], and through accurate control over the voltage and supply of the deposition species, it is possible to modulate the aspect ratio.

Guise performed a thorough investigation of carbon EBID dose parameters to identify an optimal range of energies and dwell times to create ideal features with 35 nm spacing. [5,6] The total electron-substrate interaction volume scales with acceleration voltage. Increased voltage results in deeper substrate penetration and lateral scattering forming a "teardrop"-shaped interaction region. Each interacting electron generates back scattered electrons, auger electrons, and/or secondary electrons. Secondary electrons are the most abundant emitted species and have an energy range of 1-10 eV. [38] These energies are capable of breaking C-C and C-H bonds and are thus responsible for the EBID process. Secondary electrons are emitted from an area roughly equivalent to the projected area of the teardrop interaction volume. Thus, with increased energy, the width

of the possible EBID area also increases, causing larger carbon deposits. Guise found that an accelerating voltage of 20keV provides an optimal EBID area.

Furthermore, Guise studied the exposure time range of $10^2 - 10^6$ µs. [5] The trends in deposit size were replicated at the University of Pittsburgh, revealing an optimal dwell time of 2-3 x 10^3 µs. Depending on beam current, which varies with the lifetime of the electron filament, the optimal dose factor falls in the range of 0.7-1.3 pA-s. AFM images of 2D arrays with this dose range are shown after cleaning and carbidization in Figure 5-5. In the low-dose range, many dots are lost to the cleaning and carbidization process due to evaporation and carbon-coarsening (as will be discussed later). And in the high dose range, many of the nanodots begin to impinge upon each other and have an average diameter >10 nm. Most SiC nanodots used for analysis here, where deposited with an optimal dose of 1 pAs.
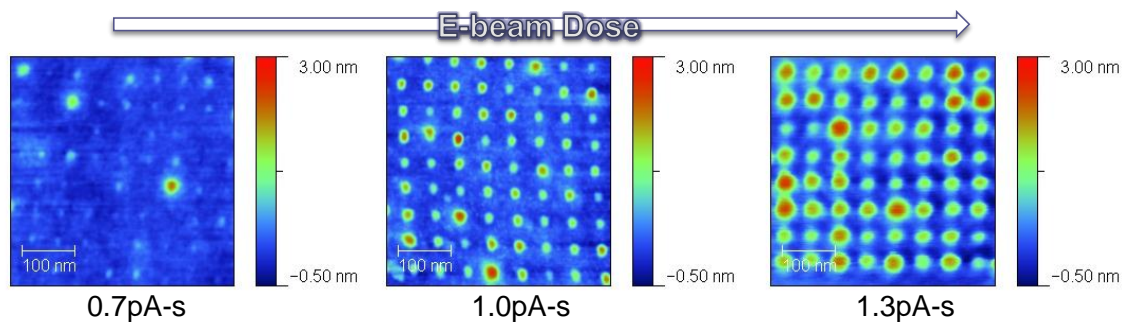
Figure 5-5: AFM images in the optimized dose range of 0.7-1.3pA-s. The typical electron beam current is 21nA for an accelerating voltage of 20 keV.

5.3.2   In vacuo annealing

Figure 5-6 shows AFM images of a small portion of the Ge/SiC arrays after Ge growth at 600°C, and after Ge growth at 400°C followed by a 700°C UHV anneal. From the AFM images, we obtain the distribution of feature volumes (where "feature" = either bare SiC nanodots or Ge/SiC composite structures) through flooding analysis. Figure 5-7 shows the average volume of the SiC arrays with 35, 50, and 100 nm spacings. In Figure 5-8, the same island distributions are plotted on an absolute scale (a), log-scale (b), and a mean normalized scale (c). The log-scale and mean-normalized distributions are useful for comparing distribution widths between specimen with mean volumes that vary over an order of magnitude. For comparison, we also include the island distributions for the specimen used for vertical transport measurements (solid black line), and the projected distribution of a fully optimized array (dashed-black line). The gray vertical lines denote the volume of a typical 10 nm SiC island.

The data points with "zero" annealing time represent the C_xH_y nanodot mean volume prior to any heating in UHV. The other three samples had an identical *in vacuo* thermal budget, except for the dwell times at 500°C prior to oxide desorption. The arrays with dwell times of 3.0 and 5.0 hours were overgrown with 1.3 ML of Ge at 600°C which was selectively etched off as indicated. The dwell time of 6.25 hours had no Ge grown on the SiC template. Figure 5-7 and Figure 5-8(a) clearly show that the overall heating and conversion to SiC results in up to 86% reduction in feature volume from the original C_xH_y nanodots. While some of this reduction is likely associated with the high temperature conversion to SiC, there is a strong dependence on the 500°C dwell time.

For example, from Figure 5-7, the mean SiC nanodot volume after 6.25 hours dwell is reduced by 65% compared with the 3.0 hour dwell. Hence significant mass was lost during the dwell. Furthermore, as shown in Figure 5-8(b), the width of the log-distribution of volumes increases with the dwell time at 500°C, negatively impacting array uniformity.
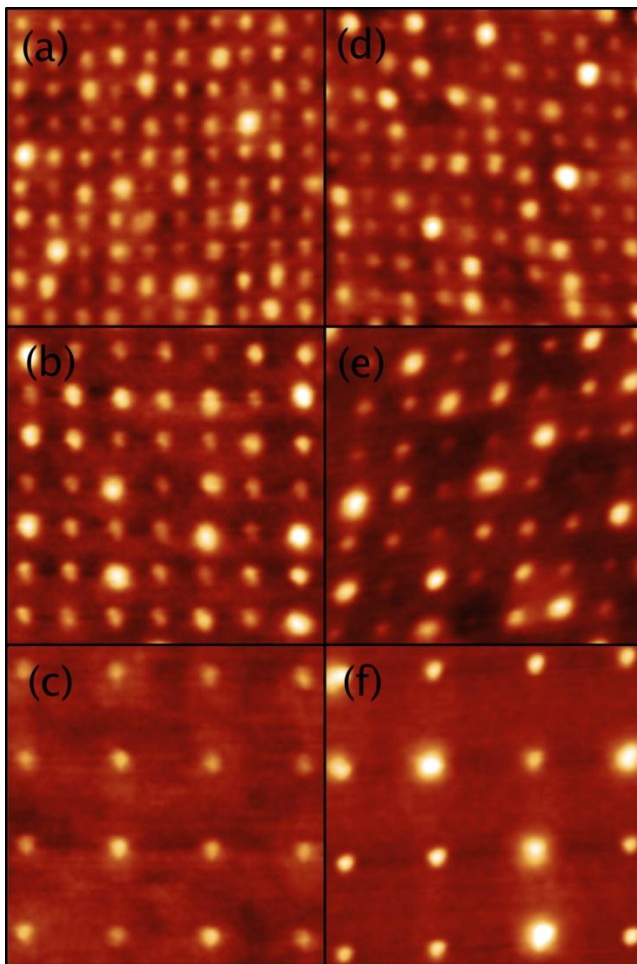
Figure 5-6: 35 nm, 50 nm, and 100 nm feature arrays after (a-c) 600°C and (d-f) 400°C + 700°C Ge depositions. Each tile is a 350 nm x 350 nm section from larger arrays. (Note: Small deviations in orthogonality are due to drift during AFM scanning.)
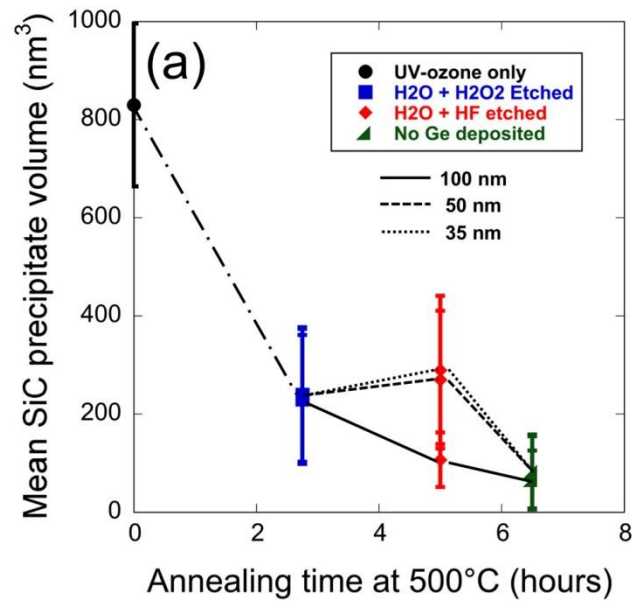
Figure 5-7: (a) Average SiC nanodot volume vs. dwell times at 500°C. In all cases, Ge has either been deposited and then selectively removed, or not deposited at all. 35 nm, 50 nm, and 100 nm template spacings are delineated by connecting lines. (b) Corresponding distributions of nanodot volumes for the 100 nm pattern spacing for each 500°C dwell time.
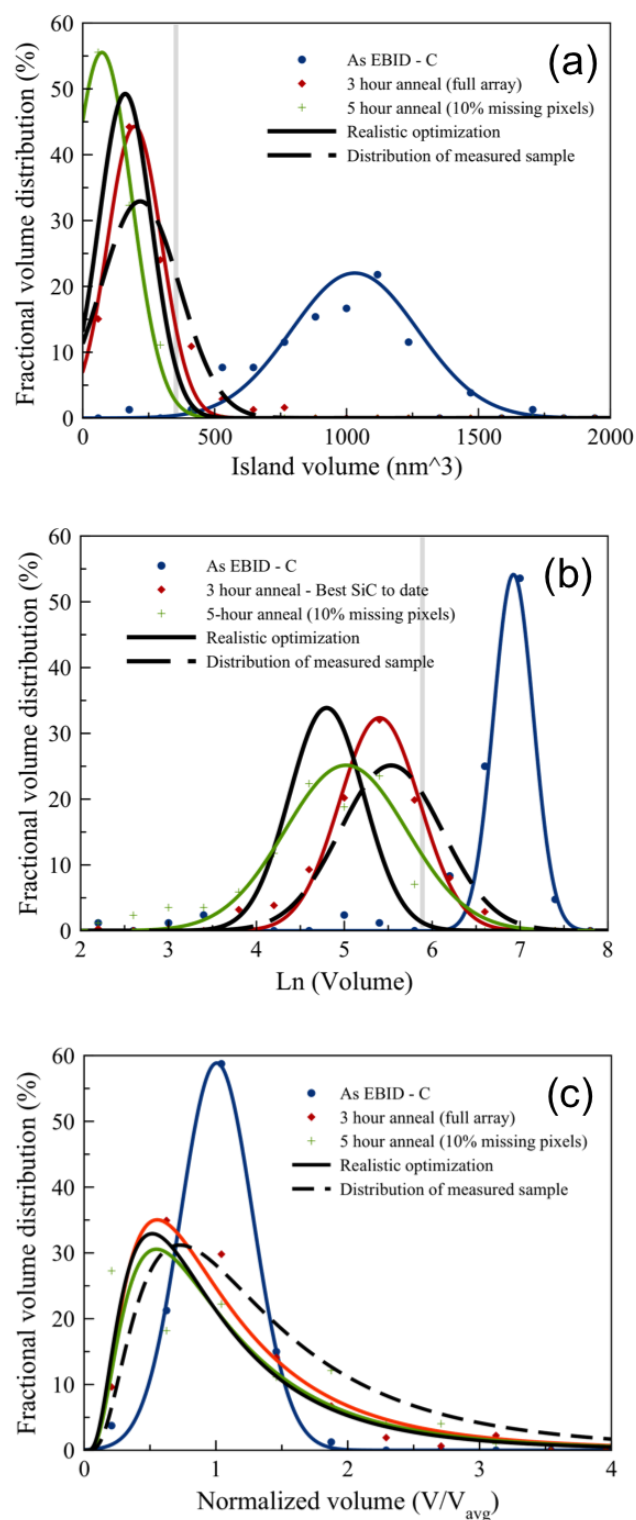
Figure 5-8: (a) Island volume distribution during dehydrogenation at 500ºC in UHV for the indicated annealing times. (b) The same volume distributions plotted on a log scale to highlight coarsening processes in the small volume range. (c) An average volume normalized plot of the same distributions exhibiting a log-normal shape. Dashed black curve represents the distribution of the electrically measured specimen prior to full process development. Solid black curve represents a realistic estimate for an optimized island distribution. The vertical gray lines denotes the volume of a 10 nm SiC nanotemplate.

During heating of the EBID-written C_xH_y patterned features in UHV, a 500°C dwell is found to strongly affect the final feature size, with longer dwells leading to reduced feature size and a much broader size distribution. Possible mechanisms for these changes include evaporative loss, diffusive loss into the substrate, and interparticle coarsening. We eliminate carbon diffusion into Si as a loss mechanism, since it is known to be insignificant below 600°C. [108,109] Interdot coarsening by itself cannot lead to loss of mass. Hence we speculate that at 500°C, volatile components of the C_xH_y nanodots evaporate, leaving behind a carbon-enriched feature; others have similarly reported complete dehydrogenation of C_xH_y between 450-550°C [6]. The concomitant broadening of the size distribution either implies the evaporative loss process is locally non-uniform, or that coarsening is occurring simultaneously with evaporation, likely mediated by a non-volatile surface diffusing species, e.g., carbon atoms.

Taking this one step further, we can combine the mean island volume as a function of 500°C annealing time with qualitative observations of array quality to generate a process diagram for the carbonaceous templates. In Figure 5-9, we show that for annealing times greater than 4 hours, pattern fidelity is lost and for short annealing times, large residual carbon dots may be unstable to high temperature annealing (as discussed in Section 5.6). Thus, the optimum 500°C annealing time is approximately 2.5 – 3.0 hours.
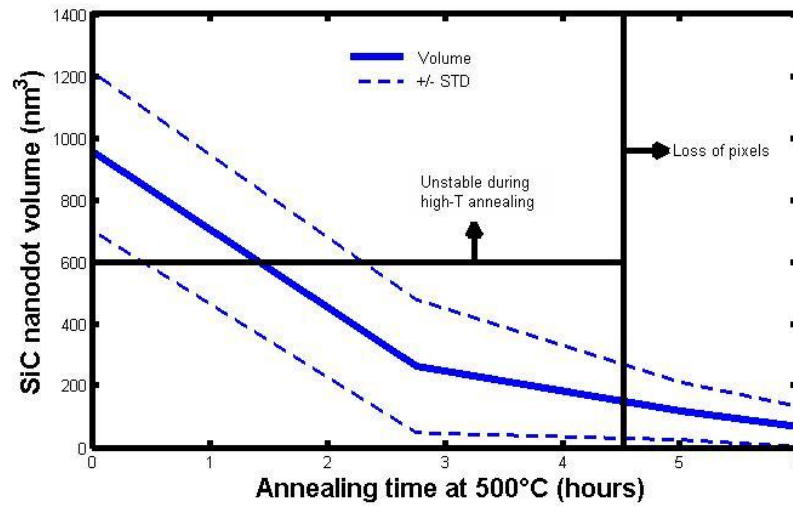
Figure 5-9: SiC annealing process diagram.

5.3.2   SiC formation

During heating to 780°C to desorb silicon oxide, HRTEM indicates that the

nanodots convert to crystalline, epitaxial 3C-SiC [56] (Figure 5-10 and Figure 5-11,

below). Guise, et al., found that a macro-area EBID (300 μm diameter region vs. our 20

nm diameter features) began converting to SiC above about 600°C, and were fully

converted to SiC at about 900°C. [6] Although our maximum temperature is lower, the

amount of deposited carbon per area in our experiments is also much lower than in Guise,

et al., so much less interdiffusion is required to complete the carbidization. Furthermore,

the TEM shows that the carbides do not penetrate into the Si substrate, suggesting that Si

surface diffusion from the adjacent regions helped supply the formation of the precipitate.

A full structural analysis of the carbides is discussed below.

5.4   Structure of the SiC templates

To obtain deeper insight into potential mechanisms behind Ge-on-SiC self-assembly, we add to the surface analysis study of Guise, et al., by cross-sectioning select specimens for high-resolution transmission electron microscopy (HR-TEM). As a result, we extract critical information on the phase of the SiC nanodots, their epitaxial orientation, and whether Ge actually nucleates preferentially on SiC. The study reported here was part of a larger effort geared towards examining magnetotransport in coupled Ge dot arrays. Preliminary results, reported in Chapter 6, give strong evidence that the nanostructures do confine electrons at low temperatures. Hence, it is essential to characterize the detailed structure of the quantum dot arrays.

Unlike the experiments reported by Guise et al [103], the Ge/SiC features were encapsulated with 50 nm Si grown at 250-300°C. The low capping temperature was chosen to ensure conformal Si growth whilst maintaining single crystalline epitaxy [104].

High resolution, cross-section TEM (HRTEM) micrographs of two Si-capped, Ge/SiC/Si (001) nanodots are shown in Figure 5-10. These nanodots have basal diameters of 7 nm and 15 nm, respectively, and heights of 1.5 – 2 nm. Due to their small size, the SiC nanodots are completely surrounded by Si in the cross-section, and hence the lattice fringing is dominated by Si. However, analysis of both the real-space Moiré fringing, and the FFTs of the micrographs indicates that the carbide polymorph is cubic 3C-SiC, epitaxially formed on Si in a "cube-on-cube" orientation. The SiC (111) interplanar spacing is measured to be 2.53 Å from the FFT in Figure 5-11(a), representing +0.40% strain. Since the lattice mismatch between 3C-SiC and Si is 20%, the carbide nanodots are highly relaxed towards their bulk lattice constant. The FFT also indicates there is a $2^{°}$

tilt (about the <110> zone axis) misalignment between the SiC nanodot and the Si substrate. Close examination of the micrographs suggests the presence of {111} facets on the perimeter of the SiC, while a {001} top facet is presumed, but not directly imaged. Note that the Si cap grown over the SiC nanodots is also fully epitaxial; however, additional defect-related contrast in the Si cap is observed. A full structural characterization of the Si cap is discussed in Section 5.8.
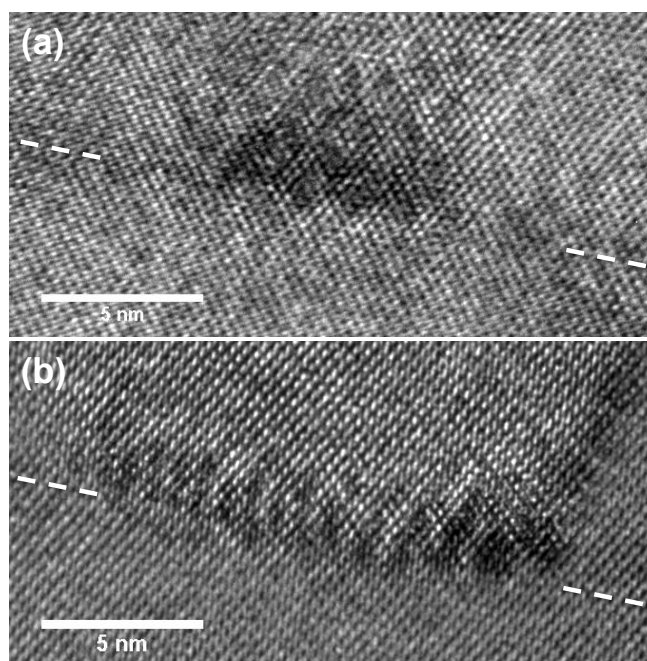
Figure 5-10: (a) and (b) Cross-sectional TEM of two carbide nanodots, along a <110> zone axis. The original Si substrate surface is delineated with dashed lines.

TEM also shows that the carbides do not penetrate into the Si substrate, suggesting that Si surface diffusion from the adjacent regions helped supply the formation of the precipitate. The SiC nanodots are close to fully strain-relaxed, and hence have a semicoherent interface with the Si substrate exhibiting misfit dislocations at

a periodicity equivalent to that of the Moire fringe spacing, 1.6nm. The epitaxial Si

overgrown above the SiC nanodots should also have a semicoherent interface. Due to the

complex contrast in the vicinity of the misfitting SiC nanodots, it is difficult to directly

image the dislocation structure. Figure 5-11(a) is the FFT pattern taken from Figure

5-10(b). In addition to showing that the SiC is highly relaxed, a slight misalignment of

the spots also shows that the SiC nanodot has a 2° tilt misorientation relative about the

[110] Si zone axis (see Figure 5-11(d)). Using Bragg filtering (inverse FFT) of Moire

fringe superlattice spots, we isolate the embedded SiC in Figure 5-11(b). An abrupt shift

in the fringe registry is observed (arrowed), which may result from a stacking fault,

which are known to have very low energy in SiC. In addition, by selecting higher

frequency Si(111) and SiC(111) reflections, we can directly image the edge components

of interfacial misfit dislocations that are parallel to the [110] zone axis, as shown in

Figure 5-11(c).
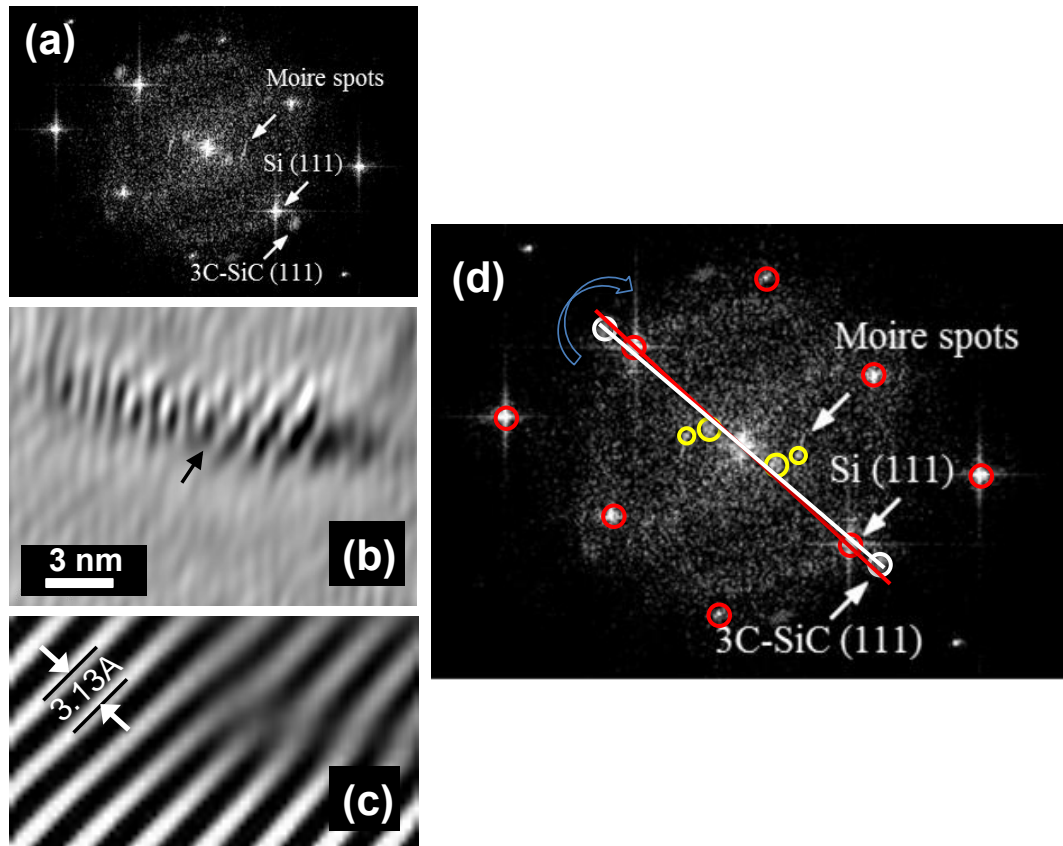
Figure 5-11: (a) the corresponding FFT from the dot Figure 5-10(b), extra spots beyond the Si(111) represent 3C-SiC and inner spots come from the Moire fringes. (b) Bragg filtered (inverse FFT) image using Moire fringe reflections. Contrast highlights buried SiC. (c) Bragg filtered image using Si(111) and SiC(111) reflections. The edge component of an interfacial misfit dislocation as observed at the SiC/Si interface. (d) Labeled FFT spots showing approximately 2° rotation of the 3C-SiC(111) spots relative to the Si(111). This suggests there exists cube-on-cube epitaxy with a 2° misorientation with a <110> ZA.

In cubic systems with low misfit, such as Ge_xSi_{1-x}/Si (001), heteroepitaxial growth initially results in a coherently-strained layer, followed by the introduction of misfit dislocations after the critical thickness is surpassed [110,111]. These dislocations are typically 60° a/2<101> type that glide on inclined {111} planes. However, for SiC/Si with 20% misfit, even the first monolayer will not be able to remain in coherent registry,

and dislocations will be "grown into" the film via local atomic relaxations at the heterointerface. Ideally this would result in formation of sessile 90º, a/2[101] and a/2[1-10] dislocations, where the burgers vector lies entirely in the inteface plane, relieving more strain than 60º dislocations. Many studies have shown that epitaxial 3C-SiC on, or in, Si relaxes completely [112–114], and several have observed 90º dislocations in the 3C-SiC/Si (001) interface. [115–118]

In an investigation of 3C-SiC formation during evaporative deposition of pure C onto Si (001), a nanoscale island growth mode was observed by Zekentes, et al., at temperatures close to those used here [119]. Islands exhibited {111} facets, and growth on these planes was held responsible for the presence of stacking faults and microtwins in the resulting films. Our observation of a stacking fault in a larger SiC nanodot, together with the observed {111} side facets, is consistent with this view. Zekentes, et al., also observed small tilt and twist misorientations in some of their islands, similar to what is observed here.

Although 90º dislocations are expected on energetic grounds, our observation of in-plane tilt and possible out-of-plane twist misorientation in these SiC nanodots could be explained by the presence of an array of preferred 60°-type interfacial misfit dislocations encircling the carbides. As Figure 5-12 shows, a 60º misfit has a screw component (b_S, green), misfit component (b_M, red) that relieves lattice misfit, and a tilt component (b_T, blue). If all the interfacial dislocations were 60º, the spacing required to relieve the 20% misfit strain would be $D_{mis} = b_M/0.2 = 0.96$ nm. The observed 2º tilt could be accounted for by 60º misfits with identical b_T, spaced by $D_T = b_T/\tan(2º) = 7.8$ nm along the heterointerface, which is in reasonable agreement with Figure 5-11(b). Hence only a

small number of interfacial dislocations (relative to those required to relieve the misfit strain) containing a net tilt component could provide the observed rotation. Similarly, any twist misorientation about the [001] axis could be accounted for by the screw component, where $D_S = b_S/\tan(q)$, where q is the twist.
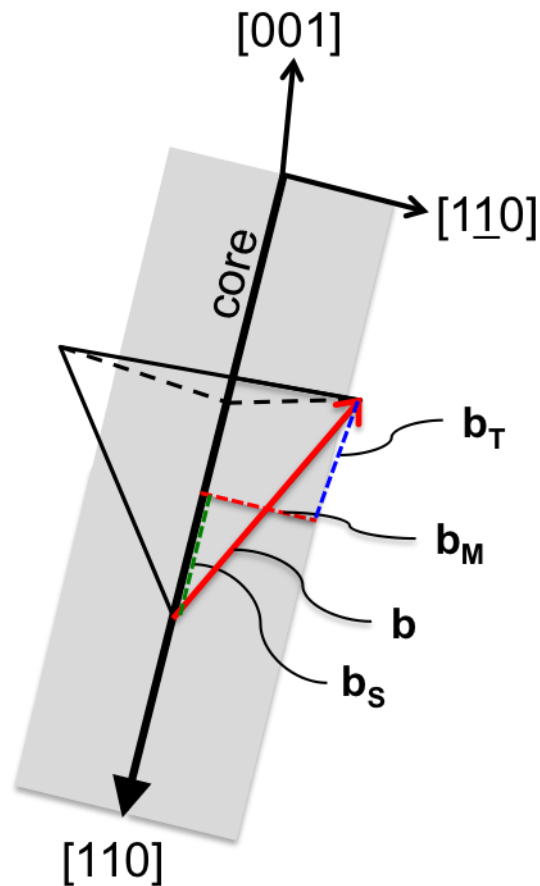
Figure 5-12: This figure shows a 60° misfit dislocation in the (001) plane, having one of the four possible strain-relieving burger's vectors (**b**, in red). The tetrahedron of {111} planes is also shown. b is resolved into three orthogonal components, a screw (b_S), misfit (b_M) and tilt component (b_T, which is parallel to [001]).

5.5   Ge overgrowth at 600°C

In Figure 5-13(a), we show a 35 nm array after Ge deposition at 600°C along with a

fast Fourier transform (FFT) of the full array. By extracting the FWHM of the first order

<01> peak, we determine the average spatial variation to be ±1.6nm. While positional

accuracy of these QDs is adequate for device needs, it is more difficult to control the

diameter of the SiC template. Figure 5-13(b) is a cumulative probability plot of QD

diameters for the same 35 nm array. In the observed distribution 51% of islands have

FWHM ≤10 nm and 95% are ≤15 nm.
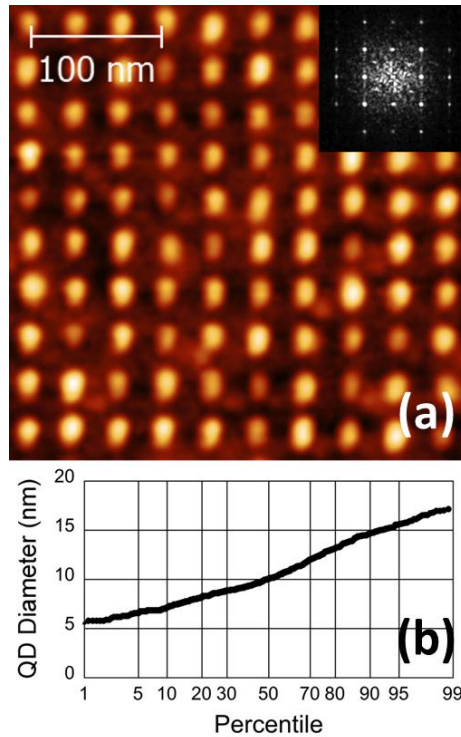
Figure 5-13: (a) AFM image of a 10x10 array section of composite Ge/SiC QDs with 35 nm spacing. The inset displays a FFT of the full array; the FWHM of the <10> peak determines a positional error of ±1.6nm. (b) Cumulative probability plot of the QD diameters for the same 35 nm spacing array. 51% of islands have Ø ≤10 nm, while 95% have Ø ≤15 nm.

Using high-angle annular dark field (HAADF) imaging of an embedded SiC nanodot, Figure 5-14 directly shows the spatial distribution of the Ge film by Z-contrast. In this film, the Ge layer was grown thicker (still at 600ºC), to 3 ML, in order to provide stronger imaging contrast, and a Si capping layer was used to protect the surface during FIB lift-out. In Figure 5-14, the SiC nanodot is the dark region while the white band is the Ge layer. The HAADF image clearly shows that the Ge layer does not preferentially accumulate at the SiC site, *nor does it even appear to coexist with the Si capping layer*. Figure 5-14 also displays a high resolution STEM image of the same SiC nanodot. Notably, the Ge film is fully epitaxial and wets the Si substrate completely to the SiC/Si interface.
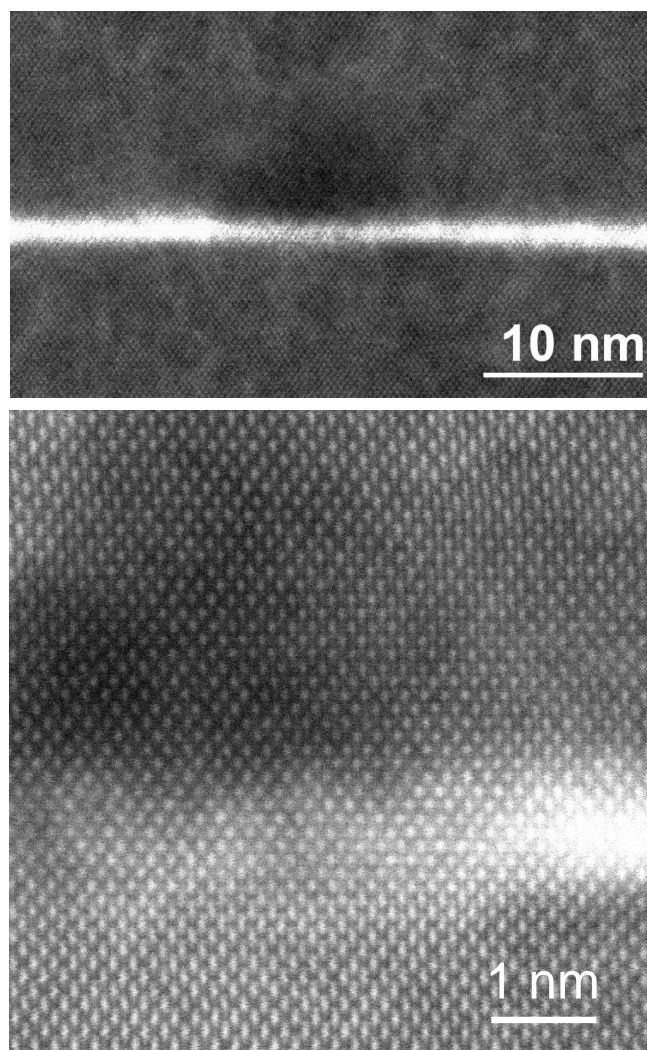
Figure 5-14: (top) HAADF-STEM image of an embedded SiC nanodot (dark region). Z-contrast clearly shows the deposited Ge film at the substrate-cap interface. No Ge has overgrown the SiC nanodot. (bottom) high-resolution HAADF-STEM showing the right-edge of the same SiC nanodot at its intersection with the Ge WL.

Clearly, our growth process, with Ge deposition at 600ºC, followed by low-temperature Si capping, results in Ge rejection from SiC template sites. Ostensibly, this occurs due to the unfavorable Ge-C bond. This manifests itself in many different experiments, including a thermodynamically-driven tendency for Ge to segregate rather than solutionize when introduced into SiC by ion implantation [120] or by MBE co-

deposition [121,122]. Similarly, in growth of metastable diamond cubic alloys of $(Si_{1-x}Ge_x)_{1-y}C_y$, where y is $<< 0.5$, the presence of Ge tends to have an additional destabilizing influence on solution formation [123–125]. On the other hand, for Ge deposition on the (0001) plane of 4H-SiC substrates, Ait-Mansour, et al., found that Ge underwent Stranski-Krastanov island growth when the basal plane is Si-terminated [126], demonstrating that Ge wetting is possible under certain conditions. In our system, given the large Si reservoir surrounding the 3C-SiC nanodots, we assume that the SiC islands are in fact likely to be Si-terminated. However, unlike the Ait-Mansour work, where a monolithic SiC substrate is used, the small areal coverage of SiC in our system, with sub-15 nm carbide dots surrounded by Si (001), leads us to speculate that Ge strongly prefers to attach to the lower-energy surface bonding sites on the nearby Si substrate.

The possibility should be mentioned that limited Ge sticking to the SiC nanodots may occur during deposition, and subsequent Si capping could lead to complete Ge rejection and replacement with Si. High temperature capping is known to modify QD shapes extensively, whereas capping at lower temperatures minimizes such effects [127,128]. Given the low capping temperatures used here, it seems unlikely that Si deposition could remove an entire Ge QD from the SiC, although it might affect Ge at the monolayer level. It would be useful to examine lower growth Ge temperatures, where restricted adatom mobility could at least produce conformal coverage of the SiC nanodots. Additionally, we suggest there is another way that Ge could be forced to accumulate preferentially on SiC: if the Si regions between SiC sites have significant residual surface-C impurities present, Ge atoms may actually find these regions less energetically favorable than the Si-terminated 3C-SiC (001). It is already known that C

impurities on Si (001) drastically reduce Ge diffusion. [123,129] Such a mechanism might have been operative in the work of Guise, et al.

5.6   Ge overgrowth at 400°C and post-annealing

The effect of post-deposition annealing on the size uniformity is shown in Fig. 4. Each volume distribution is obtained from more than 200 features per array. For comparison, the size distributions after selective removal of the Ge are also shown, where pre- and post-etching distributions are measured from the exact same features. Growth of 1.3 ML of Ge at 600°C results in a volume distribution that is nearly identical to that of the underlying SiC template (obtained by selective etching). This observation holds for all three interdot spacings. On the other hand, growth of Ge at 400°C, followed by a 700°C, 30 min anneal, clearly leads to coarsening. The total volume of the distribution is larger than the distribution for conformal Ge on the SiC template, implying that additional mass was accumulated, i.e., perhaps due to uptake of Si from the substrate. The additional mass would correspond to consumption of about 1 ML of Si from the entire patterned region, distributed on the patterned sites. Furthermore, the degree of coarsening *increases* with the interdot spacing, consistent with a larger local supply of Si surface atoms. At 100 nm, a clearly bimodal distribution is produced. The bimodality is less pronounced at 50 nm spacing, and only a shoulder is observed at 35 nm.
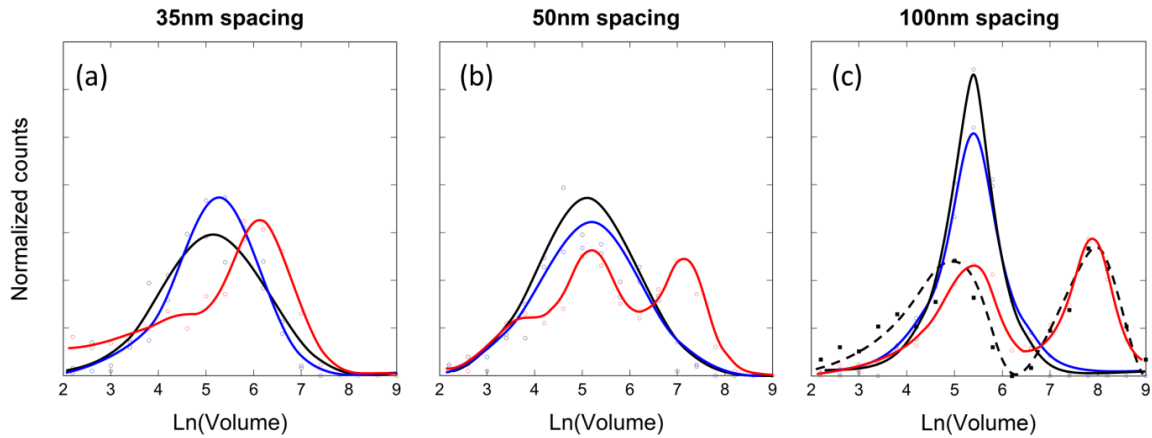
Figure 5-15: Volume distributions of Ge/SiC composite islands (2.75 hr dwell at 500°C) for two different growth strategies: (blue) Ge deposited at 600°C and (red) Ge deposited at 400°C then annealed at 700°C. (a) 35 nm spacing, (b) 50 nm spacing, and (c) 100 nm spacing. For comparison, the bare SiC arrays after selective Ge etching are also shown (black). In the case of 100 nm spacing, the annealed specimen was also etched (dashed-black).

To further investigate the degree of coarsening, we also plot the volume of each island relative to the average volume of its nearest neighbors in Fig. 5(a). In general we observe a negative trend such that larger islands tend to have smaller neighbors, consistent with a coarsening mechanism. For comparison with typical SiC nanodots (black line), line profiles of select coarsened features from a 100 nm array are shown in Fig. 5(b). The enlarged island radius is triple that of the initial carbide and the volume increase is nearly 30x. XTEM indicates that typical SiC nanodots have {111} facets at their perimeters, thus tip convolution effects are clearly present when measuring the smallest islands, but the observed profile should be accurate for enlarged islands.
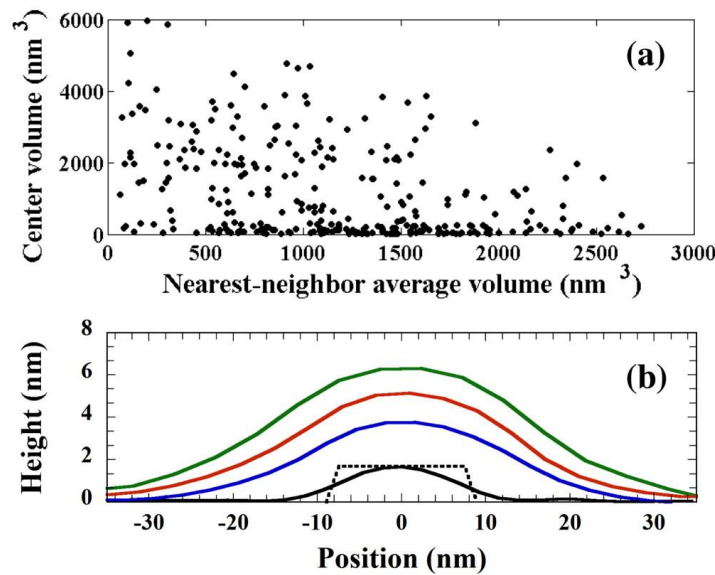
Figure 5-16: (a) A scatter plot showing the average nearest-neighbor volume surrounding each island, and (b) line profiles of a typical SiC nanodot (black line) and coarsened $Si_{1-x}Ge_x$/SiC composite islands (blue, red, green lines) from 100 nm spacing arrays, e.g. Figure 5-6(f). The dotted line-trace shows the actual SiC size/shape as observed in TEM (see Figure 5-10).

Coarsening of these post-annealed arrays is indicated by the observation that the largest islands have smaller neighbors on average. However, a net accumulation of total mass is determined by integrating the distributions before and after Ge growth+annealing, implying an additional uptake of material, most likely Si from the surrounding substrate. Since negligible volume change is observed after selective Ge etching and Ge has no known propensity for alloying with C [125], we infer that the resulting island volume consists of a dilute $Si_{1-x}Ge_x$ (x<0.6) alloy covering of the SiC nanodot. Thus, rapid island growth is likely driven by both surface energy reduction via Si overgrowth of the SiC combined with strain-reduction at the dislocated $Si_{1-x}Ge_x$/SiC interface akin to the accelerated evolution of so-called "super domes" [106,130–133]. Regardless, while we

observe the formation of *morphological* Ge QDs, their bimodal distribution and extended defect nature is non-ideal.

5.7   Analytical model for Ge/SiC heterostructures

We can also approach the problem of Ge overgrowth of SiC analytically. By treating the formation of a self-assembled Ge QD as a simple nucleation and growth problem, one can write an equation for the change in free energy as a function of critical nucleus size. The primary driving force to form a self-assembled Ge island on SiC will be the reduction in elastic strain energy.

Consider the simplest case, wherein a thin film of Ge is fully covering the Si substrate, but initially avoiding a small SiC region, due to large misfit strain. An island nucleus will form when some volume of Ge is transferred, fully strain relaxed to the SiC region; e.g. the Ge/SiC interface is incoherent.
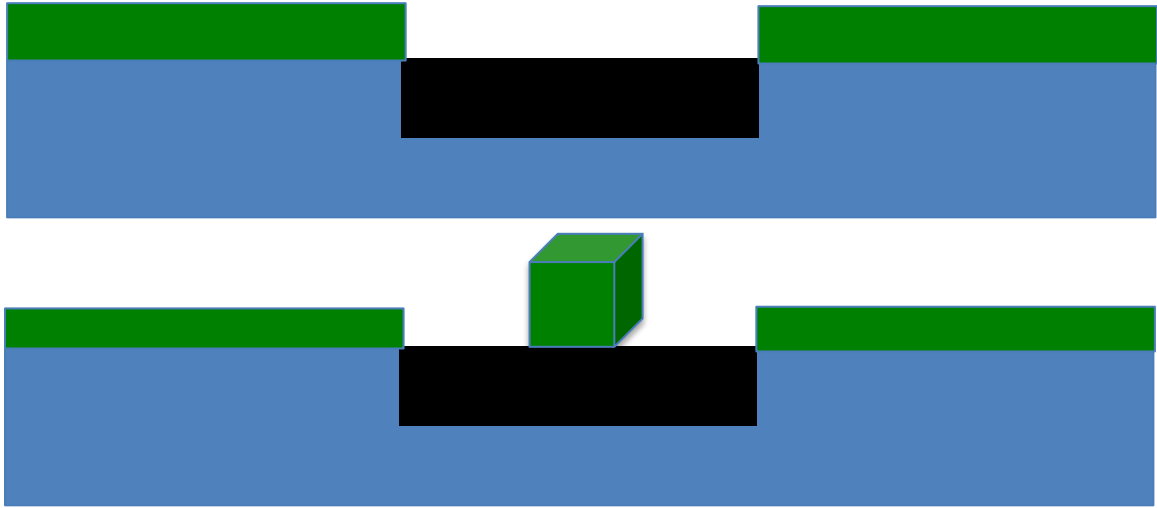
Figure 5-17: (top) Simple numerical model setup for a Ge film that is avoiding a small SiC region and (bottom) the formation of a cubic Ge island on the SiC area may be formed by transferring some of the strained Ge to an unstrained island state.

We can thus solve for the critical nucleus size by balancing the reduction in strain energy with the increase in total surface (and interface) area, as shown in Equation 5-1, and illustrated by Figure 5-17. The surface energies for Ge(001) and Si-terminated SiC(001) are 1.1 J/m^2 and 3.4 J/m^2, respectively. M is the biaxial modulus of Ge (175 GPa), and ε is the 4% lattice mismatch between Si and Ge.

$$D_c = \frac{2(5\gamma_{Ge} + \gamma_{Ge/SiC} - \gamma_{SiC})}{3M\varepsilon^2}$$

Equation 5-1

The interfacial energy between Ge and SiC is unknown, but we set a lower bound at zero, assuming a "perfect interface" and an upperbound is the sum of the Ge(001) and

SiC(001) surface energies, e.g. the two surfaces are non-interacting. The actual interface energy is likely closer to the upper bound due to the incompatibility between Ge and C.

Solving Equation 5-1, we determine the lower and upper bounds for the critical nucleus sizes as 5.3nm and 16.0 nm, respectively. The corresponding cubic critical nucleus volumes are 149nm^3 and 4096nm^3. We compare this to our measured island volumes of ~100 nm^3, which is less than even the unrealistic lower bound. Even by changing the geometry of this simplistic model, it does not seem likely to justify preferential Ge accumulation on SiC.

5.8 Si encapsulation

For TEM and electrical measurements, it is critical to encapsulate the patterned features with Si. In this study, we use three different capping strategies: (1) all low temperature (300°C), (2) elevated temperature (400°C), and (3) two-step capping, 5 nm at 250°C followed by 45 nm at 500°C. Typically, low capping temperatures are chosen to ensure conformal Si growth [104], however this may be at the expense of crystalline quality.

We have performed cross sectional TEM on patterned arrays with 50 nm spacing. These samples have a 1.5 ML Ge film grown at 600ºC. The carbides are visible exactly at the substrate surface and then a 50 nm Si encapsulation layer is grown.

5.8.1 300°C encapsulation

During low temperature Si encapsulation we observe 'V'-shaped regions above each SiC template site. Figure 5-18(a-b) shows a bright field (BF) and dark field (DF)

comparison with a selected g-vector of (002), perpendicular to the film. Here, the active

mechanism of contrast is predominantly strain. This contrast may arise from either

defect-induced elastic deformation inside the 'V' and/or by some misorientation of the

'V' relative to the perfect epitaxial overgrowth between defected areas.
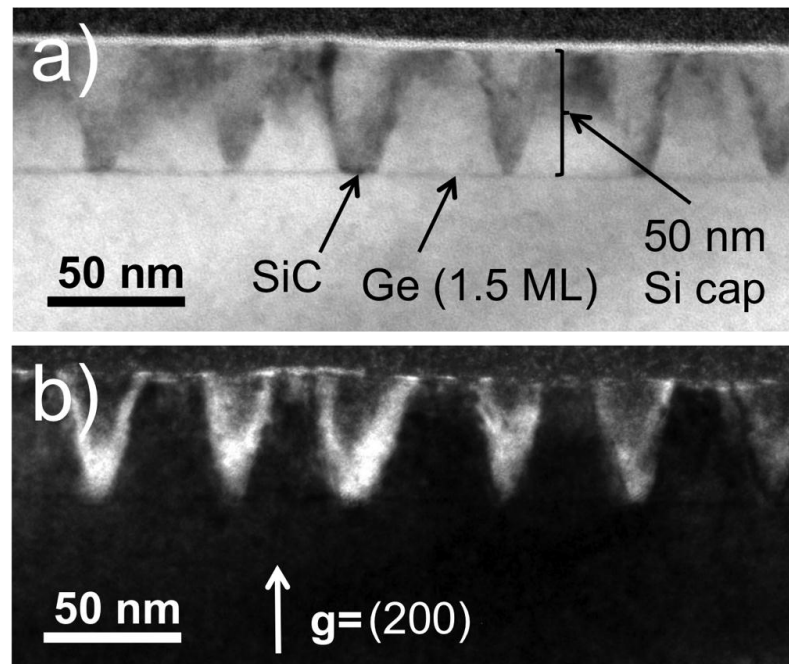
Figure 5-18: (a) Low magnification bright field image of defect cones during Si overgrowth of SiC nanodots. (b) WBDF image of the same area with g=(200).

In Figure 5-19(a-b), we use HRTEM to investigate the detailed contrast

mechanism at the boundary of the defective-'V'. The low temperature Si overgrowth is

fully epitaxial, although the 'V' boundaries may be defined by narrow stacking faults as

discussed in Section 5.8.1.1. By plane-tracing, using Figure 5-19(b), we find that the

(002) atomic planes are continuous across the dark boundary, whereas (111) planes are

not. One can achieve a similar analysis through Bragg filtering (inverse-FFT) around the

(111) and (002) spots, as shown in Figure 5-20. When selecting (002) vectors, iFFT

contrast is even indicating that all (002) planes are in-phase. However, using (111)

vectors, dark contrast along the 'V' boundary indicates a ½ plane registry error along the

(111).

The observation of disregistry along only a single set of atomic planes, suggests

uniaxial rotation, with an axis perpendicular to the continuous plane set, i.e. (002). To

confirm rotation, we employ fine probe convergent beam electron diffraction (CBED).

This diffraction technique produces disks at each allowed reflection which contain

additional information on local crystal symmetry. In addition, due to the reduced intensity

of each diffraction 'disk', small deviations from zone axis (ZA) are detectible and

Kikuchi band intensity is enhanced.

Figure 5-19(c-d) are CBED patterns from an area inside the defective-'V' and

from the unperturbed material outside the 'V' (labeled s2 and s1 in Figure 5-19(a)).

Using simulated Kikuchi bands (also shown in Figure 5-19), the CBED pattern under

small rotations is calculated and compared to experimental results allowing determination

of the exact ZA. From the observed CBED data, we calculate that the material inside the

'V' has a rotation of 1.81°, with a [001] axis[††]. Similar small angle rotational

misalignment has been observed during diamond growth on Ni substrates [135].

[††] Simulation and calculation of the exact zone axes was performed using the Java
Electron Microscopy Software (JEMS) software package. The angle between zone axes
was determined using Matlab code developed by Priya Ghatwai [134].
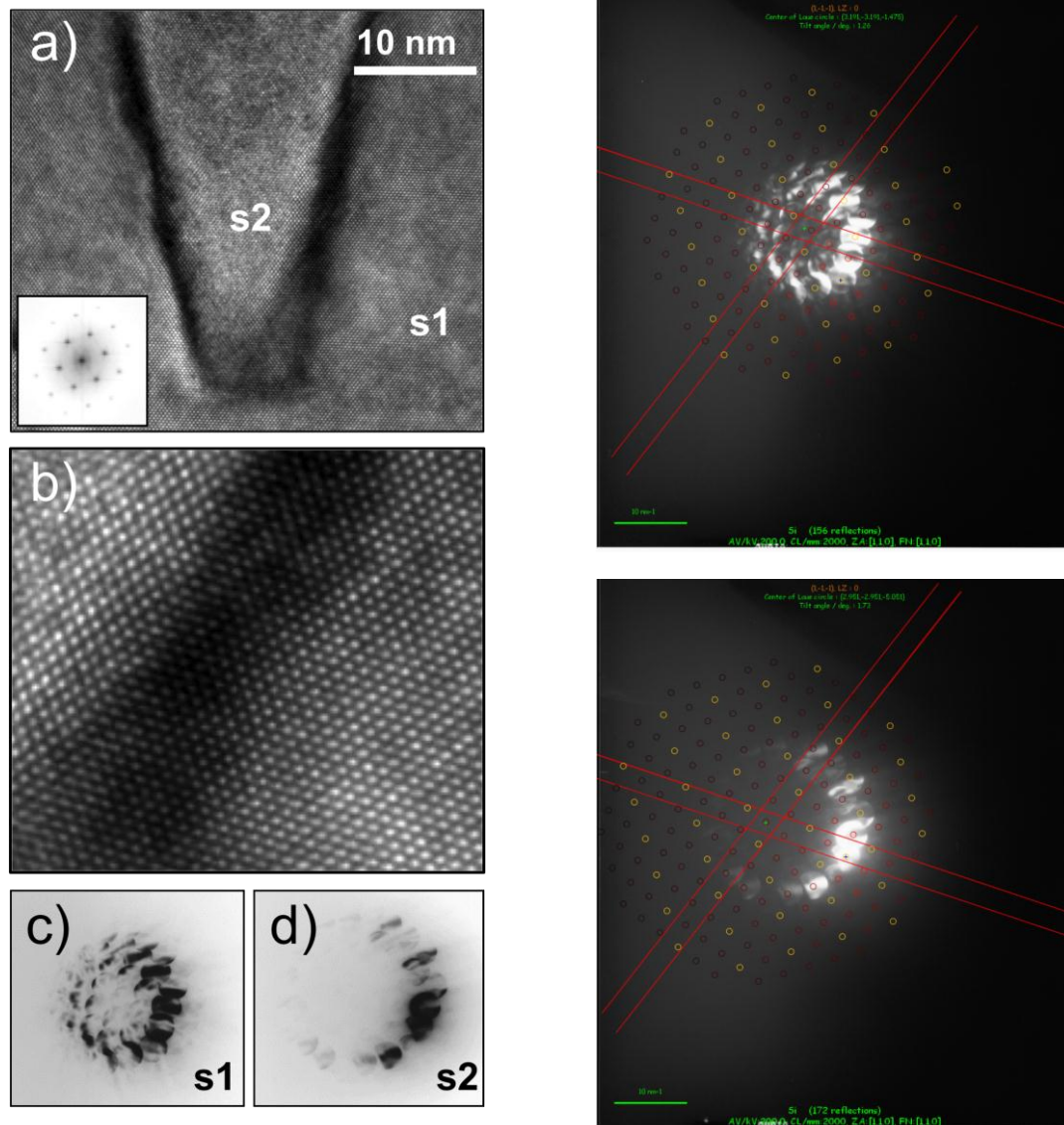
Figure 5-19: (a) HR-TEM image of a Si defect cone, the inset is a corresponding FFT. (b) zoom-in of the cone boundary in (a), by drawing lines along atomic columns, one can determine a ½ plane disregistry along the {111}, while the {200} are in perfect registry across the boundary. (c)-(d) CBED patterns of spots labeled **s1** and **s2** in (a). These are used to measure the precise zone axis in each region and calculate the magnitude and direction of rotation. In the right column, simulated (1-1-1) and (-111) Kikuchi bands are overlaid on the s1 and s2 CBED patterns (top and bottom, respectively).
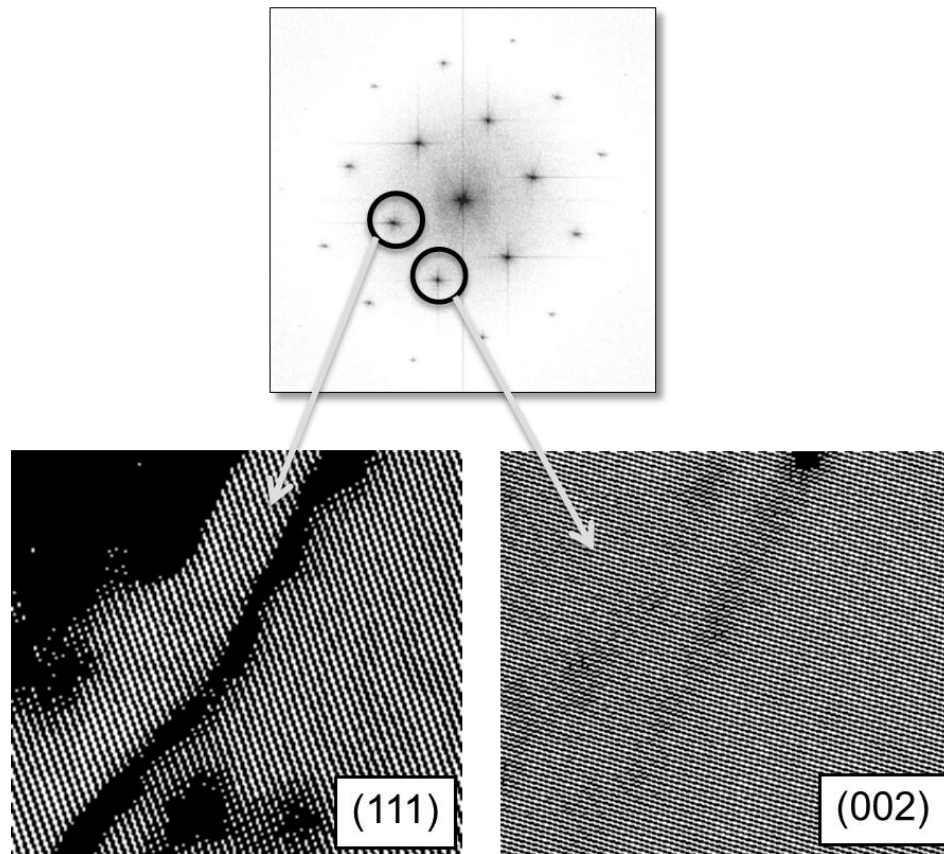
Figure 5-20: Inverse FFT filtering of the HRTEM image shown in Figure 5-19(b). (left) iFFT from the (111) reflection and (right) iFFT from the (002) reflection.

In Section 5.4, the possibility of a twist rotation in the SiC was discussed and may be accounted for by the screw component of a 60º misfit dislocation. These dislocations are expected to completely encircle the embedded carbides providing an anti-symmetric twist component at the Si film / SiC interface, resulting in perfect orientation between the Si film and the underlying Si substrate. Thus, the observed 1.8º rotation of the defective 'V' region in the Si film must be a result of additional edge dislocations that are grown into the film and extend to the free surface. Figure 5-21 illustrates the full dislocation loop for a simplified case, where the defective overgrowth is columnar with vertical boundaries. In this scenario, the pure-edge a/2[1$\underline{1}$0] Burger's vector is parallel to the

cross-section ZA, thus rendering it invisible during TEM investigation. Propagation of

the rotation through the thick Si overlayer is observed only when the growth kinetics are

severely limited, otherwise, high temperature overgrowth allows relaxation and re-

alignment with the surrounding Si/Si(001) epitaxial matrix. Based on an approximate 1.8°

rotation, we calculate the total 'V' boundary atomic strain to be approximately 3%. Thus,

the 'V' boundary contrast is a combination of elastic and shear strain caused by the

increased defect concentration inside the 'V' and the ~1.8° boundary rotation.
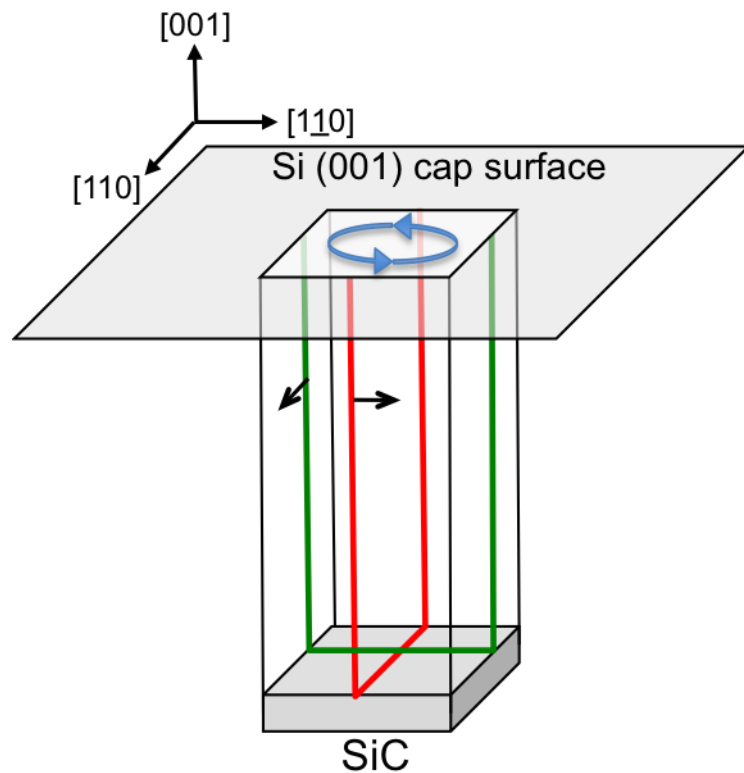
Figure 5-21: This figure shows the V-shaped region of the Si cap above a SiC nanodot, in 3D, simplified as a square-column. The twist misorientation about [001] of the columnar region relative to the surrounding cap would be produced by the pure edge dislocations shown above, where the burgers vectors are shown with black arrows. Note that in a cross-section parallel to (1$\underline{1}$0), the burgers vector of a dislocation contained in the section would be parallel to the zone axis, and therefore invisible to the TEM.

5.8.1.1   Faulted overgrowth

Additionally, it is possible that planar defects nucleate during Si overgrowth on {111} SiC side facets. We propose that the initial 2D overgrowth on the SiC side facets can have a stacking sequence that is out of phase with the (001) oriented planar growth on the adjacent Si(001) substrate and on the top surface of the carbide. In this case, the intersections of the {111} side facets with the (001) oriented growth will exhibit geometrically necessary Shockley partial dislocation loops, see Figure 5-22. These loops are self-contained and can be described by a pair of Shockley partials (b = a/6 <121> and b = a/6 <21-1>), as shown in Figure 5-23.

Full dislocations dissociate into pairs of Shockley partial dislocations. There are 3 different Shockley partials, and thus 3 permutations with of two Shockley partials. If the same pair is repeated in successive layers, the result would be a transformation from FCC (-abc-) to HCP (-abab-) stacking. The total offset of these loops would form an angle of ~63°. On the other hand, if all three permutations of Shockley partials are equally active, the net offset of the stacked partial loops will be 'zero' [136]. In this work, we observed disregistered overgrowth with an inclination of ~75º, this is consistent with the expected offset if 2 out of 3 Shockley partials are active on the growth plane. Assuming the SiC is square, and its {111} side-facets are epitaxially oriented with the substrate, there will be two edges bordering (001) planes that lend access to only two Shockley partials.

Going a step further, the bright contrast boundary in Figure 5-18(b), shows that the disregistered overgrowth narrows with film thickness. It is possible that the Shockley

partials are weakly interacting at this kinetically limited temperature (300°C) and tend

towards annihilation during growth.
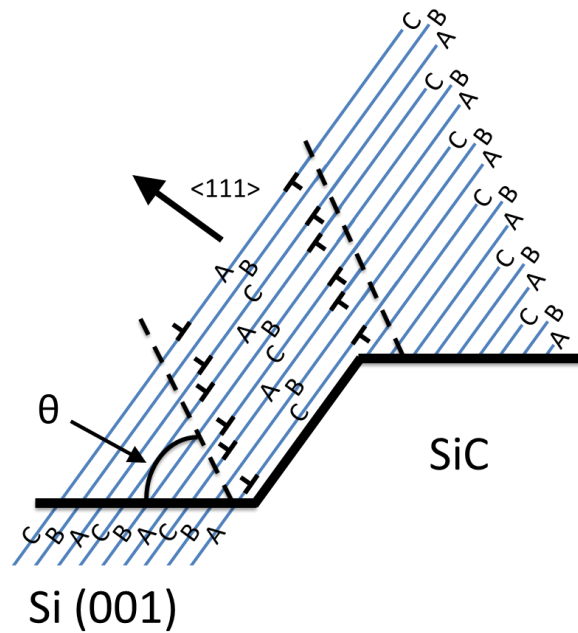
Figure 5-22: Schematic of {111} plane stacking showing that stacking errors can originate on the {111} sidewalls of SiC nanotemplates. Shockley partials exist at the intersection of differently stacked planes. The angle of the disregistered boundary depends on the distribution of Shockley partial variants.
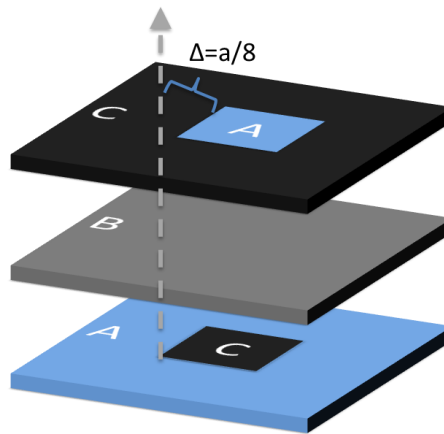
Figure 5-23: Illustration of (111) planes containing loops of material that with an offset stacking sequence. The letters A,B,C denote the stacking of each region.

5.8.2   400°C encapsulation

Ultimately, the goal of this work is to generate epitaxial heterostructures that are capable of confining proximal carriers. Dislocations and crystal defects are unfavorable for carrier recombination and polarization lifetimes, thus it is critical to obtain heterostructures with high crystalline quality. In an attempt to avoid extended propagation of the epitaxial misorientation above the SiC, a Si encapsulation layer was grown at a slightly elevated temperature of 400°C. Figure 5-24 shows an AFM image of a SiC patterned surface after 5 nm of Si overgrowth. <100> faceted pits are observed at each template site with variable diameter, which is likely related to the variation in carbide size [56]. We note here that with this slight increase in deposition temperature, the overgrowth has transitioned from a conformal coating to, at least, Si partial rejection from the template sites.

A detailed study of Ge/SiC overgrowth at 600°C also observed Ge rejection from carbide sites [56]. In that case, the Ge rejection is attributed to both chemical and lattice incompatibility. Since Si is chemically compatible, the primary driving force for Si rejection must be Si/SiC interfacial strain. That is, given sufficient kinetic energy for diffusion lengths greater than the carbide diameter, Si has a much greater sticking probability at unstrained substrate sites between carbides.
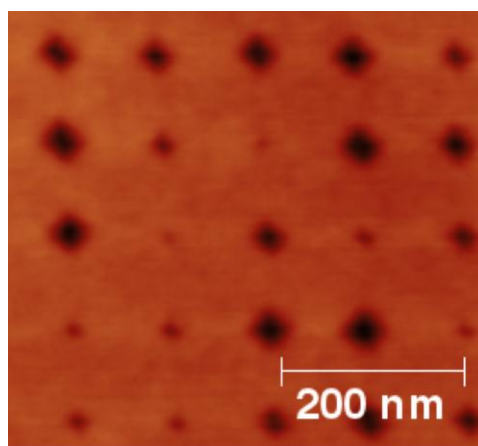
Figure 5-24: 100 nm spacing SiC nanodots encapsulated with 10 nm Si at 400°C.

Figure 5-25 and Figure 5-26 show line scans of selected pits of various width. We find that the deepest pits extend through the entire 5 nm Si overlayer and exhibit the steepest sidewall angles, 13-14º. The shallowest pits have reduced sidewall angles, as low as 5º, and in some cases we observe nearly complete surface planarization. As mentioned, the pit width is likely related to the SiC template diameter. To explain this, we speculate that the eventual coverage of the SiC template is controlled by lateral overgrowth of Si. Assuming uniform Si/SiC lateral overgrowth rates, smaller carbides will cover earlier and permit detachment of the pit bottom from the SiC template. This mechanism is illustrated

in Figure 5-27 for two carbide sizes. From a simple 1-D lateral overgrowth model, the lateral overgrowth rate (V_x), can be determined as a function of pit depth (ΔZ), Si deposition rate (R_g), and carbide radius (r_{SiC}), as shown in Equation 5-2.

$$\frac{\Delta Z}{R_g} = \frac{r_{SiC}}{V_x}$$

Equation 5-2
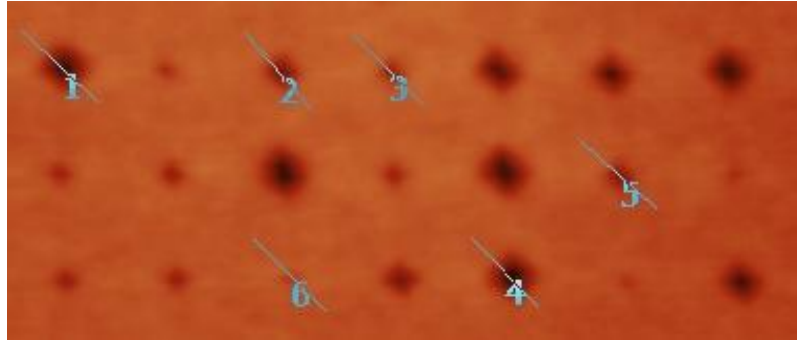
Figure 5-25: Selected pits used for linescans in Figure 5-26.
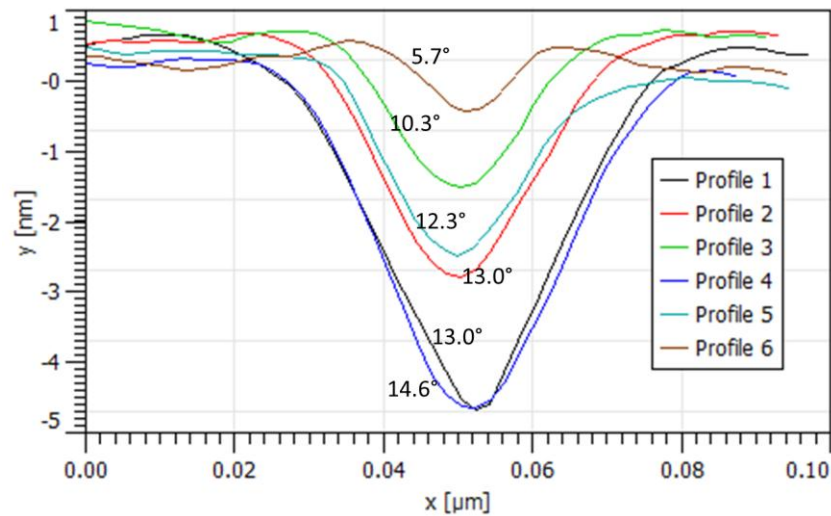
Figure 5-26: Linescans of selected pits from Figure 5-25.

Although we do not know the carbide radius from these AFM scans, it is possible to set upper and lower bounds for the lateral overgrowth rate in Equation 5-2, by correlating the largest and smallest pit depths with the largest and smallest carbides observed with TEM. The boundaries for Equation 5-2 in terms of [ΔZ, r_{SiC}] are: [50Å, 80Å] and [10Å, 25Å]. Given a Si deposition rate of 0.15 Å/s, the upper and lower bounds for lateral overgrowth, V_x, are 0.37 Å/s and 0.25 Å/s. Surprisingly, the lateral growth rate is larger than the vertical growth rate. If we additionally consider stabilization of the pit sidewalls with low angle facets, then the *effective deposition rate* around each carbide is reduced. That means that Si deposited onto the lateral-growing low angle facet is either pushed to the carbide for overgrowth, or away from the carbide to the planar inter-template growth area. It thus follows that the thermodynamic driving force to facet controls the Si lateral overgrowth of SiC.
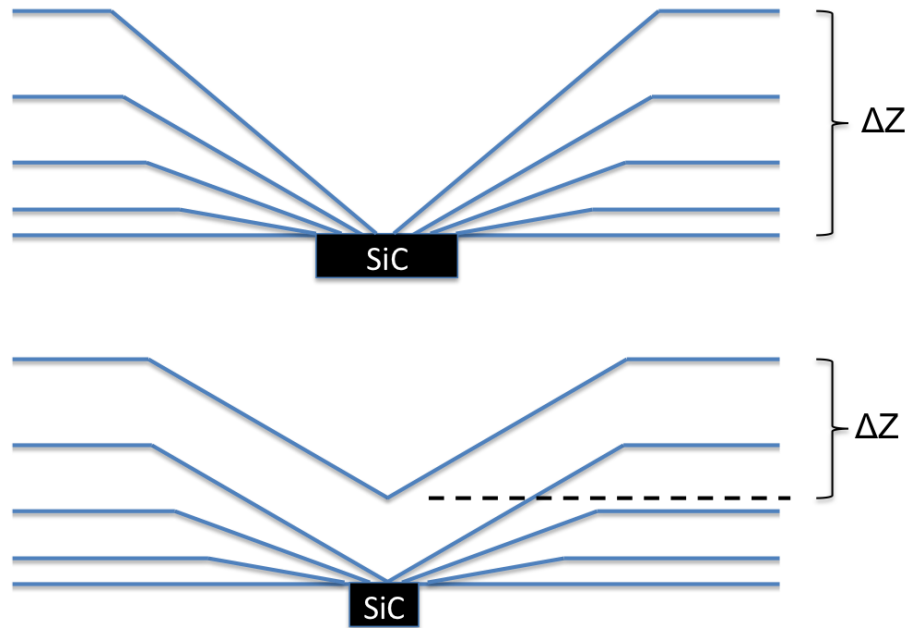
Figure 5-27: Lateral overgrowth model schematic predicting pit sizes as a function of SiC diameter. (top) Large carbides will take longer to overgrow and will result in deeper, and steeper pits. (bottom) Small carbides will overgrow quickly and allow detachment of the pit bottom from the carbide.

5.8.3   Two-step epitaxially embedded SiC nanodots

Alternatively, we employ a two-step capping process, where the first 5 nm of Si are deposited at 250ºC, followed by 45 nm of Si at 500ºC. Figure 5-28 shows two semicoherent epitaxially embedded SiC nanodots. We note the absence of extended stacking faults or threads into the capping layer, thus the misfit dislocations arising from Si/SiC strain relief are confined directly at the heterointerface.
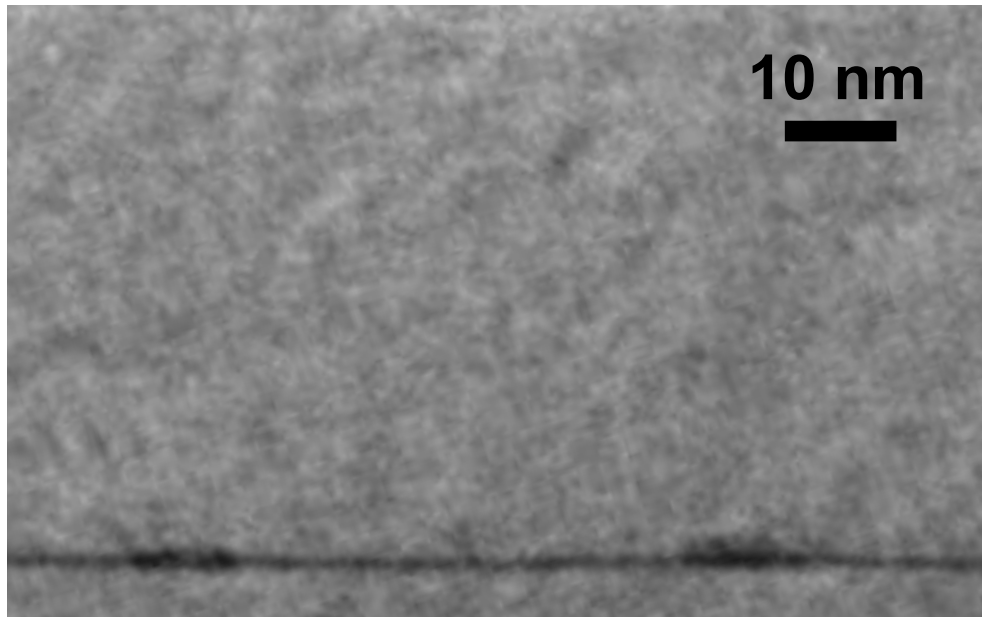
Figure 5-28: HR-TEM of a SiC nanodots encapsulated in Si using a two-step procedure: 5 nm at 250°C followed by 45 nm at 500°C.

Using this two-step capping process, it is possible to ensure conformal overgrowth during initial deposition at low temperatures. During the first kinetically limited growth step, misfit dislocations are grown-in to the top Si/SiC interface and buried with 5 nm of Si. As observed during 50 nm of low-T capping, we infer that a partially sheared dislocation boundary does initially form around the edges of the SiC. However, when heating to 500°C during continued Si capping, the surface diffusion lengths are increased. This allows any rotated overgrowth to relax to perfect coherency and the Shockley partial dislocated boundaries to glide inward and annihilate. Thus, the lengthy deposition time at 500°C (45 nm in 63 min) effectively anneals out existing dislocations. Other works have shown that such in-situ annealing can aid in condensation of extended dislocations or faults to confined locations at heterointerfaces [137].

5.9   Other observations

5.9.1   Edge effects

For fine pitch arrays, we observe edge effects including peripheral step bunching and enlarged dot volumes around the array perimeter. Figure 5-29 shows an example of long-range step bunching encompassing nearly the entire array edge-length. Step bunching was also observed on FIB templates with a greater pitch of 250 nm [138]. However, on FIB templates, step-bunching occurs around each FIB milled site rather than at the array boundary. Considering the reduced pitch of ~35 nm, the array *unit cell* occupancy with SiC is large, thus there exists a greatly reduced area for step flow inside the template area.

Furthermore, the width of the step-bunching region around the array can be used as a metric for the lengthscale of Si "supply" during carbidization at 780ºC. At the edge-center, the width of the depleted lower terrace is 250 nm, suggesting Si uptake from at least this distance. The increased supply of Si at the array periphery and the lack of internal step-flow growth thus leads to enhanced edge dot volumes compared to interior SiC sites. These edge effects are directly related to the SiC array density, thus maintaining a uniform distribution at the array edges will be more challenging for finer pitch templates.
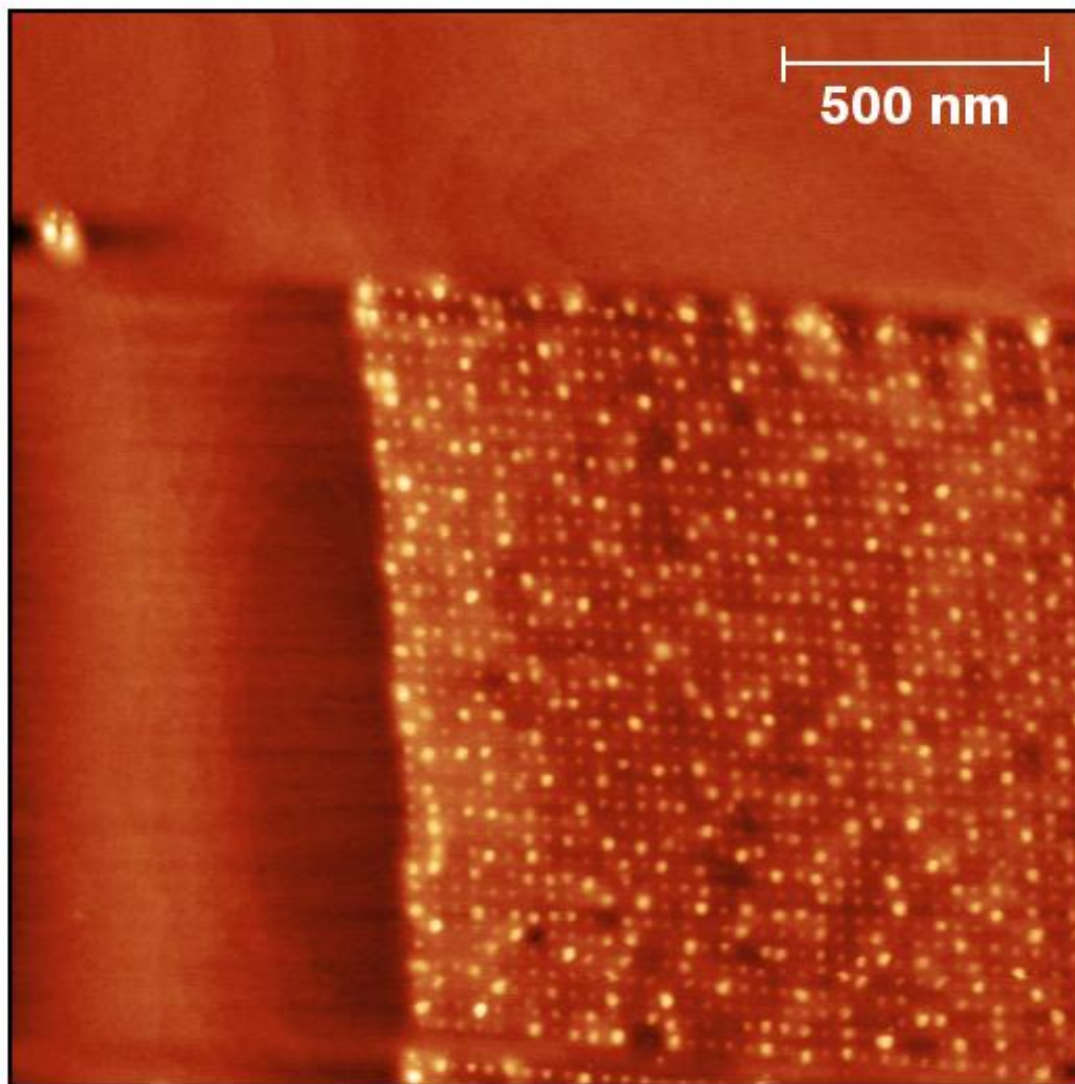
Figure 5-29: Step bunching is commonly observed at SiC template array periphery.

5.9.2 SiC splitting

During an extended post-annealing experiment splitting of a significant fraction of SiC nanodots was observed. Figure 5-30 is a labeled AFM image highlighting three distinct flavors of nanodots. First, the smallest dots have a relatively uniform size

distribution. Alternatively there exists a lower density of enlarged dots, in most cases these dots are monolithic, but we also observe many "split", enlarged dots.

During the initial SiC formation, we previously observed that larger SiC dots can contain low angle grain boundaries or stacking faults, as shown in Figure 5-11. With lengthy annealing times, we also have shown that some carbides tend to non-uniformly collect a dilute alloy overlayer (Figure 5-15,15). Thus, during rampant overgrowth and coarsening, SiC islands with preexisting SFs have a tendency to split along the boundary. We then suggest that planar boundaries within the SiC nanodots represent high energy interfaces owing to the nanodot's small volume. High temperature annealing can then activate Si interdiffusion through the planar boundary, creating pairs of smaller, monolithic SiC nanodots.
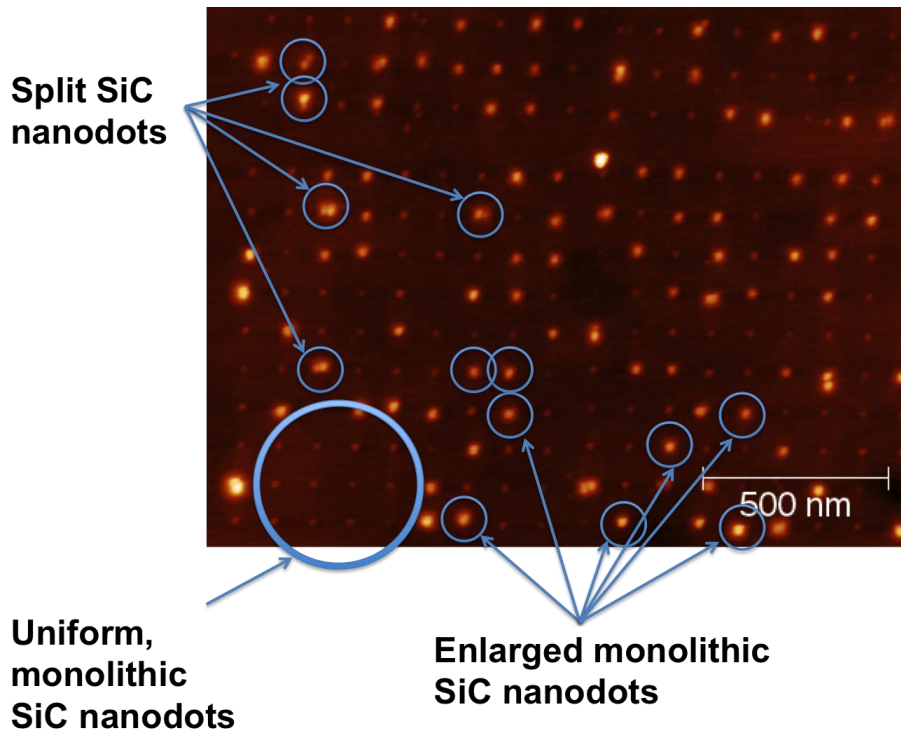
Figure 5-30: AFM image of a 100 nm spacing array of SiC nanodots after 30 min post-annealing at 700ºC. Three flavors of resultant dots are labeled, (1) small, uniform SiC nanodots, (2) enlarged, uniform nanodots, and (3) pairs of split nanodots.

The distribution of nanodot volumes shown in Figure 5-30, is similar to the bimodal distribution shown in Figure 5-15. The average volume of the uniform, small nanodots is 244nm^3, and the trough in the distribution is approximately 600 nm^3. The mean volume of monolithic enlarged dots is 760 nm3, and the combined volumes of split-pairs of nanodots ranges from 700-1500 nm^3. Using these statistics, a high temperature annealing "process diagram" is suggested in Figure 5-31. The boundary at 600 nm^3 represents the maximum stable SiC volume beyond which non-uniform coarsening and splitting *may* occur with extended high temperature annealing. We have previously suggested that the final island distribution can never be better than the

distribution immediately following carbidization. Thus, by accurately controlling the time-temperature exposure of the C_xH_y during dehydrogenation and carbidization, one can in principle stabilize templated nanodots from adverse behavior during high temperature heat treatment for T≤700ºC.
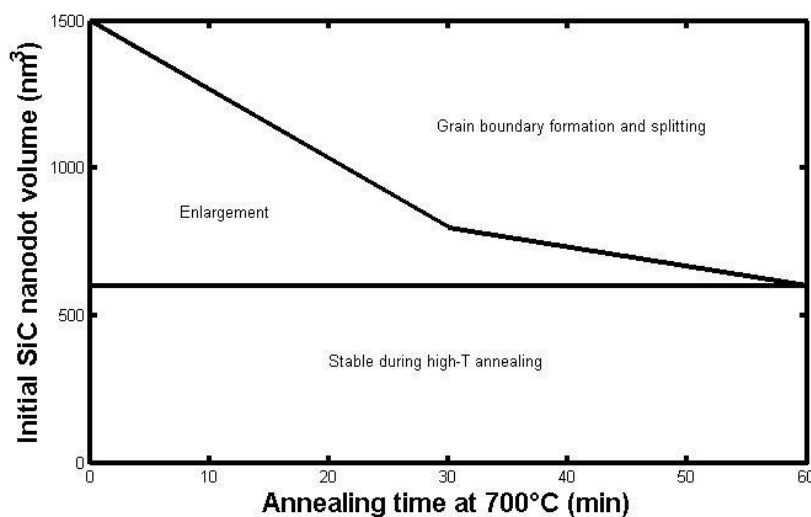
Figure 5-31: 700ºC post-annealing "process diagram" for SiC nanodots. Compare to Figure 5-15(c).

5.10 Conclusions

Our goal in this work, building on previous results [4], was to refine and better understand the carbide-based methodology for directing self-assembly of 3D Ge quantum dots. To further understand what the templated topography corresponds to and directly analyze the Ge/SiC interaction, high resolution AFM, TEM, and HAADF-STEM was performed.

In this study, we have determined that any volume accumulation cannot be accounted for solely by SiC or Ge coarsening. We show that limited C_xH_y coarsening

does occur at 500°C, but it is likely that C and/or SiC coarsening continues throughout the entire carbidization, oxide desorption, and Ge growth process. Our work suggests that minimizing the time-temperature product prior to the conversion of the C_xH_y nanodots to SiC is crucial to keeping the narrowest possible distribution in the templated array. This is of key importance, since we ultimately find that the composite Si/Ge/SiC template size distribution can never be better that that of the bare SiC.

High resolution TEM analysis confirms that the templated carbides are the cubic 3C-SiC polymorph and are epitaxially formed on Si in a "cube-on-cube" orientation. These carbides are near-fully strain relaxed by an array of misfit dislocations that wrap around their perimeter. Furthermore, we observe no excess Ge accumulation to form a morphological quantum dot, nor even conformal wetting of the carbide template sites. Apparently, the large chemical and lattice mismatch between Ge and SiC, combined with proximal, lower-energy Si (001) surface sites, results in complete Ge avoidance of the carbide under conditions of high adatom mobility.

A series of Si encapsulation experiments show that low-temperature Si does epitaxially overgrow the carbides without formation of extended stacking faults or dislocations in the overlayer. Thus, despite the avoidance of Ge directly over the SiC nanodot, the fully epitaxial nature of the resulting Si/SiC/Si heterostructures appears promising for the creation of artificial molecules with nanoscale strain modulation for engineered electronic and spintronic properties.

Chapter 6: Electronic properties and confinement mechanisms

6.1   Details of electrical measurements

In this study, we conducted electrical measurements of qubits with varying dimensions. The qubits consisted of groups of one to six nanodots arranged to mimic the six sides of a die; the interdot separations were varied from 22nm to 90 nm. For electrical measurements, a vertical contact stack was fabricated above each qubit as shown in Figure 6-1. For contact (or gating), we deposited an Al adhesion layer, for ohmic contact directly to Si, and a Au overlayer. SiO_2 was used as a barrier film. Note: device fabrication was performed by Dongyue Yang at the University of Pittsburgh (Pitt) following MBE-Si encapsulation of the qubit heterostructures at the University of Virginia (UVA).
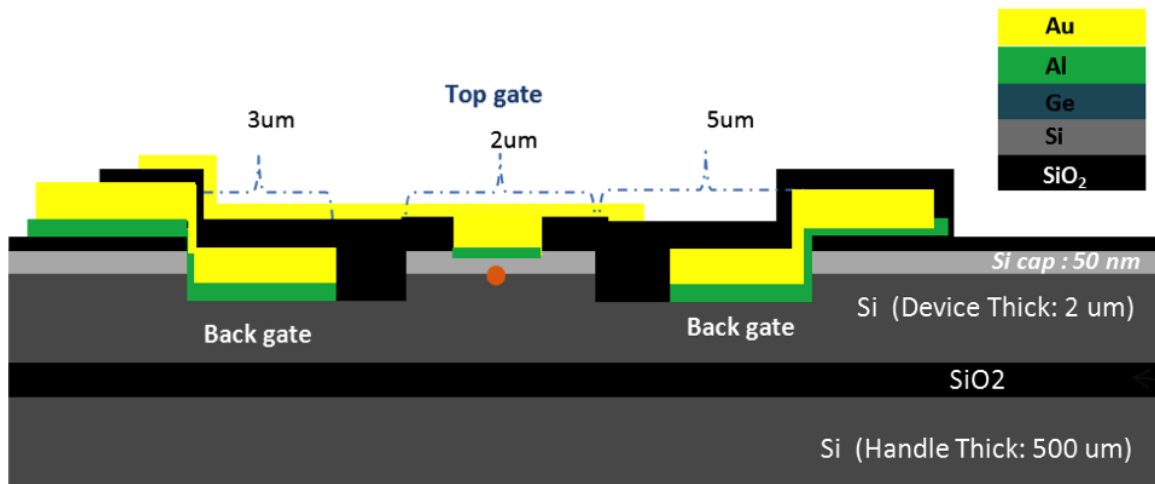
Figure 6-1: Schematic of multilayer devices fabricated at Pitt by Dongyue Yang for vertical transport measurements.

Several qubits were patterned on a single substrate and arranged in a 2D grid for simultaneous device fabrication. Figure 6-2 shows two optical images of the final

crossbar structures with top- and bottom-contacts. Figure 6-3 is a cartoon schematic showing the vertical contacts and the device orientation during measurement in a physical property measurement system (PPMS) housed at Pitt. The specimen was placed in a dilution refrigerator (DR) and cooled to 70 mK. Current – Voltage (I-V) curves are obtained as a function of an externally applied magnetic field (B-field) in the range of ±6 Tesla (T). Measurement of each I-V-B map requires over 8 hours of sampling time.
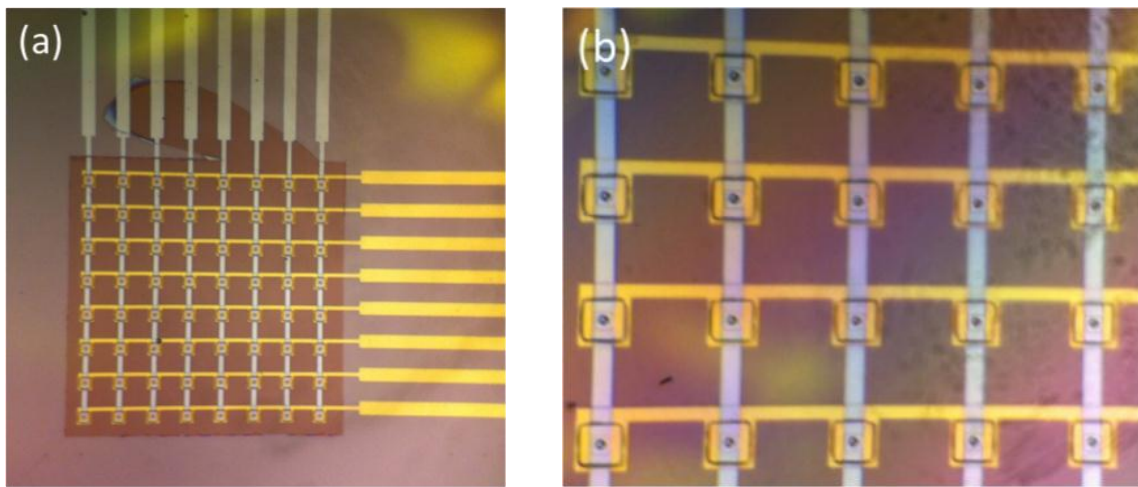
Figure 6-2: Optical images of crossbar devices for vertical transport measurements.
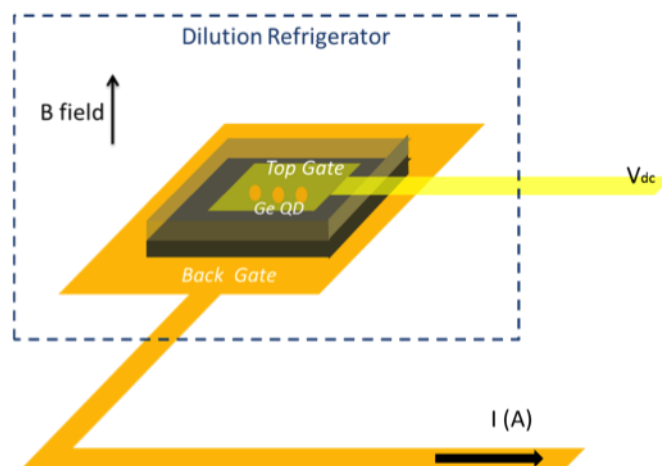
Figure 6-3: Cartoon schematic of the vertical contacts and the device orientation during measurement in a PPMS.

6.2 Observed electrical properties

The electrical results presented here very preliminary and not yet well understood. A collaborative group in the physics department at Pitt is conducting this phase of the project. In this section we show some exemplary spectra and aim to correlate the electrical phenomena with our characterized nanostructures.

For reference, vertical transport through a sample region void of SiC nanodots is measured as shown in Figure 6-4. The measured area is approximately $1um^2$ and is simply a Si/Ge/Si 2D quantum well (QW). In the 3D color spectra, we note symmetric, linear B-V behavior. The opposite voltage response to applied magnetic field is a possible indication of Zeeman splitting arising from confinement on either (or both) sides of the Ge wetting layer. The bottom panel shows an I-V curve at about -1.7T. Periodic current spikes with voltage are possible signatures of resonant tunneling behavior through the same thin Ge wetting layer.
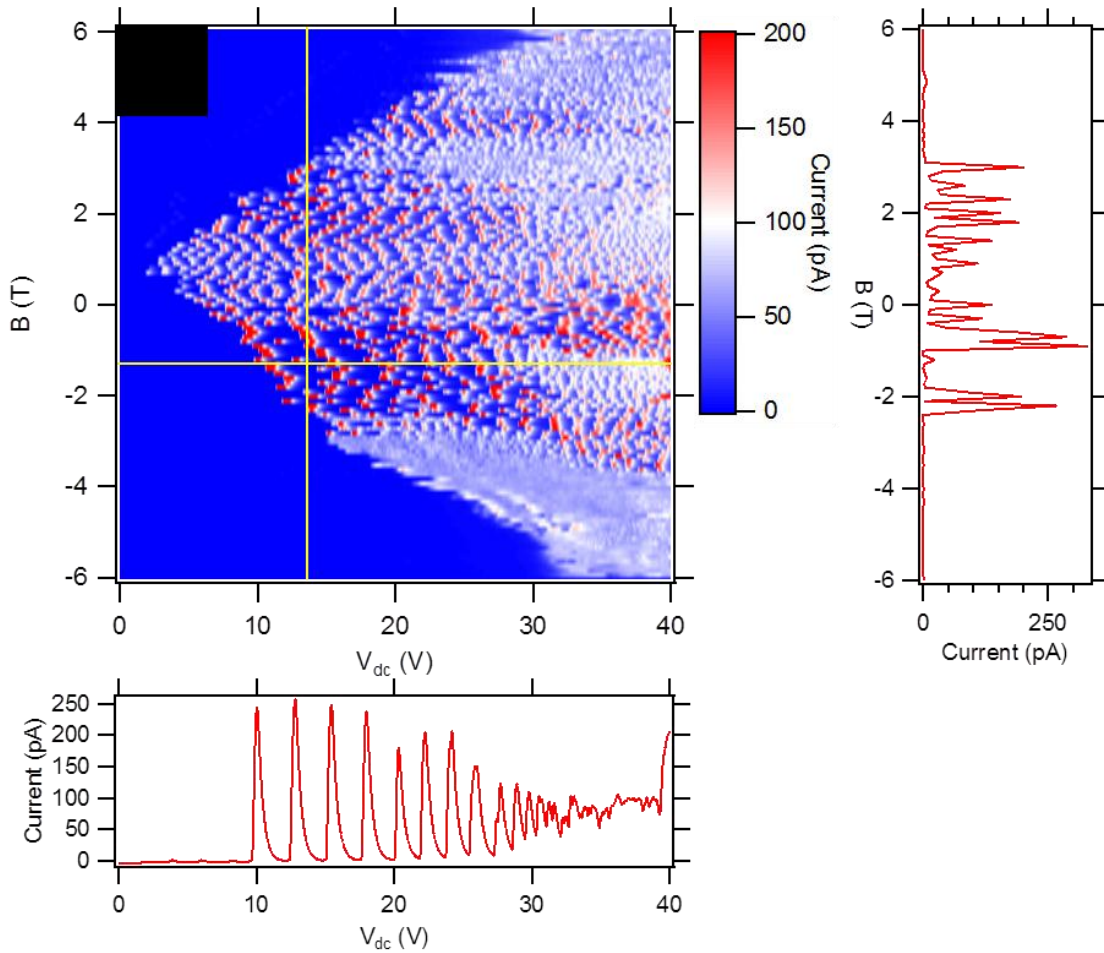
Figure 6-4: I-V-B map of the 'zero dot' reference device, the color scale is current. (right) I-B plot. (bottom) I-V plot.

In this report, for simplicity, we only show vertical transport results for the '1' and '2' nanodot cases (Figure 6-5). In the '2'-nanodot system, the interdot separation is 22nm. As previously discussed, wavefunction overlap between confined electrons is restricted to distances <35 nm and the interaction is expected to be enhanced for reduced distances. In both the '1' and '2' dot systems, we observe symmetric B-V trends akin to the 'zero-dot case', which is a signature of the Si/Ge/Si QW around the SiC nanodot. Furthermore, in the presence of '1' and '2' qubits, we also observe dual current peaks

near applied magnetic fields of +/-2T. We speculate that enhanced current at these

discrete magnetic fields is evidence of selective confinement of polarized carriers with

respect to the applied magnetic field. That is, confined carriers of opposite spin occupy

the SiC nanodot dependent upon the direction of the applied magnetic field. This is a

encouraging evidence that our templated nanodots are weakly confining electrons.
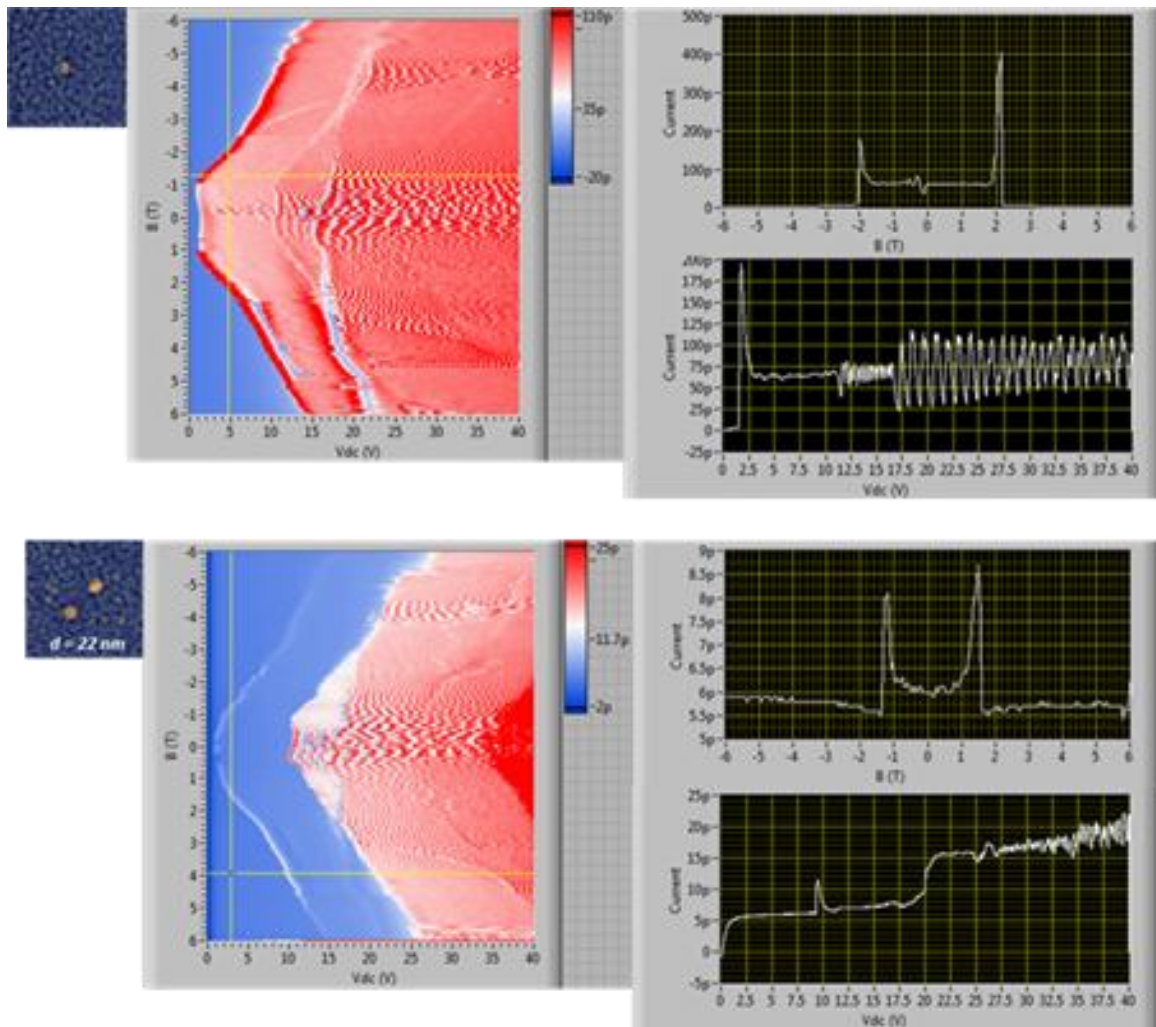
Figure 6-5: For each qubit: 1 and 2 dot cases, we show the resulting electrical measurement plots. (left) SEM image of no-dot area. (middle) I-V-B map, the color scale is current. (top right) I-B plot. (bottom right) I-V plot.

We also observe multiple current levels as a function of applied voltage under fixed magnetic field, (lower right panels in Figure 6-5). One explanation for the additional current peaks may be charging to a second discrete energy level. It is important to note that current oscillations observed at high applied voltage are a result of measurement error.

In summary, we find that the presence of small qubits containing 1 or 2 nanodots have a significant impact on the I-V-B spectra. Symmetric linear B-V behavior is evidence of Zeeman split energy levels arising from the Ge wetting layer (QW) in all specimen. Additionally, split current spikes as a function of magnetic field suggest polarized carrier confinement within the templated qubit structures. The observation of multiple current peaks as a function of voltage suggests charging of additional energy levels within confining potential wells. Although the electrical results presented here are not fully understood, in this chapter we examine a few materials-related features that may contribute to our magnetotransport observations.

6.3   Potential mechanisms for electrical observations

Since we have shown that the idealized nanostructure of the patterned nanodots is not valid, it is important to discuss the implications of the real atomic structure and hypothesize how our films are interacting under the applied electrical conditions. In this section, we discuss two simple models and propose future nanostructures for fabrication that may confirm these mechanisms.

6.3.1   Incoherent multilayers

The lattice mismatch between Si (Ge) and SiC is -20% (-23%), which cannot be supported elastically even in a single monolayer. As a result, a periodic array of misfit dislocations exists at the Si/SiC interface, as discussed in Chapter 5. However, the highly misfitting SiC nanodots will still present a significant strain perturbation in the overgrown Si film due to incomplete SiC relaxation and extended elastic strain fields from the dislocation cores. Figure 6-6 presents a schematic representation of the expected nanoscale strain modulation. The precise magnitude of the resultant strain fields will vary with carbide size and their spatial extent is unknown. A simple molecular dynamics (MD) model has been developed to calculate these strains for a Si/SiC bilayer system and is presented in Section 6.4.
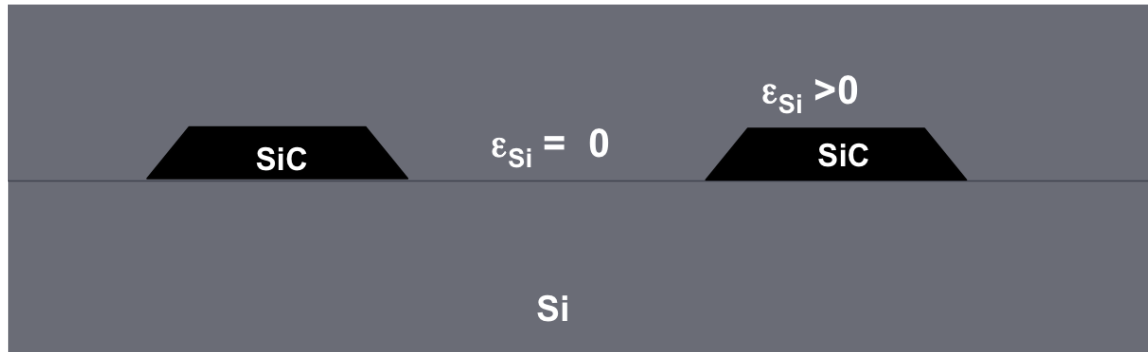
Figure 6-6: Schematic representation of embedded SiC nanodots in a Si matrix. The proposed magnitudes of strain modulation in the Si overlayer are labeled.

Alternatively, the presence of a thin Ge interlayer between the Si cap and the SiC nanotemplate may enhance the magnitude of the strain. Ultra-thin films of Ge (1-3 ML) grow pseudomorphically on Si, resulting in compressive strains of -4.2% in the Ge film. However, Ge and SiC have a lattice mismatch of 23%, which is expected to result in a

completely incoherent interface [139–141], exhibiting zero strain. This Ge film, going

between growth on Si and growth on SiC, is thus strain-modulated on the lengthscale of

the templated nanodots. It follows that a thin Si film overgrown on top of the strain-

modulated Ge will exhibit +4.2% tensile strain above each templated nanodot and be

unstrained in-between. A schematic showing the heteroepitaxial strain levels is shown in

Figure 6-7 (compare to Figure 6-6).
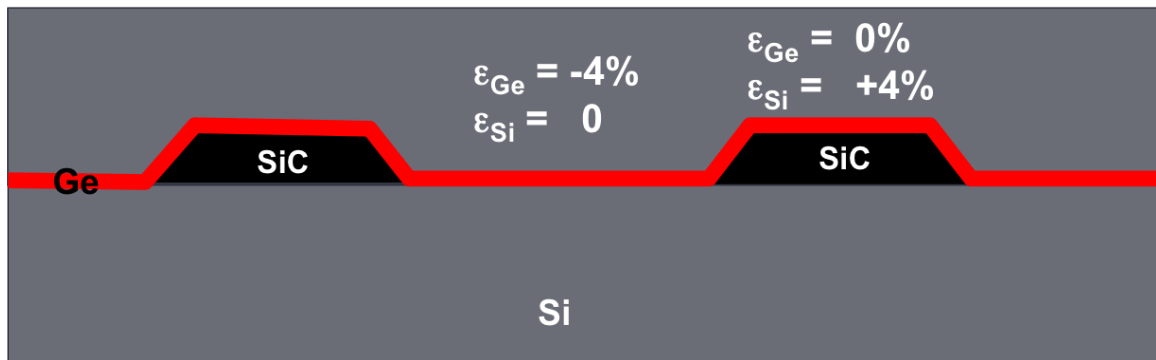
Figure 6-7: Schematic representation of SiC nanodots with an conformal coverage of Ge
and embedded in Si. The magnitude of strain modulation in the Ge and Si overlayers is
labeled.

Although these mechanisms of strain modulation are different from the initial,

idealized embedded Ge QD system, the strains involved with SiC precipitate inclusion

may still provide weak interfacial quantum wells. Furthermore, the strain levels predicted

here are lower than the 4.2% strain at a Ge/Si(001) interface, which implies shallower

confining wells and hence greater wavefunction decay lengths. It follows that interdot

coupling may be active over wider separations.

6.3.1.1   Future Work

Our current data suggests that Ge overgrowth at elevated temperatures (T>300ºC) results in Ge—SiC repulsion. To ensure conformal Ge overgrowth, it will be required to deposit Ge at, *or near*, room temperature. Fortunately, Ge epitaxy is known to be possible at these low temperatures [47,104]. All films investigated here have a Ge interlayer, which *does not coat* the SiC nanotemplates. Assuming the inter-dot pseudomorphic Ge film does not contribute to the strain in the Si capping layer, the existing films are expected to behave like the Si/SiC/Si multilayers. To confirm the possibility of Si-strain induced band bending at the Si/SiC interfaces, it will be necessary to fabricate two additional samples: (1) one with a room-temperature Ge thin film and (2) one Si/SiC/Si multilayer stack without Ge.

6.3.2   Silicon bottleneck model

In an alternative picture, we correlate the observed nanostructure with the vertical transport properties. For the reference device with no SiC nanodots, the system is simply a Si/Ge/Si multilayer stack. Here, the pseudomorphic, compressively strained Ge interlayer behaves as a weak 2D tunnel barrier to vertical electron transport. Similarly, when a SiC nanodot is present, the SiC interlayer also presents a barrier to vertical transport. However, surrounding the SiC nanodots, there may exist a narrow annulus of tensile strained Si that is devoid of Ge. This geometry is illustrated in Figure 6-8. The nano-annulus will thus have a reduced barrier for vertical transport resulting in a "bottleneck" – *preferential* – conduction path around the carbide.

Clearly, the vertical transport measurements show that the presence of qubit structures causes a significant perturbation on electrical behavior. The surprising aspect of this is that the 10 nm nanodots represent less than a 0.01% fractional area of the contact region. Incorporating the "bottleneck" model, we note two attractive features. First, since conduction is directed around the wide-band gap SiC barrier, all misfit dislocations might be avoided by carriers allowing one to dismiss their typical adverse effects on performance. And secondly, a greater threshold voltage is observed for the "no dot" case which is consistent with a continuous Ge tunnel barrier and the lack of a preferential conduction path via a nanoannulus.

Extensive electrical characterization has been conducted using a specimen with a 1.5 ML Ge layer grown at 600ºC. This specimen was structurally characterized in detail in Chapter 5. To confirm our "bottleneck" model hypothesis, it is critical to grow an identical specimen *without* the thin Ge layer. The ideal film here would simply be a SiC template film, capped with 50 nm of Si using the two-step procedure discussed in Chapter 5. If the Si "bottleneck" picture is accurate, when no Ge is present there will be little barrier to vertical transport, even in the presence of a SiC qubit structure. Thus, one would expect to observe no difference between the reference device and a qubit structure. Alternatively, if one were to increase the Ge interlayer thickness, the reference barrier to vertical conduction would also increase, resulting in an even greater threshold voltage.
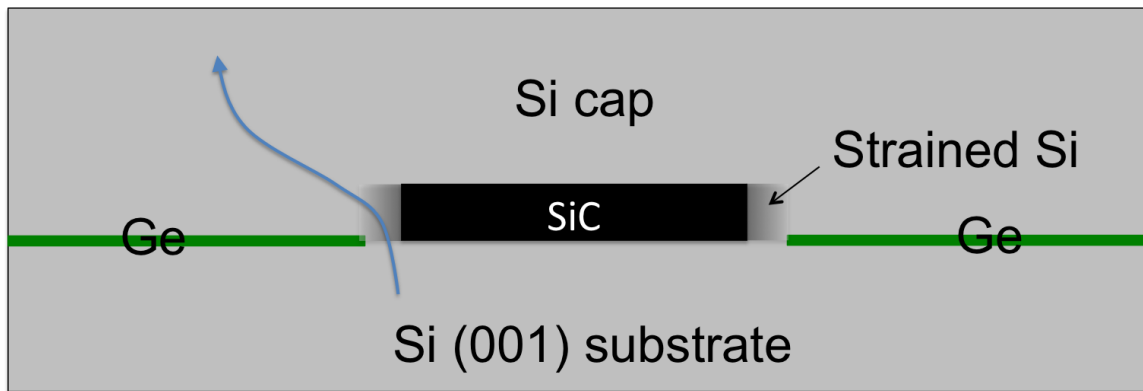
Figure 6-8: Cross-section illustration of the Si-nanoannulus bottleneck model.

6.3.3   A possibility for deterministic Ge self-assembly

As shown in Chapter 5, SiC nanodots can be epitaxially embedded in Si. Using a two-step capping procedure, the misfit dislocations are confined to the SiC/Si heterointerface, the defect density is reduced, and the free Si surface is re-planarized. This final surface may then be ideal for subsequent Ge island growth. The spatial extent of the misfit dislocation strain field is unknown, however, it is expected that long-range residual strains may aid *early* nucleation of Ge islands in SiC templated areas.

To test this, it is suggested to grow a series of Si-capped SiC templates with variable cap thicknesses (1-20 nm) followed by a constant thickness of Ge (5 ML) at 550ºC. Since the pre-existing surface will be planarized and the SiC buried, there are no additional topological or chemical perturbations, but instead pure strain modulation. It will thus be straightforward to determine the amount of preferential accumulation and the island species by shape. [35]

6.4   Molecular dynamics simulations

Nanoscale strain modulation is the key enabler for realization of shallow potential wells necessary for weak carrier confinement. Although we have not achieved the morphological QDs originally intended, we can accurately place, and epitaxially embed highly strain-mismatched SiC nanoprecipitates in Si. These heterostructures are expected to have extended strain fields caused by incomplete relaxation and/or physical perturbations from misfit dislocations and geometrical incorporation in the film.

If one knew the magnitude and spatial extent of these strain fields, it might be possible to predict the resulting band structure. For the purposes of this study, we are mostly interested in the strain fields caused by interfacial misfit dislocations. To calculate atomic level strains, we turn to molecular dynamics modeling. We use a simplistic bilayer model of a Si film on a SiC substrate. In order to impose periodic boundary conditions, the computational cell uses increments of 4 unit cells (UC) Si on top of 5 UC of SiC. The SiC is unstrained while the Si film is tensile strained to ~1%. The top and bottom surfaces are free. One quarter of the computational cell is depicted in Figure 6-9.

For the purposes of this study, we use a simple relaxation algorithm to solve for the lowest energy positions of an arrangement of atoms. In this "quasi-dynamic" approach to relaxation, the position and velocity of each atom is calculated and the velocities are reset to zero at each time step when the kinetic energy reaches a maximum. Similar approaches have been previously used to look at small atomic displacements involved with dislocation formation and interdiffusion [142,143]. The simulations conducted here used a time step of 0.1ps and typically ran for ~12 hours on a single node of the UVA cluster system.
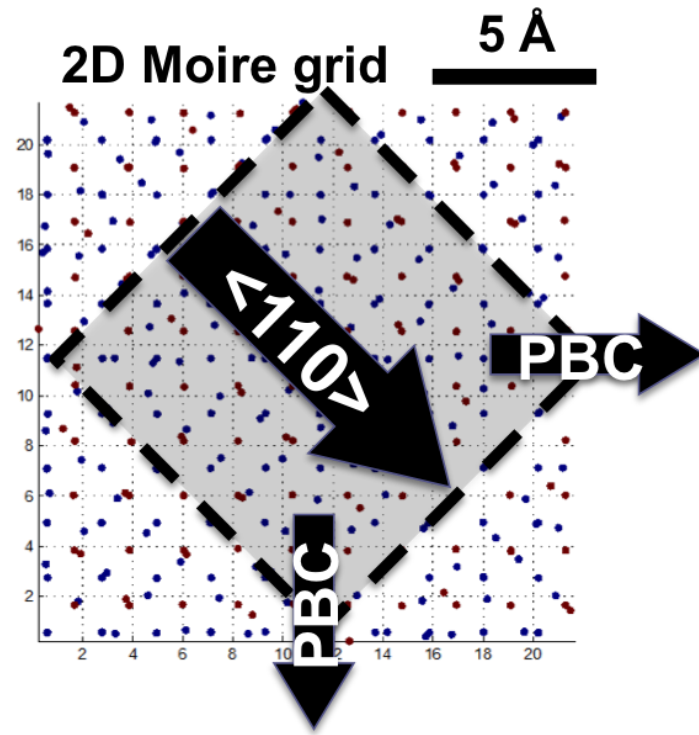
Figure 6-9: One quarter of the Si/SiC bilayer computational cell used for MD simulations.

6.4.1   Dislocation strain fields

At a misfitting interface, the beat frequency of the Moiré fringes and the frequency of edge-type misfit dislocations can both be determined by Equation 6-1, and are simple functions of the bulk lattice interplanar spacings. In our investigations of Si/SiC, misfit dislocations run along the <110>, and are edge-on in our TEM specimen.

$$d_{Moiré} = \frac{d_{Si}d_{SiC}}{d_{Si} - d_{SiC}} = 1.62 \; nm \qquad\qquad \text{Equation 6-1}$$

In Figure 6-10(left) we show a potential energy map directly from the Si/SiC interface in the computational cell. Light blue lines running along the <110> direction denote perfect edge-type dislocations and red nodes denote locally high-energy positions where the misfit dislocations intersect. Figure 6-10(right) is a slice of the computational cell taken perpendicular to one of the dislocation lines. The black trace directly shows the extra half-plane in the SiC substrate with a Burgers vector of a/2<110> type.

In this highly misfitting system, it is non-trivial to reproduce other relaxation mechanisms such as stacking faults or extended threads. In order to utilize periodic boundary conditions, it is necessary to match the boundaries of the computational cell requiring that one either (1) impose an initial 20% strain on one of the constituent films or (2) use the closest ratio of numbers of unit cells that can minimize the strain in both films. We have used the latter method in this case, which, in-effect builds in the misfit dislocations since their periodicity is equivalent to the bulk Moiré fringe periodicity. Thus, we note that other relaxation mechanisms are possible, but not captured in this model. Nonetheless, this perfect array of misfit dislocations is sufficient to calculate the spatial extent of the resulting strain fields.
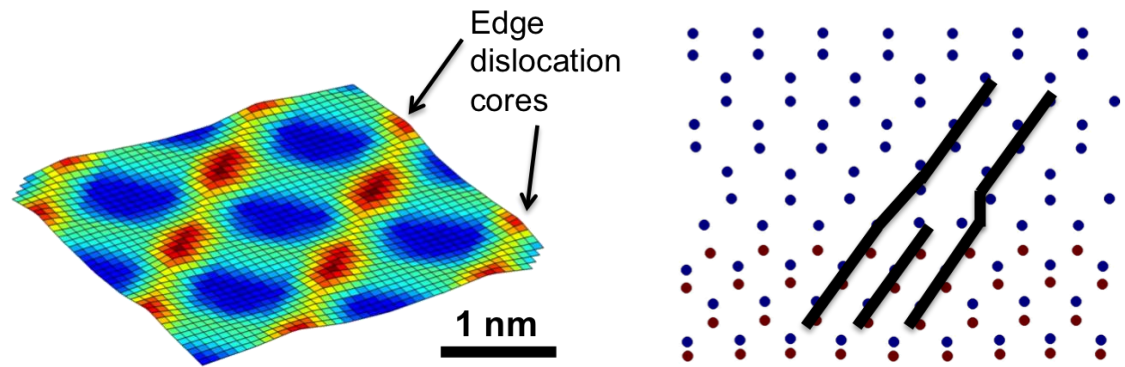
Figure 6-10: (left) Potential energy map of the energy relaxed computational cell. Light blue lines denote edge dislocation cores. (right) A cross-sectional view taken through one of the dislocation lines. The black lines denote the perfect edge dislocation.

In the relaxed heterostructure, we use the mean atomic displacements in each atomic layer to infer the range of the misfit dislocation strain field. Figure 6-11 displays the calculated average strain in each monolayer in the Si film above the heterointerface, as labeled on the abscissa. The in-plane strain is in tension up to ~3% at the interface and fully relaxes within 4 monolayers. More interestingly, the perpendicular (ZZ) displacement is compressed to -0.5% and relaxes to null within 4 monolayers, or one unit cell.
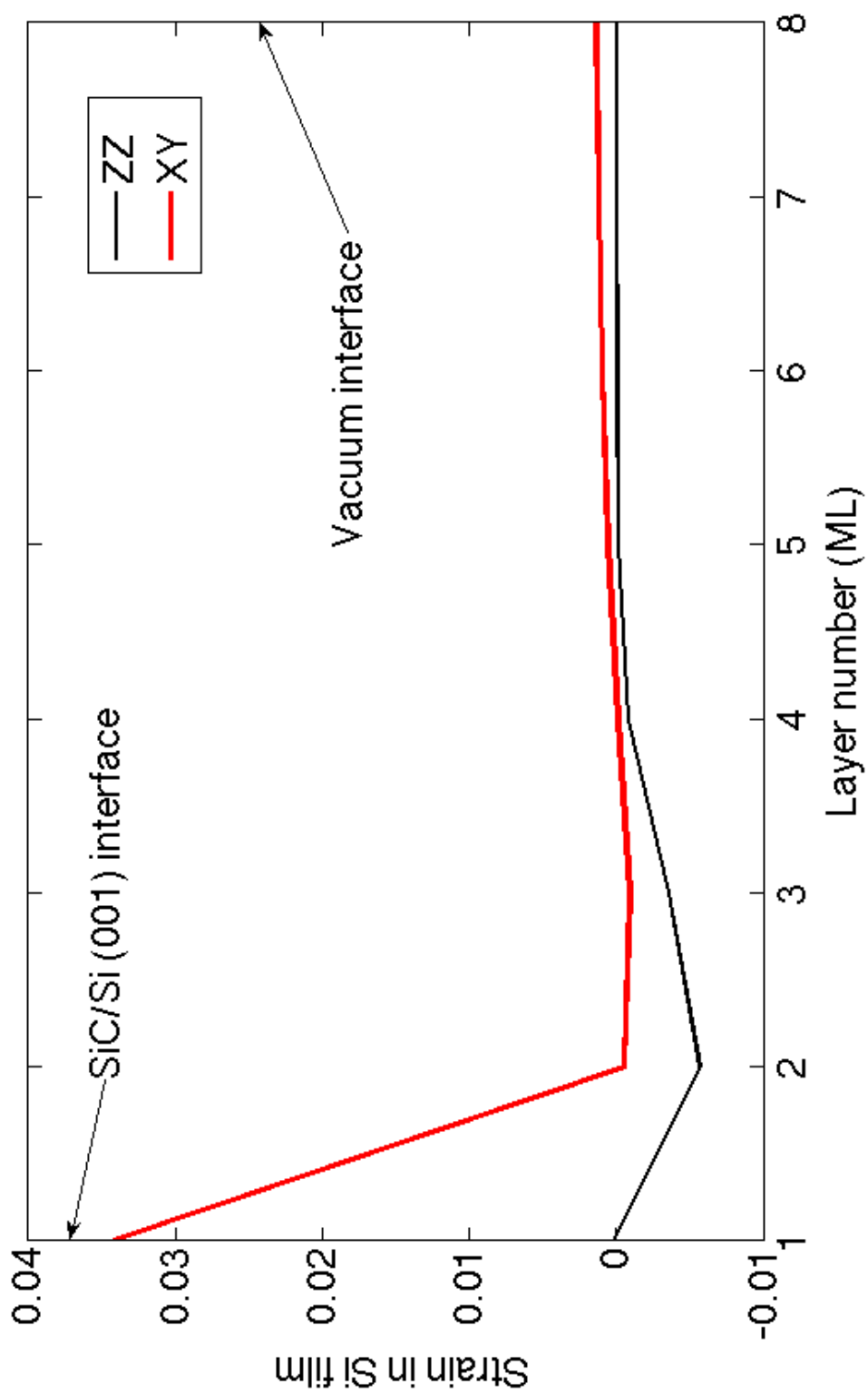
Figure 6-11: Average atomic displacements in each monolayer in the Si film above the Si/SiC interface.

Ultimately, we can use the MD calculated strain in the Si film to predict the Si/SiC interfacial band-bending. Empirical deformation potentials for Si are used to calculate the local change in bandgap as a function of strain [7,144]. The resulting Si/SiC band structure is predicted in Figure 6-12. The conduction-band and valence-band deformation potentials are 10.5eV and 1.1 eV, respectively [144]. The depth of the conduction band potential well in the <110> direction is 0.36eV. Although the origin of the nanoscale modulated strain is different from the idealized Ge/Si heterostructures, we believe this SiC-based patterning route may still provide the confinement potentials desired for spintronic device exploration.
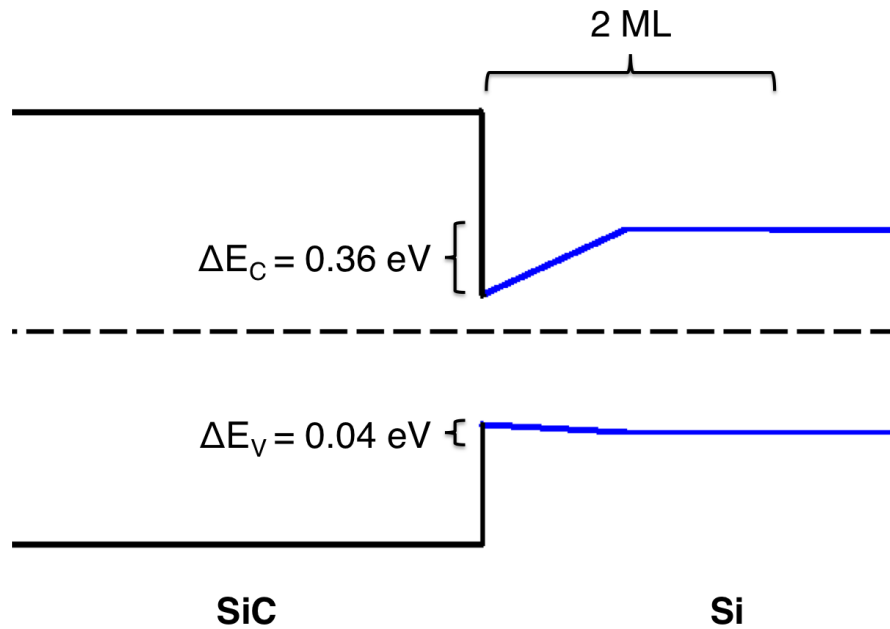
Figure 6-12: Si/SiC interfacial band structure calculated using the XY strain component from Figure 6-11 and deformation potentials reported by Fischetti. [144]

Chapter 7: Auxiliary Projects

In this chapter, we present background information, existing results, and suggested future work for side projects that are outside the scope of this dissertation. These experiments include the study of hyperthermal growth using magnetron sputtering in our HyperMBE and the nanoindentation of ultra-thin resist layers. These projects were completed in collaboration with NanoSTAR undergraduate summer fellows, Mr. Andrew Fish and Mr. Mehrad Mehr, respectively.

7.1   Hyperthermal growth of Ge/Si(001)

Our group's HyperMBE employs two variable-distance magnetron sputter guns for deposition of Ge and Si. These sources are operated with DC power up to 80W. Deposition rates can be varied between 0.1Å/s and 6.5Å/s depending on power and substrate-target separation, with no thermal loading of the sample. Using Stopping Range of Ions in Matter (SRIM) modeling, we estimate gaseous deposition species to have energies in the range 10-40eV upon exiting the sputter target. Although we have not determined the degree of thermalization of energetic Si and Ge while transiting from target to substrate, the mean free path of deposition species as a function of Ar pressure is calculated in Fig. 2-1. Thermalization may be avoided when the target-substrate distance is small, or if working pressure is reduced. Deposition with high energy species further enables the possibility of hyperthermal growth. Since surface diffusion rates are suggested to be much higher, increased deposition rates and lower temperatures are available for high quality film growth. The effects of adatom energy on films growth is summarized by Ensinger [51] in Figure 2-2.

7.1.1   Background

Few labs have reported hyperthermal growth in semiconductor systems. The most common techniques are ion assisted, such as Low Energy Ion Deposition (LEID) in the range of 1 eV – 1keV, and Ion Beam Assisted Deposition (IBAD) operating at >1keV. Ion assisted processing requires an ion beam that is directed to the substrate with an electric field bias; these ions interact primarily with near surface atoms promoting transport of thermalized deposition species.

In the energy range of 10-100eV, incident ion energy is much greater than the surface binding energy and shallow collision cascades may occur which can generate surface vacancies and adatoms from the substrate. Additionally, flux-generated surface phonons may couple with adatoms to promote mobility [51]. This process also tends to coarsen existing island distributions, as adatoms from small islands evaporate and condense on large islands [51].

Accordingly, if the ion energy is too high, the defect generation rate may surpass the rate of annhilation from annealing effects [51]. Thus, optimization of hyperthermal species energy is required to obtain adequate adatom mobility for smooth film growth and to avoid surface damage [145].

Semiconductor film growth using ion-assisted deposition has been demonstrated with Si and Ge [51,146–148]. At high ion energies (150-350eV) and low deposition rate (0.1-0.2Å/s), Ge islands have been shown to grow on SiO_2. With increased deposition rate and ion assist energy, the island size is reported to decrease while density increases. It is suggested that ion beams partially dissociate supercritical nuclei, increasing the adatom density and thus the nucleation rate [146].

Greene attempted hyperthermal homoepitaxial growth of Si/Si(001) by concurrent ion-beam sputtering and assist with Kr^+ ions [148]. With active species energies of E_{Kr}=15eV and E_{Si}=18eV the epitaxial thickness of Si in the temperature range of 80-300ºC is reported to increase by an order of magnitude. The use of energetic species is said reduce the rate of surface roughening, postponing the amorphous phase transition.

Though magnetron sputtering has been used for deposition of Si [149] and Ge [150] species, little evaluation of the effects of energetic deposition species has been demonstrated. Radio frequency (RF) magnetron sputtering of Si(001) homoepitaxy has been attempted by Vögeli [149] at 350-450ºC. STM was used to monitor the surface defect density and Ar working pressure was varied in the range of 1-33 mT to control the degree of thermalization. At the highest pressures the change in surface defect density is negligible, and the relative density increases linearly as the pressure is reduced. It is suggested that at the lowest pressures, more species exist in the high-energy tail of the sputtered atom energy distribution. Based on molecular dynamics simulations, atom energies greater than that for bulk displacement (14eV) are capable of breaking and reforming Si bonds at the surface. Resulting dimer vacancy defects are suggested to provide additional nucleation centers for 2D island formation, however the absolute amount of damage is minimal and assumed to anneal out in the time scale associated with 1 ML coverage. In the parameter space investigated here, high-energy species are not found to enhance surface mobility, but rather to alter the surface atomic structure.

7.1.2   Preliminary growth studies

Though somewhat elevated growth rates of Ge have been explored in the literature [151,152], none have approached 3-6Å/s for single crystal growth of Ge/Si(001), and no studies suggest deposition of crystalline Ge with energetic species. A series of recent growth experiments have provided two interesting observations.

First, multiple Ge thicknesses were deposited at 450°C and 0.5Å/s with a target-substrate distance of 1.5". Compared to our standard QD growth of 0.1Å/s at 450ºC, strain induced island nucleation is delayed, exhibiting metastable wetting layer thicknesses of 7ML, compared to 3 ML, as is illustrated in Figure 7-1. In both cases, the estimated volume consumed by QDs accounts for approximately 3 ML of thickness. Further analysis of representative islands reveals ~24% reduction in base width and 54% reduction in volume when increasing the deposition rate from 0.1Å/s to 0.5Å/s. All islands retain {105} faceting, indicated by 11° surface angles. Similar QD size range has been reported by Dashiell, et al. [153] at 360°C using a growth rate of 0.003Å/s and a coverage of 5.6 ML. From this we can conclude that at high deposition rates, the mean diffusion length before an adatom is incorporated into the film is reduced, thus increasing the deposition rate is analogous to reducing the growth temperature. However, deposition rate seems to have a particularly large effect on increasing the wetting layer thickness.
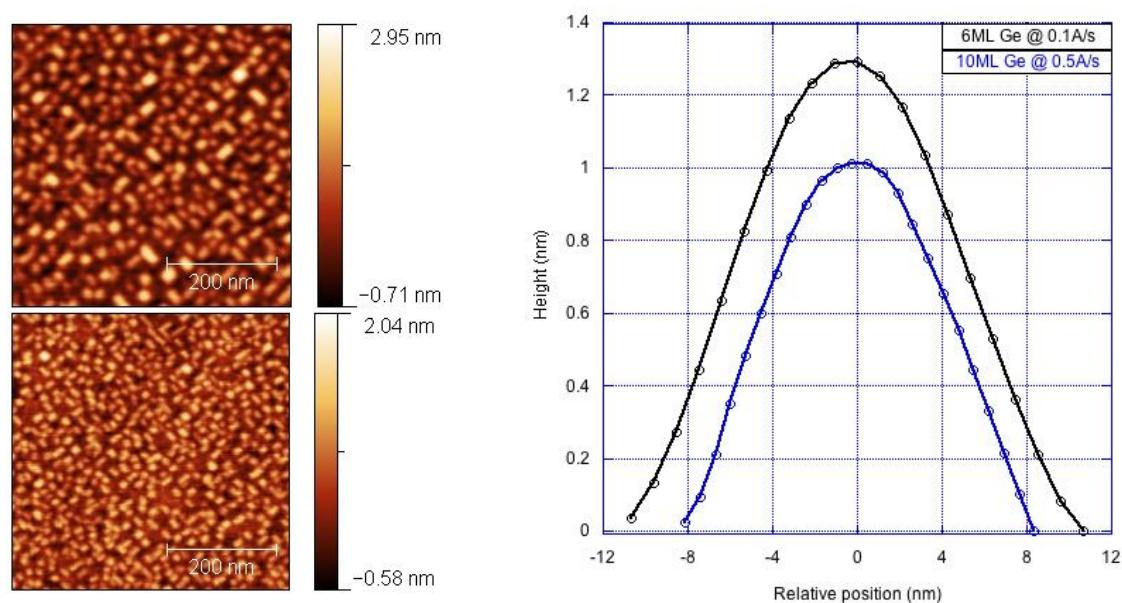
Figure 7-1:Ge QDs grown at 450°C with (top-left) 6ML at 0.1 A/s and (bottom-left) 10 mL at 0.5A/s, and (right) corresponding average hut linescans.

In an attempt to further suppress 3D island formation, the growth rate was pushed to 3-6Å/s. In addition to a high density of small islands, we surprisingly observed a population of very large islands, see Figure 7-2. At deposition rates this high, we would expect adatom diffusion lengths to be further reduced compared to the 0.5 Å/s growth shown in Figure 7-1, but that is obviously not the case. Note that this deposition was repeated, with very similar results. Thus, there is another mechanism promoting enhanced adatom mobility at work. One possible origin is strain relaxation in the large dots via both shape and misfit dislocations, that can drive anomalous coarsening [22,29,152]. However, denuded zones are not observed around the large islands. Additionally, using SRIM we estimate the Ge adatom energy to be >20eV at the large plasma power used to obtain high rate sputtering. This corresponds with the energy range of enhanced mobility suggested in Figure 1-2.
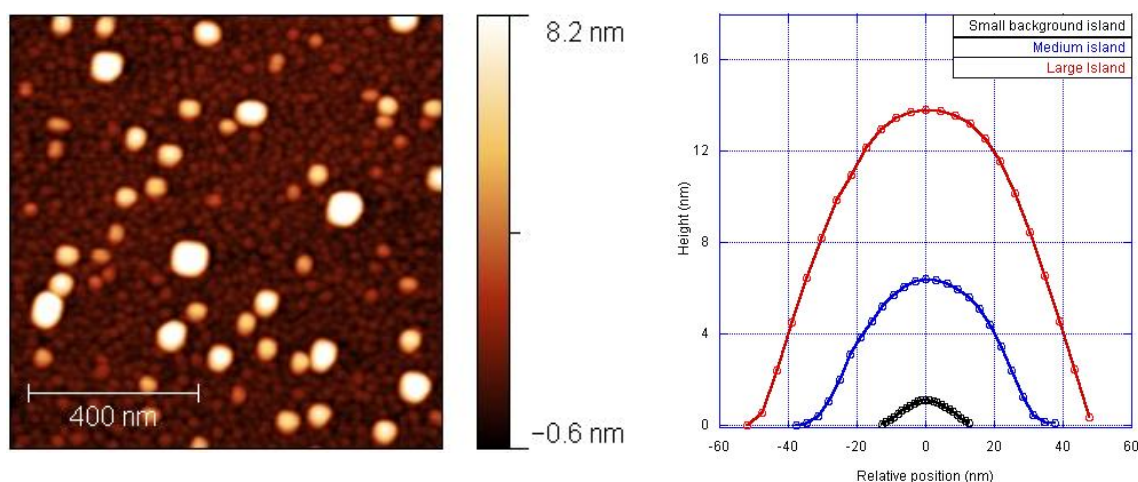
Figure 7-2: (Left) 1um AFM scan of Ge islands exhibiting a tri-modal size distribution after growth at 3.5A/s, thickness = 10 mL. Vertical scale has been shifted to emphasize background islands, actual +Z=15.1 nm. (Right) Average line scans of three different features. Islands have side angles of 6°, 20°, and 25°, respectively.

From the AFM data, the volume of Ge in large islands is found to include >40% of the total Ge volume, but occupies a projected area that represents only 19% of the scan region. Meanwhile the small islands include about 30% of the deposited volume. The resulting wetting layer thickness is 1-4 ML. Significant error in the WL thickness is due to difficulty in controlling film thickness at these high deposition rates.

To provide some information on the island composition, various selective wet-chemical etches were attempted. Figure 7-3 shows the surface morphology after etching with buffered oxide etch (BOE) and with $NH_4OH + H_2O_2$ (NHH). BOE is known to etch SiO_2 and GeO_2 at extremely high rate, thus smoothening of the background suggests the roughness was mostly due to oxidation (compare to Figure 7-2). NHH selectively etches Ge and $Si_{1-x}Ge_x$ (x>0.2)[27–32]. After 4s immersion in NHH, all large Ge islands are completely removed, leaving behind so-called tree-rings. Coherent islands are known to form "rings" as a mechanism of strain relaxation [154]. For dislocated islands, the

addition of concentric rings has been shown to directly correlate with the nucleation of a

single dislocation per ring [106]. The absence of additional rings in these samples

suggests that (1) the large islands are coherent or (2) due to the high deposition rate,

diffusion processes for ring formation are quenched. As a counterpoint, formation of such

large features suggests diffusion lengths must be extremely high, on order of the mean

island separation, 240 nm.
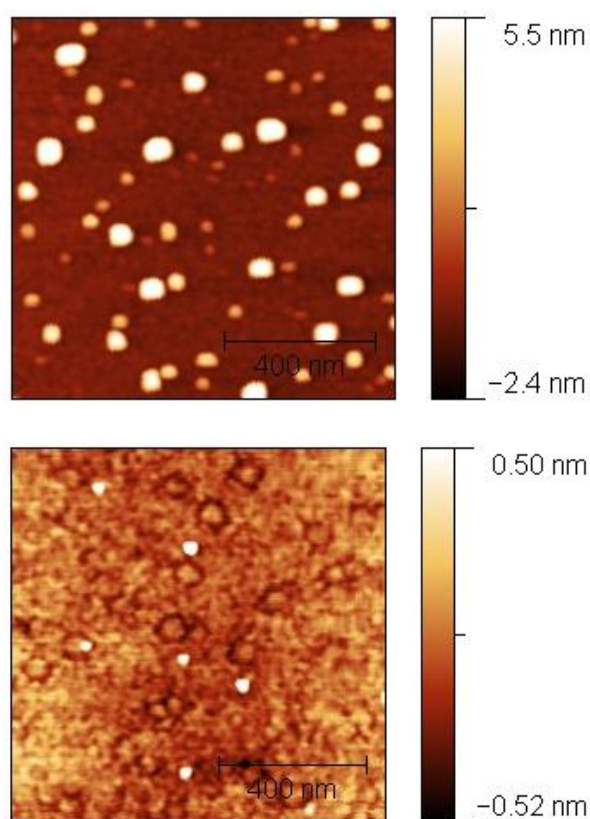
Figure 7-3: (Left) Large Ge islands only remain after 10s BOE etching, actual +Z=15.0
nm and (Right) all Ge is lost after subsequent etching for 4s in H2O2, actual +Z=2.0 nm.

Many questions exist about the growth mechanisms of Ge at high rate and low

temperature. In ongoing work we are performing a series of Raman spectroscopy

measurements with Dr. Thomas Beecham at Sandia National Laboratories to elucidate

the strain state of various QD surface as a function of growth rate and deposited film volume.

We have also performed cross sectional HR-TEM on specimen with enlarged Ge dots, akin to that shown in Figure 7-2. Micrographs of four irregular Ge islands are shown in Figure 7-4. The largest island (bottom left) has two stacking faults that extend to the substrate interface. The other three islands are at least semi-coherent, and free of extended faults. Interestingly, the free surface of the islands have irregular faceting behavior. Ongoing analysis and future TEM work will allow full structural characterization.
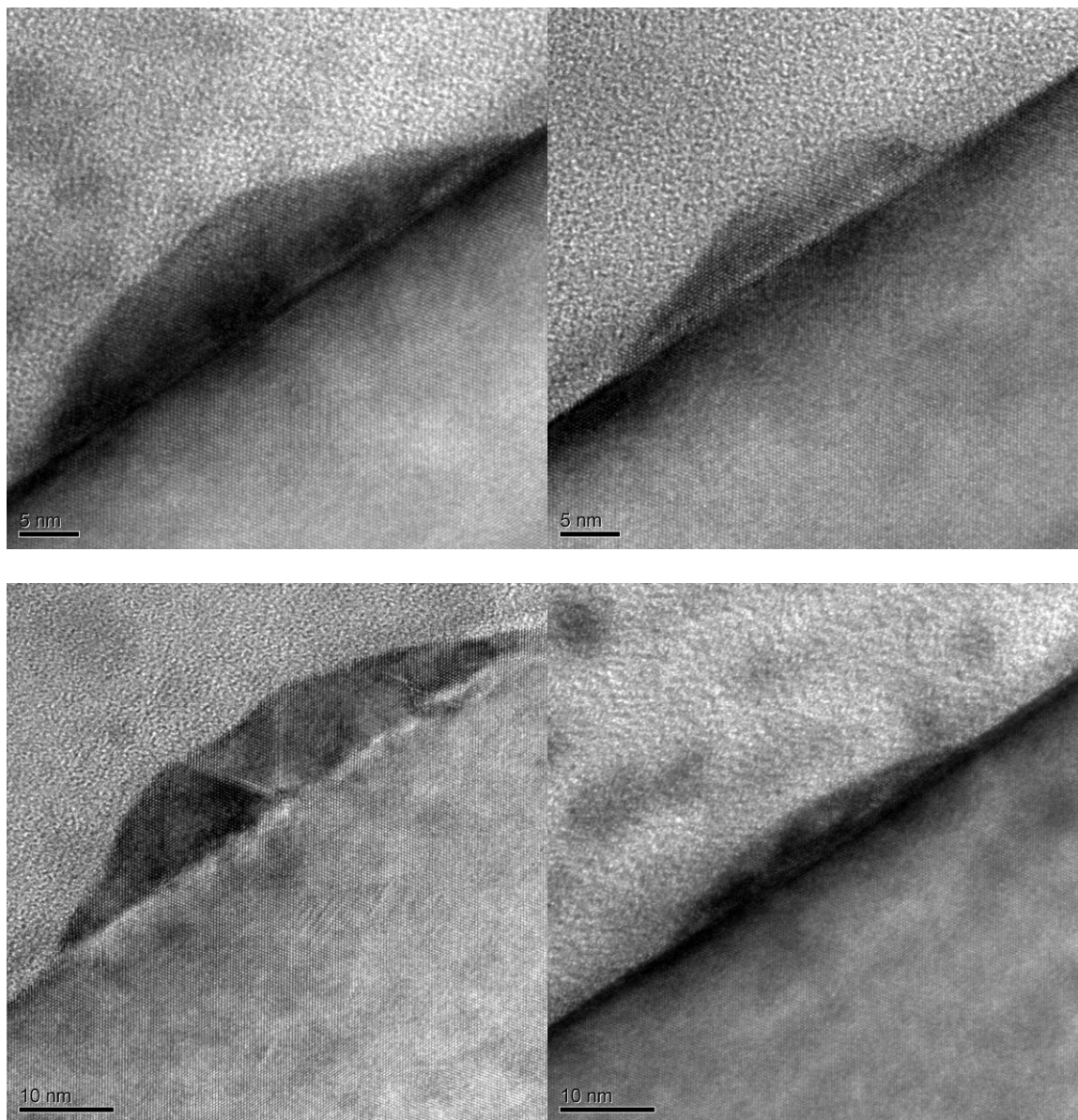
Figure 7-4: HR-TEM images of various irregular Ge/Si(001) islands formed during pseudo-hyperthermal Ge deposition.

Chapter 8: Conclusions

Our goal in this dissertation was two-fold: to refine and better understand the carbide-based methodology for directing self-assembly of 3-D Ge quantum dots; and to explore low-temperature growth processes for structurally perfect, device quality island encapsulation. To accomplish these objectives, we have investigated the structural and chemical composition of semiconductor thin films using high resolution AFM, TEM, and HAADF-STEM.

In previous work, it was suggested that SiC nanodots initiate self-assembly of Ge QDs at template sites, outlining a rapid-prototyping methodology for directed organization of 3-D islands. Following the work of Guise, et al. [4], we have studied the entire process flow in detail to evaluate the carbonaceous template formation on Si and the chemical interaction between Ge and SiC. Earlier work claimed that coarsening of templated sites was mediated by the interaction between Ge islands. On the contrary, we find that C_xH_y templates, produced by EBID, undergo extensive mass-loss and coarsening at 500°C; these processes are mediated by dehydrogenation and carbon-surface diffusion. As a result, loss of template uniformity occurs throughout the entire SiC formation process, requiring precise control over the total time-temperature product.

Even more intriguing, we find that Si and Ge overgrowth on SiC results in complete expulsion of the overlayer from template regions. Due to the narrow SiC nanodot size, proximal Si attachment sites are available which represent more energetically favorable Si-Si and Ge-Si bonding locations. Near-room temperature growth is required to kinetically limit diffusion and force Ge/SiC conformal overgrowth. However the result is a highly dislocated or incommensurate Ge/SiC heterointerface.

Thus, self-assembly of morphological Ge QDs on SiC nanodots is not observed due to large chemical and lattice mismatch between these species.

The optimized structure of the SiC islands is observed with high resolution TEM. SiC/Si(001) islands are disk-shaped, exhibiting the cubic 3C-SiC polymorph. These nanodots are epitaxially formed on Si in a "cube-on-cube" orientation, but are near-fully strain-relaxed through dense arrays of interfacially confined 90° and 60° misfit dislocations, and in some cases, carbide penetrating stacking faults.

A series of Si encapsulation experiments show that low-temperature Si does epitaxially overgrow the carbides without formation of extended stacking faults or dislocations in the overlayer. Thus, despite the avoidance of Ge directly over the SiC nanodot, the fully epitaxial nature of the resulting Si/SiC/Si heterostructures appears promising for the creation of artificial molecules with nanoscale strain modulation for engineered electronic and spintronic properties.

In a separate, but related experiment, we have investigated critical epitaxial thicknesses for low growth temperatures. Epitaxial growth of Si and Ge films for T<200°C has been shown to transform into defective and eventually the amorphous phase as a function of film thickness. This phenomena has been widely studied for homoepitaxial films and to a lesser extent during moderately strained heteroepitaxy. Here, we have employed lightly strained GeSi QD surfaces as a basis for ultra-low temperature Si overgrowth, which allow concurrent modulation of both strain and growth orientation. During encapsulation experiments, we found that growth orientation has a much more profound effect on the critical epitaxial thickness than low level surface

strain. This work allowed us to define a lower bound for fully coherent encapsulation growth temperatures as a function of the known surface topography.

Ultimately, encouraging electrical results confirm that our qubit patterning geometries are exhibiting unique spintronic behavior at low temperatures. Although the qubit structures are not the originally intended morphological Ge QD heterostructures, we have proposed multiple mechanisms for carrier confinement based on the directly observed structures. In effect, the qubit devices fabricated here may exhibit strain and/or structural modulations on sub-22nm length-scales that are ideal for the study of fundamental spin interactions.

References

[1]   S. A. Wolf, D. D. Awschalom, R. A. Buhrman, J. M. Daughton, S. von Molnár, M. L. Roukes, A. Y. Chtchelkanova, and D. M. Treger, Science **294**, 1488 (2001).

[2]   C. Felser, G. H. Fecher, and B. Balke, Angewandte Chemie International Edition **46**, 668 (2007).

[3]   D. D. Awschalom and M. E. Flatte, Nat Phys **3**, 153 (2007).

[4]   O. Guise, J. T. Yates, J. Levy, J. Ahner, V. Vaithyanathan, and D. G. Schlom, Appl. Phys. Lett. **87**, 171902 (2005).

[5]   O. Guise, J. Ahner, J. Yates, and J. Levy, Appl. Phys. Lett. **85**, 2352 (2004).

[6]   O. Guise, H. Marbach, J. Levy, J. Ahner, and J. T. Yates Jr., Surface Science **571**, 128 (2004).

[7]   C. E. Pryor, M. E. Flatté, and J. Levy, Appl. Phys. Lett. **95**, 232103 (2009).

[8]   V. Srinivasa, J. Levy, and C. S. Hellberg, Phys. Rev. B **76**, 094411 (2007).

[9]   J. Levy, Phys. Rev. A **64**, 052306 (2001).

[10]   F. Meier, J. Levy, and D. Loss, Phys. Rev. Lett. **90**, 047901 (2003).

[11]   F. Meier, J. Levy, and D. Loss, Phys. Rev. B **68**, 134417 (2003).

[12]   A. Imre, G. Csaba, L. Ji, A. Orlov, G. H. Bernstein, and W. Porod, Science **311**, 205 (2006).

[13]   B. T. Jonker, G. Kioseoglou, A. T. Hanbicki, C. H. Li, and P. E. Thompson, Nat Phys **3**, 542 (2007).

[14]   O. M. J. van 't Erve, A. T. Hanbicki, M. Holub, C. H. Li, C. Awo-Affouda, P. E. Thompson, and B. T. Jonker, Appl. Phys. Lett. **91**, 212109 (2007).

[15]   L. W. Snyman, M. du Plessis, E. Seevinck, and H. Aharoni, IEEE Electron Device Letters **20**, 614 (1999).

[16]   V. E. Ferry, M. A. Verschuuren, M. C. van Lare, R. E. I. Schropp, H. A. Atwater, and A. Polman, Nano Letters **11**, 4239 (2011).

[17]   T. M. Gibbons, B. Kang, S. K. Estreicher, and C. Carbogno, Phys. Rev. B **84**, 035317 (2011).

[18]   P. E. Hopkins, J. C. Duda, C. W. Petz, and J. A. Floro, Phys. Rev. B **84**, 035438 (2011).

[19]   S.-M. Lee, D. G. Cahill, and R. Venkatasubramanian, Applied Physics Letters **70**, 2957 (1997).

[20]   National Physical Laboratory. at <http://www.npl.co.uk/>

[21]   D. J. Eaglesham and M. Cerullo, Phys. Rev. Lett. **64**, 1943 (1990).

[22]   F. M. Ross, J. Tersoff, and R. M. Tromp, Phys. Rev. Lett. **80**, 984 (1998).

[23]   D. E. Jesson, G. Chen, K. M. Chen, and S. J. Pennycook, Phys. Rev. Lett. **80**, 5156 (1998).

[24]   J. C. Bean, T. T. Sheng, L. C. Feldman, A. T. Fiory, and R. T. Lynch, Appl. Phys. Lett. **44**, 102 (1984).

[25]   R. Hull, J. Gray, C. C. Wu, S. Atha, and J. A. Floro, J. Phys.: Condens. Matter **14**, 12829 (2002).

[26]   A. Vailionis, B. Cho, G. Glass, P. Desjardins, D. G. Cahill, and J. E. Greene, Phys. Rev. Lett. **85**, 3672 (2000).

[27]   J. A. Floro, G. A. Lucadamo, E. Chason, L. B. Freund, M. Sinclair, R. D. Twesten, and R. Q. Hwang, Phys. Rev. Lett. **80**, 4717 (1998).

[28]   G.-H. Lu and F. Liu, Phys. Rev. Lett. **94**, 176103 (2005).

[29]   M. R. McKay, J. A. Venables, and J. Drucker, Solid State Communications **149**, 1403 (2009).

[30]   O. Moutanabbir, S. Miyamoto, E. E. Haller, and K. M. Itoh, Phys. Rev. Lett. **105**, 026101 (2010).

[31]   A. A. Darhuber, V. Holy, P. Schittenhelm, J. Stangl, I. Kegel, Z. Kovats, T. H. Metzger, G. Bauer, G. Abstreiter, and G. Grübel, Physica E: Low-dimensional Systems and Nanostructures **2**, 789 (1998).

[32]   R. Magalhes-Paniago, G. Medeiros-Ribeiro, A. Malachias, S. Kycia, T. I. Kamins, and R. S. Williams, Phys. Rev. B **66**, 245312 (2002).

[33]   Appl. Phys. Lett. **83**, 5298 (n.d.).

[34]   A. J. Steinfort, P. M. L. O. Scholte, A. Ettema, F. Tuinstra, M. Nielsen, E. Landemark, D.-M. Smilgies, R. Feidenhans'l, G. Falkenberg, L. Seehofer, and R. L. Johnson, Phys. Rev. Lett. **77**, 2009 (1996).

[35]   G. Springholz, V. Holy, M. Pinczolits, and G. Bauer, Science **282**, 734 (1998).

[36]   J. F. Graham, C. D. Kell, J. A. Floro, and R. Hull, Nanotechnology **22**, 075301 (2011).

[37]   J. L. Gray, R. Hull, and J. A. Floro, J. Appl. Phys. **100**, 084312 (2006).

[38]   W. F. van Dorp and C. W. Hagen, J. Appl. Phys. **104**, 081301 (2008).

[39]   W. F. van Dorp, C. W. Hagen, P. A. Crozier, B. van Someren, and P. Kruit, Microelectronic Engineering **83**, 1468.

[40]   Y. D. Park, A. T. Hanbicki, S. C. Erwin, C. S. Hellberg, J. M. Sullivan, J. E. Mattson, T. F. Ambrose, A. Wilson, G. Spanos, and B. T. Jonker, Science **295**, 651 (2002).

[41]   K. A. Bratland, Y. L. Foo, P. Desjardins, and J. E. Greene, Appl. Phys. Lett. **82**, 4247 (2003).

[42]   U. Konig, E. Kasper, and H. J. Herzog, Journal of Crystal Growth **52, Part 1**, 151 (1981).

[43]   H. J. Gossmann, E. F. Schubert, D. J. Eaglesham, and M. Cerullo, ATT Bell Laboratories (1990).

[44]   D. J. Eaglesham, J. Appl. Phys. **77**, 3597 (1995).

[45]   O. P. Karpenko, S. M. Yalisove, and D. J. Eaglesham, J. Appl. Phys. **82**, 1157 (1997).

[46]   D. J. Eaglesham, H.-J. Gossmann, and M. Cerullo, Phys. Rev. Lett. **65**, 1227 (1990).

[47]   K. A. Bratland, Y. L. Foo, J. A. N. T. Soares, T. Spila, P. Desjardins, and J. E. Greene, Phys. Rev. B **67**, 125322 (2003).

[48]   D. P. Adams, S. M. Yalisove, and D. J. Eaglesham, Appl. Phys. Lett. **63**, 3571 (1993).

[49]   D. J. Eaglesham and M. Cerullo, Appl. Phys. Lett. **58**, 2276 (1991).

[50]   K. A. Bratland, Y. L. Foo, T. Spila, H.-S. Seo, R. T. Haasch, P. Desjardins, and J. E. Greene, J. Appl. Phys. **97**, 044904 (2005).

[51]   W. Ensinger, Nuclear Instruments and Methods in Physics Research Section B: Beam Interactions with Materials and Atoms **127-128**, 796 (1997).

[52]   C. Kell, Synthesis of Amorphous Ge:Mn Thin Films and Position-Controlled Ge:Si Self-Assembled Nanostructures, Masters, University of Virginia. (2009).

[53]   D. Smith, *Thin-Film Deposition: Principles and Practice*, 1st ed. (McGraw-Hill Professional, 1995).

[54]   M. W. Thompson, Philosophical Magazine **18**, 377 (1968).

[55]   J. G. Goodberlet, J. T. Hastings, and H. I. Smith, Journal of Vacuum Science & Technology B: Microelectronics and Nanometer Structures **19**, 2499 (2001).

[56]   C. W. Petz, D. Yang, J. Levy, and J. A. Floro, Unpublished.

[57]   R. L. Stewart, Phys. Rev. **45**, 488 (1934).

[58]   R. W. Christy, J. Appl. Phys. **31**, 1680 (1960).

[59]   E. H. Hirsch, Br. J. Appl. Phys. **11**, 547 (1960).

[60]   P. M. George and J. L. Beauchamp, Thin Solid Films **67**, L25 (1980).

[61]   M. Heyns, M. Meuris, and Paul Mertens. *Ultra Clean Processing of Silicon Surfaces: Proceedings of the Fourth International Symposium on Ultra Clean Processing of Silicon Surfaces (UCPSS '98), Held in Ostend, Belgium, September 21-23, 1998* (Uetikon-Zuerich, Switzerland, 1998).

[62]   P. Klapetek and I. Ohlídal, Ultramicroscopy **94**, 19 (2003).

[63]   P. Klapetek, I. Ohlídal, and J. Bílek, Ultramicroscopy **102**, 51 (2004).

[64]   N. Kato, H. Maruyama, and H. Saka, J Electron Microsc (Tokyo) **50**, 9 (2001).

[65]   H. Li and L. Salamanca-Riba, Ultramicroscopy **88**, 171 (2001).

[66]   J. Reyes-Gasga and R. García-García, Radiation Physics and Chemistry **64**, 359 (2002).

[67]   J. Tersoff, Phys. Rev. B **37**, 6991 (1988).

[68]   J. Tersoff, Phys. Rev. B **39**, 5566 (1989).

[69]   J. Tersoff, Phys. Rev. Lett. **64**, 1757 (1990).

[70]   M. Tang and S. Yip, Phys. Rev. B **52**, 15150 (1995).

[71]   Y. Ma and S. H. Garofalini, J. Chem. Phys. **128**, 084505 (2008).

[72]   M. Kitabatake, Journal of Vacuum Science & Technology A: Vacuum, Surfaces, and Films **8**, 3726 (1990).

[73]   G. D. Samolyuk, S. I. Golubov, Y. N. Osetsky, and R. E. Stoller, Journal of Nuclear Materials **418**, 174 (2011).

[74]   G. Xue, H. Z. Xiao, M.-A. Hasan, J. E. Greene, and H. K. Birnbaum, J. Appl. Phys. **74**, 2512 (1993).

[75]   J. E. Van Nostrand, S. J. Chey, M.-A. Hasan, D. G. Cahill, and J. E. Greene, Phys. Rev. Lett. **74**, 1127 (1995).

[76]   J. E. Van Nostrand, S. J. Chey, and D. G. Cahill, Phys. Rev. B **57**, 12536 (1998).

[77]   G. Xue, H. Z. Xiao, M.-A. Hasan, J. E. Greene, and H. K. Birnbaum, J. Appl. Phys. **74**, 2512 (1993).

[78]   J. A. Floro, E. Chason, L. B. Freund, R. D. Twesten, R. Q. Hwang, and G. A. Lucadamo, Phys. Rev. B **59**, 1990 (1999).

[79]   H.-J. Gossmann, P. Asoka-Kumar, T. C. Leung, B. Nielsen, K. G. Lynn, F. C. Unterwald, and L. C. Feldman, Appl. Phys. Lett. **61**, 540 (1992).

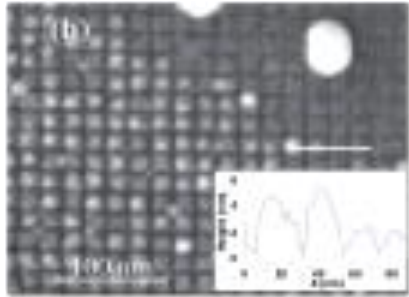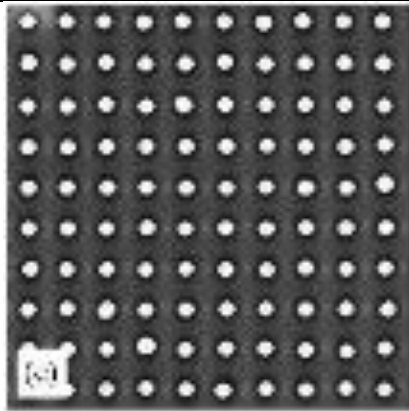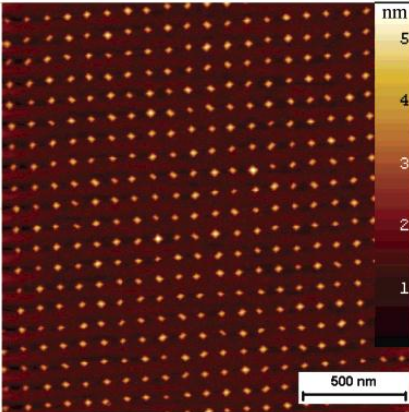[80]   H. Jorke, H.-J. Herzog, and H. Kibbel, Phys. Rev. B **40**, 2005 (1989).

[81]   J.-M. Baribeau, X. Wu, D. J. Lockwood, L. Tay, and G. I. Sproule, J. Vac. Sci. Technol. B **22**, 1479 (2004).

[82]   N.-E. Lee, D. G. Cahill, and J. E. Greene, Phys. Rev. B **53**, 7876 (1996).

[83]   K. A. Bratland, T. Spila, D. G. Cahill, J. E. Greene, and P. Desjardins, J. Appl. Phys. **109**, 063513 (2011).

[84]   P. Desjardins, T. Spila, O. Gürdal, N. Taylor, and J. E. Greene, Phys. Rev. B **60**, 15993 (1999).

[85]   A. Raviswaran and D. G. Cahill, Phys. Rev. B **69**, 165313 (2004).

[86]   J. H. Lin, Y. Q. Wu, J. Cui, Y. L. Fan, X. J. Yang, Z. M. Jiang, Y. Chen, and J. Zou, J. Appl. Phys. **105**, 024307 (2009).

[87]   G. Medeiros-Ribeiro, A. M. Bratkovski, T. I. Kamins, D. A. Ohlberg, and R. S. Williams, Science **279**, 353 (1998).

[88]   B. O. Kolbesen, J. Mähliß, and D. Possner, Phys. Stat. Sol. (A) **208**, 584 (2011).

[89]   B. Kolbesen, D. Possner, and J. Maehliss, in *ECS Transactions* (Washington, DC, 2007), pp. 195–206.

[90]   C. W. Petz and J. A. Floro, J. Appl. Phys. **110**, 023508 (2011).

[91]   J. Platen, B. Selle, I. Sieber, S. Brehme, U. Zeimer, and W. Fuhs, Thin Solid Films **381**, 22 (2001).

[92]   D. P. Adams and S. M. Yalisove, J. Appl. Phys. **76**, 5185 (1994).

[93]   W. Ranke, Phys. Rev. B **41**, 5243 (1990).

[94]   J. Knall, J. B. Pethica, J. D. Todd, and J. H. Wilson, Phys. Rev. Lett. **66**, 1733 (1991).

[95]   J. Myslivecek, C. Schelling, G. Springholz, F. Schäffler, B. Voigtländer, and P. Smilauer, Materials Science and Engineering B **89**, 410 (2002).

[96]   Y.-W. Mo, J. Vac. Sci. Technol. A **8**, 201 (1990).

[97]   J. A. Floro, P. G. Kotula, S. C. Seel, and D. J. Srolovitz, Phys. Rev. Lett. **91**, 096101 (2003).

[98]   S. G. Mayr and K. Samwer, Phys. Rev. Lett. **87**, 036105 (2001).

[99]   R. W. Smith and D. J. Srolovitz, J. Appl. Phys. **79**, 1448 (1996).

[100]   A. Malachias, M. Stoffel, M. Schmidbauer, T. Ü. Schulli, G. Medeiros-Ribeiro, O. G. Schmidt, R. Magalhães-Paniago, and T. H. Metzger, Phys. Rev. B **82**, 035307 (2010).

[101]   M. S. Leite, J. L. Gray, R. Hull, J. A. Floro, R. Magalhães-Paniago, and G. Medeiros-Ribeiro, Phys. Rev. B **73**, 121308 (2006).

[102]   M. Tomitori, K. Watanabe, M. Kobayashi, and O. Nishikawa, Applied Surface Science **76-77**, 322 (1994).

[103]   D. Yang, C. W. Petz, J. A. Floro, and J. Levy, Unpublished.

[104]   C. W. Petz and J. A. Floro, J. Appl. Phys. **110**, 023508 (2011).

[105]   G. Katsaros, A. Rastelli, M. Stoffel, G. Isella, H. von Känel, A. M. Bittner, J. Tersoff, U. Denker, O. G. Schmidt, G. Costantini, and K. Kern, Surface Science **600**, 2608 (2006).

[106]   T. Merdzhanova, A. Rastelli, M. Stoffel, S. Kiravittaya, and O. G. Schmidt, Journal of Crystal Growth **301-302**, 319 (2007).

[107]   H.-U. Danzebrink, L. Koenders, G. Wilkening, A. Yacoot, and H. Kunzmann, CIRP Annals - Manufacturing Technology **55**, 841 (2006).
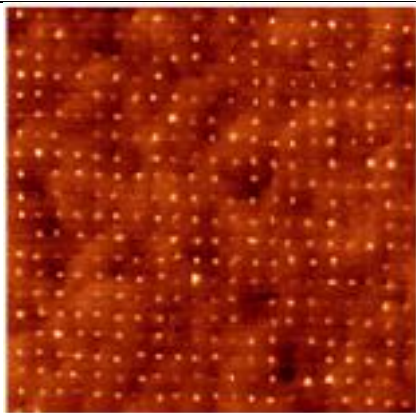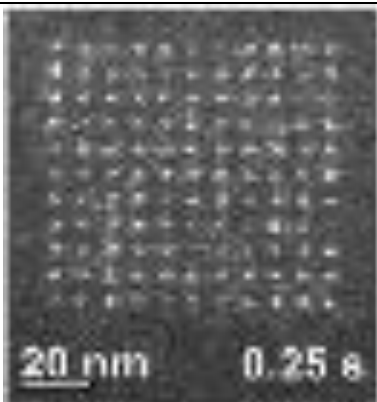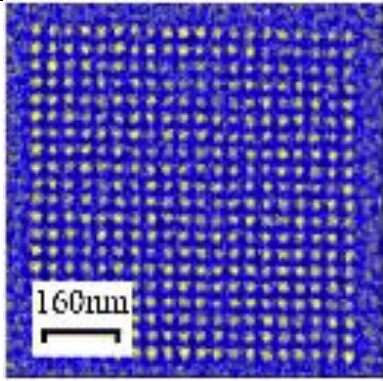
[108] C. K. Chung and B. H. Wu, Journal of Nanoscience and Nanotechnology **10**, 4679 (2010).

[109] C.-K. Chung and B.-H. Wu, Nanotechnology **17**, 3129 (2006).

[110] R. Hull, J. C. Bean, L. Peticolas, Y. H. Xie, and Y. F. Hsieh, MRS Online Proceedings Library **220**, (1991).

[111] L. B. Freund, Journal of the Mechanics and Physics of Solids **38**, 657 (1990).

[112] F. M. Morales, S. I. Molina, D. Araújo, R. García, V. Cimalla, and J. Pezoldt, Diamond and Related Materials **12**, 1227.

[113] N. Frangis, J. Stoemenos, J. V. Landuyt, A. Nejim, and P. L. F. Hemment, Journal of Crystal Growth **181**, 218 (1997).

[114] J. P. Li, A. J. Steckl, I. Golecki, F. Reidinger, L. Wang, X. J. Ning, and P. Pirouz, Appl. Phys. Lett. **62**, 3135 (1993).

[115] C. Long, S. A. Ustin, and W. Ho, Journal of Applied Physics **86**, 2509 (1999).

[116] G. Cicero, L. Pizzagalli, and A. Catellani, Phys. Rev. Lett. **89**, 156101 (2002).

[117] P. Pirouz, C. M. Chorey, T. T. Cheng&, and J. A. Powell, MRS Online Proceedings Library **91**, 399 (1987).

[118] C. Wen, Y. M. Wang, W. Wan, F. H. Li, J. W. Liang, and J. Zou, Journal of Applied Physics **106**, 073522 (2009).

[119] K. Zekentes, V. Papaioannou, B. Pecz, and J. Stoemenos, Journal of Crystal Growth **157**, 392 (1995).

[120] C. Schubert, U. Kaiser, A. Hedler, W. Wesch, T. Gorelik, U. Glatzel, J. Kräußlich, B. Wunderlich, G. Heß, and K. Goetz, Journal of Applied Physics **91**, 1520 (2002).

[121] P. Weih, V. Cimalla, T. Stauden, R. Kosiba, G. Ecke, L. Spiess, H. Romanus, M. Gubisch, W. Bock, T. Freitag, P. Fricke, O. Ambacher, and J. Pezoldt, Physica Status Solidi (c) **1**, 347 (2004).

[122] M. Diani, L. Kubler, L. Simon, D. Aubel, I. Matko, and B. Chenevier, Phys. Rev. B **67**, 125316 (2003).

[123] G. Hadjisavvas, P. Sonnet, and P. C. Kelires, Phys. Rev. B **67**, 241302 (2003).

[124] W. H. Weber, B.-K. Yang, and M. Krishnamurthy, Appl. Phys. Lett. **73**, 626 (1998).

[125] M. Krishnamurthy, J. S. Drucker, and A. Challa, Journal of Applied Physics **78**, 7070 (1995).

[126] K. Aït-Mansour, D. Dentel, J. . Bischoff, L. Kubler, M. Diani, A. Barski, M. Derivaz, and P. Noé, Physica E: Low-dimensional Systems and Nanostructures **23**, 428 (2004).

[127] M. De Seta, G. Capellini, L. Di Gaspare, F. Evangelisti, and F. D'Acapito, J. Appl. Phys. **100**, 093516 (2006).

[128] E. Sutter, P. Sutter, and J. E. Bernard, Appl. Phys. Lett. **84**, 2262 (2004).

[129] O. G. Schmidt, C. Lange, K. Eberl, O. Kienzle, and F. Ernst, Appl. Phys. Lett. **71**, 2340 (1997).

[130] F. K. LeGoues, M. C. Reuter, J. Tersoff, M. Hammar, and R. M. Tromp, Phys. Rev. Lett. **73**, 300 (1994).

[131] M. Hammar, F. K. LeGoues, J. Tersoff, M. C. Reuter, and R. M. Tromp, Surface Science **349**, 129 (1996).

[132] A. Rastelli and H. von Känel, Surface Science **515**, L493 (2002).
[133] T. Merdzhanova, S. Kiravittaya, A. Rastelli, M. Stoffel, U. Denker, and O. G. Schmidt, Phys. Rev. Lett. **96**, 226103 (2006).
[134] P. Ghatwai, TEM Investigation of Random Grain Boundary Migration, Masters, University of Virginia, n.d.
[135] W. Liu, P. C. Yang, C. A. Wolden, R. F. Davis, J. T. Prater, and Z. Sitar, Journal of Applied Physics **83**, 7658 (1998).
[136] D. A. Porter and K. E. Easterling, *Phase Transformations in Metals and Alloys, Second Edition*, 2nd ed. (CRC, 1992).
[137] A. Sakai, T. Tatsumi, and K. Aoyama, Applied Physics Letters **71**, 3510 (1997).
[138] J. Graham, Mass-Selecting Focused Ion Beam Templating of Heteroepitaxial Semiconductor Nanostructures, Ph.D., University of Virginia.
[139] C. J. Palmstrom, Annu. Rev. Mater. Sci. **25**, 389 (1995).
[140] A. Trampert, Physica E: Low-dimensional Systems and Nanostructures **13**, 1119 (2002).
[141] J. A. Floro, J. R. Michael, L. N. Brewer, and J. W. P. Hsu, Journal of Materials Research **25**, 1352 (2010).
[142] M. Kitabatake, M. Deguchi, and T. Hirao, J. Appl. Phys. **74**, 4438 (1993).
[143] M. Kitabatake, Journal of Vacuum Science & Technology A: Vacuum, Surfaces, and Films **9**, 91 (1991).
[144] M. V. Fischetti and S. E. Laux, Journal of Applied Physics **80**, 2234 (1996).
[145] K. Vanormelingen, B. Degroote, H. Pattyn, and A. Vantomme, Surface Science **561**, 147 (2004).
[146] S. Nikzad and H. A. Atwater, Surface and Coatings Technology **51**, 243 (1992).
[147] J. E. Yehoda, J. Vac. Sci. Technol. A **6**, 1631 (1988).
[148] J. E. Greene and N.-E. Lee, Nuclear Instruments and Methods in Physics Research Section B: Beam Interactions with Materials and Atoms **121**, 58 (1997).
[149] B. Vögeli, S. Zimmermann, and H. von Känel, Thin Solid Films **318**, 29 (1998).
[150] K. Das, M. L. N. Goswami, A. Dhar, B. K. Mathur, and S. K. Ray, Nanotechnology **18**, 175301 (2007).
[151] B. Cho, T. Schwarz-Selinger, K. Ohmori, D. G. Cahill, and J. E. Greene, Phys. Rev. B **66**, 195407 (2002).
[152] E. P. McDaniel, Q. Jiang, P. A. Crozier, J. Drucker, and D. J. Smith, Appl. Phys. Lett. **87**, 223101 (2005).
[153] M. W. Dashiell, U. Denker, C. Muller, G. Costantini, C. Manzano, K. Kern, and O. G. Schmidt, Appl. Phys. Lett. **80**, 1279 (2002).
[154] U. Denker, O. G. Schmidt, N.-Y. Jin-Philipp, and K. Eberl, Appl. Phys. Lett. **78**, 3723 (2001).
[155] L. E. Bell, Science **321**, 1457 (2008).
[156] A. Majumdar, Science **303**, 777 (2004).
[157] L. D. Hicks and M. S. Dresselhaus, Phys. Rev. B **47**, 16631 (1993).
[158] S. P. Hepplestone and G. P. Srivastava, Journal of Applied Physics **107**, 043504 (2010).
[159] B. Yang, J. L. Liu, K. L. Wang, and G. Chen, Applied Physics Letters **80**, 1758 (2002).

[160] G. Pernot, M. Stoffel, I. Savic, F. Pezzoli, P. Chen, G. Savelli, A. Jacquot, J. Schumann, U. Denker, I. Mönch, C. Deneke, O. G. Schmidt, J. M. Rampnoux, S. Wang, M. Plissonnier, A. Rastelli, S. Dilhaire, and N. Mingo, Nat Mater **9**, 491 (2010).

[161] D. Grützmacher, T. Fromherz, C. Dais, J. Stangl, E. Müller, Y. Ekinci, H. H. Solak, H. Sigg, R. T. Lechner, E. Wintersberger, S. Birner, V. Holý, and G. Bauer, Nano Lett. **7**, 3150 (2007).

[162] J. B. Haskins, A. Kinaci, and T. Çağin, Nanotechnology **22**, 155701 (2011).

[163] M. L. Lee and R. Venkatasubramanian, Applied Physics Letters **92**, 053112 (2008).

[164] D. G. Cahill, W. K. Ford, K. E. Goodson, G. D. Mahan, A. Majumdar, H. J. Maris, R. Merlin, and S. R. Phillpot, Journal of Applied Physics **93**, 793 (2003).

[165] D. G. Cahill, Review of Scientific Instruments **75**, 5119 (2004).

[166] D. G. Cahill, K. Goodson, and A. Majumdar, J. Heat Transfer **124**, 223 (2002).

[167] P. E. Hopkins, T. Beechem, J. C. Duda, K. Hattar, J. F. Ihlefeld, M. A. Rodriguez, and E. S. Piekos, Phys. Rev. B **84**, 125408 (2011).

[168] P. E. Hopkins, J. R. Serrano, L. M. Phinney, S. P. Kearney, T. W. Grasser, and C. T. Harris, J. Heat Transfer **132**, 081302 (2010).

Appendix 1: Patterning capabilities in the literature

Technique	Feature Size	Spacing	S/P?	Picture
Selective chemical etching at artificial dislocation sites	15 nm	20 nm	Parallel	 [Bavard, Phys Stat Sol 2006]
Traditional Photo-lithography + plasma etching	80 nm	150 nm	Parallel	 [Stoffel, Micro Elec J, 2006] Img=4.5um x 4.5um
EUV photolithography	10-80 nm	90 nm	Parallel	 [Grützmacher, Nano Lett 2007]

Focused ion beam	50 nm	90 nm	Serial	[Pascale, PRB 2008] Img=2.5um x 2.5um
TEM EBID	<10 nm	<10 nm	Serial	[van Dorp, Micro Elec Eng 2006]
EBL induced deposition (EBID) *This study*	<15 nm	<35 nm	Serial	[Guise, APL 2005]

Appendix 2: Deposition rates and calibrations

Calibration

We use a quartz crystal microbalance (QCM) from Maxtek for calibration of all deposition fluxes. In this device, a quartz crystal is actively oscillated during deposition. As mass collects on the crystal, the frequency (*f*) is damped, allowing one to calculate the amount of deposited material for a known density over a period of time. These quantities are related by the following equation:

$$h_f = \frac{N_q \cdot \rho_q}{\rho_f} \left(\frac{1}{f_o} - \frac{1}{f_1} \right)$$
Equation A2-1

where h_f is the film thickness, N_q is the frequency constant for the bare quartz crystal, ρ_q is the density of the quartz, ρ_f is the density of the film, and f_o, f_1 are the frequencies before and after deposition.

Deposition rate trends

Utilizing Equation A2-1, we can determine deposition rates with an uncertainty of approximately 0.01 Å/s. Figure A1 shows two deposition rate charts. In the top panel, DC sputtering deposition rates for Si are plotted for two linear translation distances. At 0", the gun is fully retracted from the substrate, resulting in an approximate 6" working distance. With a 2" translation, the working distance is approximately 4". The increase in

deposition rate is linear with power, but the effect of working distance is enhanced at
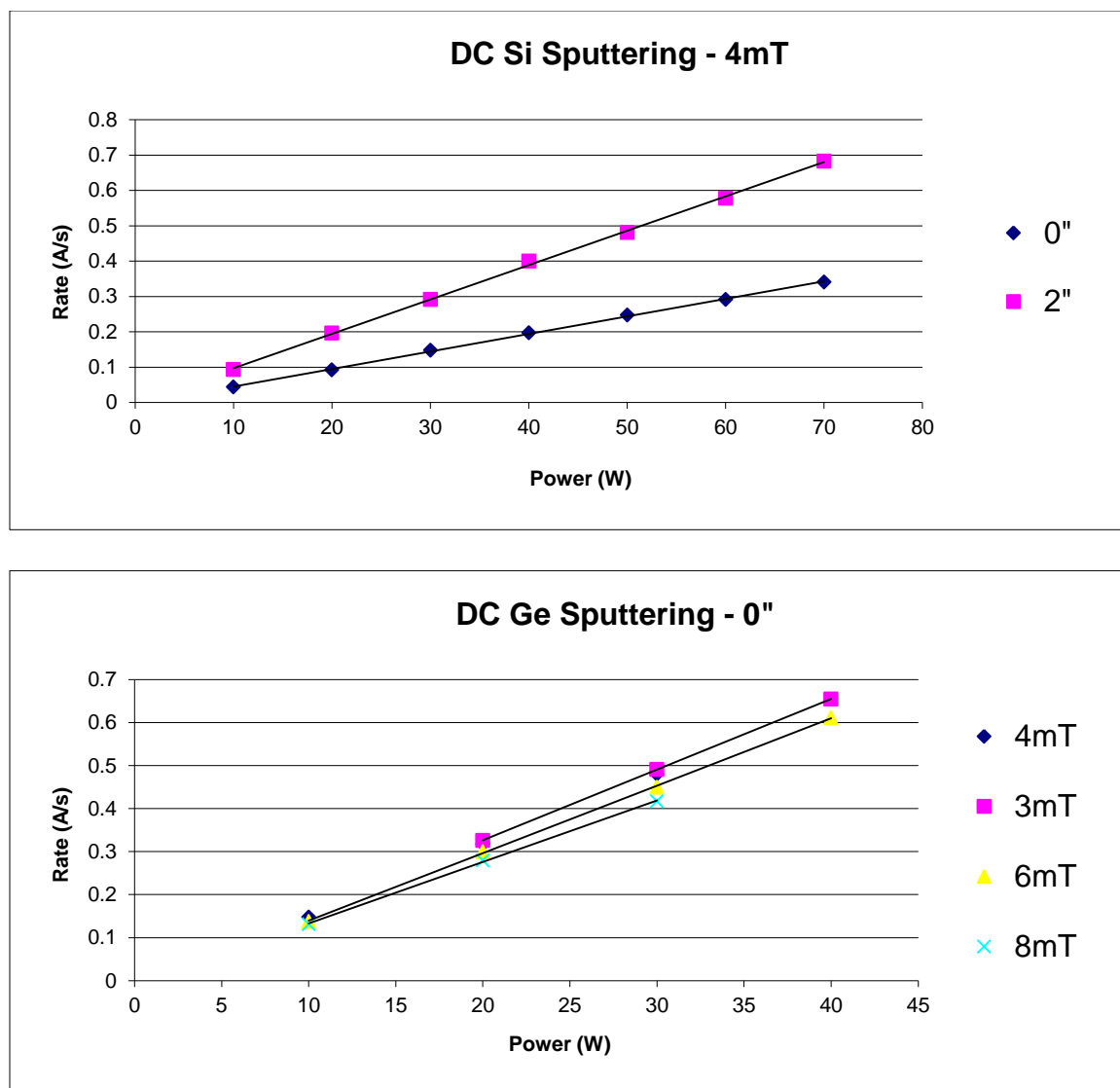
larger powers (and hence, sputtering yields).

Figure A2-1: (Top) Deposition rate from a Si target as a function of DC power. The two trend lines show linear behavior for each data set collected at different working distances. (Bottom) Deposition rate from a Ge target as a function of DC power. Trend lines show linear behavior for each data set collected at different working pressures.

The bottom panel of Figure A2-1 displays DC sputtering deposition rates for Ge for various Ar-process gas pressures. Like Si, the deposition rate of Ge is linear with power. Increased background pressures of Argon ultimately increase scattering and reduces the effective deposition rates. The effects of scattering are slightly enhanced for increased powers.

Ex situ SIMS calibration and impurity detection

We have also performed *ex-situ* secondary ion mass spectroscopy (SIMS) to extrapolate deposition rates and to detect low level impurity incorporation in our films. In the following depth profile (Figure A2-2) the Si and Ge signals have been removed to show detail in the impurity levels. Oxygen and carbon represent the greatest impurities, with especially high levels near the surface. These species are likely introduced into the film by forward recoil sputtering during the SIMS process. The total film thickness was 200 nm; profiling from 200-450 nm is into the substrate. There is a spike in B and Mo content at 200 nm which is surface contamination prior to growth.

Most importantly, we find that the metal (Fe, Ni, Mn, and Ta) contents are negligible throughout the film and the substrate. This indicates that we do not observe sputtering of the MBE tooling.
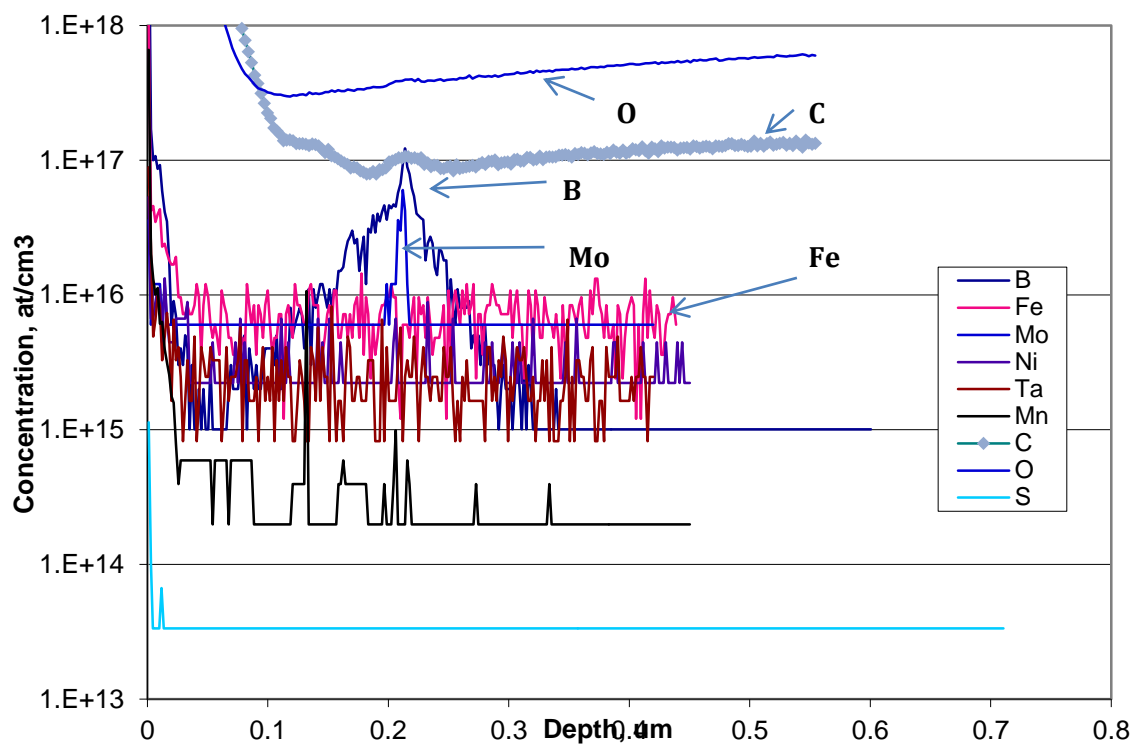
Figure A2-2: SIMS depth profile of a 200 nm SiGe film. The Si/Ge signals have been removed to investigate the impurity concentrations.

Appendix 3: Estimation of AFM error

Error calculations

The following schematic (Figure A3-1) describes the interaction of an AFM tip with a {111}-sidewall faceted island. Using the labeled dimensions one can calculate the volume of an example island and model the resulting observed island shape (bottom of Fig. A3-1). By comparing these island volumes one can determine a relationship for *volume error* as a function of island dimensions.
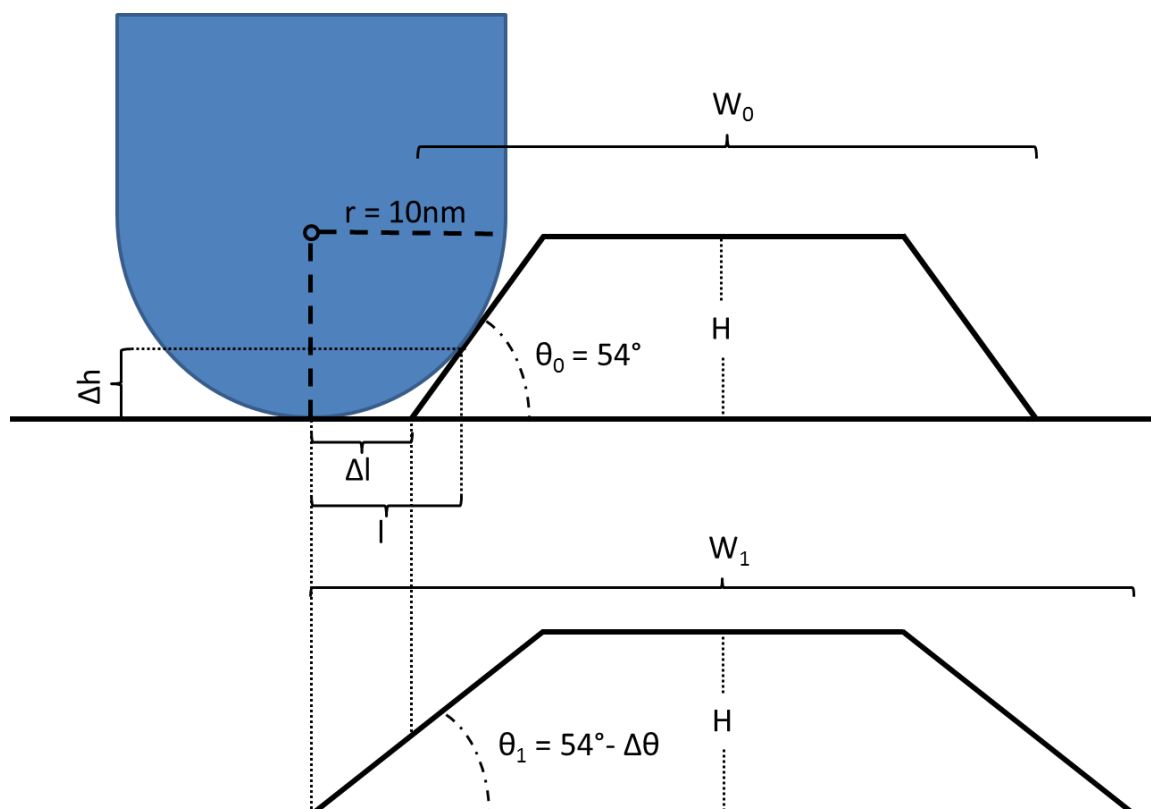
Figure A3-1: (Top) Schematic representation of the AFM tip interaction with a {111}-sidewall faceted island. (Bottom) The observed island profile when scanning will have more shallow sidewalls due to the finite radius of the AFM tip.

Volume error derivation

$$\sin \theta = \frac{l}{r}$$

$$l = r \cdot \sin \theta$$

$$\cos \theta = \frac{r - \Delta h}{r}$$

$$\Delta h = r - r \cdot \cos \theta$$

$$l - \Delta l = \frac{\Delta h}{\tan \theta}$$

$$\Delta l = r \cdot \sin \theta - \frac{r - r \cdot \cos \theta}{\tan \theta}$$

$$\Delta l = r \cdot \sin \theta - r \cdot \left(\frac{1}{\tan \theta} - \frac{\cos \theta}{\tan \theta}\right)$$

$$V_0 \approx H \cdot W_0{}^2 - 2 \cdot H \cdot L_0 \cdot W_0 - L^3$$

Next, we assume a fixed island height, H, for simplicity.

Then, use a range of W for numerical calculations.

$$\tan \theta_{0,1} = \frac{H}{L_{0,1}}$$

$$V_1 \approx H \cdot W_1{}^2 - 2 \cdot H \cdot L_1 \cdot W_1 - L^3$$

$$\Delta V \approx V_1 - V_0$$

Appendix 4: Topography post-processing of AFM data

```matlab
dir     = '\Chris\Contours_capping\';

% Edit only this file name (text file must be same as directory name)
name    = '052611_SK';

% Drop in the raw data into variable 'A'

A       = dlmread([dir,name,'/ ',name,'.txt']);

% spacing per pixel(A)-normalized to meters for Gwyddion output
d       = 19.569E-10;   %Use scan size / # pixels.

% spacing per pixel for 2D angle plot
e       = d/1E-10;

% effective "fractional flood plane".  Standard=0.12
lowest  = 0.10000;

% Use -A for NT-MDT output.  Occasionally an NT-MDT correction factor
is also used, see raw text file.
A       = A;

[n,m]   = size(A);
N       = zeros(n,m);
X       = N;

MAXA    = max(max(A));

% Calculating cross products at each pixel and determining the normal
vector.

fprintf('Start Cross Products and Finding Local Normals: ')

for i=2:n-1
    for j=2:m-1

        if ( (A(i,j)>(lowest*MAXA)) & (A(i+1,j)>(lowest*MAXA)) & (A(i-1,j)>(lowest*MAXA)) & (A(i,j+1)>(lowest*MAXA)) & (A(i,j-1)>(lowest*MAXA)))

            vec_1 = [2*d    0       (A(i+1,j) - A(i-1,j))];
            vec_2 = [0      2*d     (A(i,j+1) - A(i,j-1))];

            C       = cross(vec_1,vec_2);

            N(i,j) = acosd(dot([0 0 1],C)/norm(C)/norm([0 0 1]));

            C(3)    = 0;
```

```matlab
            X(i,j) = acosd(dot([1 0 0],C)/norm(C)/norm([1 0 0]));

        end

    end
end

fprintf('Linearizing Matrix Data: ')

N_1D    = zeros(n*m,1);
X_1D    = N_1D;

for i=1:n
    for j=1:m
        N_1D((i-1)*m+j)=N(i,j);
        X_1D((i-1)*m+j)=X(i,j);
    end
end

% Plot a histogram with '40' bins.

[n,x]=hist(N_1D,40);

n(1)=0;

figure
plot(x,n,'ro','markersize',5)
xlabel('Angle Normal to the Surface (deg)')
ylabel('Count')
print('-r600','-dpdf',[dir,name,'/',name,'_angle_40_bin.pdf'])

hista1 = [x' n'];
dlmwrite([dir,name,'\',name,'_hista1.txt'],hista1);

% Create a contour plot of the surface using the local surface angles

[n,m]    = size(A);

portion = 1;
levels = 50;

figure
contourf((0:(n/portion-1))*e, (0:(m/portion-1))*e,
N(1:(n/portion),1:(m/portion)),levels,'linestyle','none');
colormap(flipud(gray));
color = colorbar;
caxis([0, 20])
xlabel(color,'deg')
xlabel('Angstroms')
ylabel('Angstroms')
print('-r600','-dpdf',[dir,name,'/',name,'_angles.pdf'])
```

Appendix 5: Control of thermal interface conductance via roughening

Note: The following research was conducted in collaboration with Dr. Patrick Hopkins group in the UVA Department of Mechanical Engineering.

One of the largest untapped sources of energy is waste heat. In order to harvest this resource, significant interest has risen for a new class of materials known as thermoelectrics (TE's). TE materials are those that exhibit a voltage response to a temperature gradient. The earliest demonstration of this effect was by Thomas Seebeck, who found that when a junction of dissimilar materials is heated, a potential difference, ΔV, can be measured between the materials, which is proportional to the temperature change, ΔT. The Seebeck coefficient describes this relationship and is defined as: $S = -\Delta V / \Delta T$.

Later, Jean-Charles Peltier observed that heat can be carried by electrons during current flow through a material. Thus, heat may be absorbed or generated between two conductors where the heat flow, Q, is proportional to the electrical current, I, through the Peltier coefficient, $\pi = Q/I$. Furthermore, the Seebeck and Peltier coefficients may be connected through the Kelvin relationship for the absolute temperature, T: $T = \pi / S$. To further compare the efficiency of various thermoelectric materials, a dimensionless figure of merit, ZT, has been defined:

$$ZT = \frac{\pi S \sigma}{\kappa}$$

where σ and κ are the electrical and thermal conductivities of the material. This equation may be reduced to the more familiar form:

$$ZT = \frac{S^2 \sigma T}{\kappa}$$

The current state of the art has realized ZT of about 1 at room temperature for a few select materials, namely PbTe, Bi_2Te_3, and SiGe, which exhibit the greatest Seebeck coefficients. However, direct application of solid-state cooling and heating devices has failed due to the relatively high cost of materials as compared to conventional liquid coolants [155,156]. In order to compete, the efficiency (ZT) of solid-state thermoelectric materials must reach approximately 2.4.

Recently, Hicks and Dresselhaus suggested that by nanostructuring materials in one dimension, i.e. nanowires, one many significantly increase the effective ZT of the material [157]. The efficacy of such nanostructure is fundamentally based on the increase in interface density, which results in the perturbation and/or limitation of thermal conduction pathways. This new school of thought has drastically changed the way we think about thermoelectric materials and the research community is diving into clever methods for 0-D, 1-D, and 2D nanostructuring as a means to control κ.

One simple method to achieve large area two-dimensional nanostructures is via vertical superlattice (SL) growth. Owing to their compatibility (see Chapter 1), Si-Ge is an ideal material system for high crystalline quality SLs. Several works have investigated the thermal transport across Si-Ge SLs [158,159] and stacked QDs [160–163] all

demonstrating the feasibility of tuning thermal transport with SL period and QD areal density. However, the exact mechanism of phonon impedance at roughened SL interfaces is unclear.

In the present collaborative work with Prof. Patrick Hopkins, we have synthesized a series of samples exhibiting single QDs layers with variable size to investigate various interfacial scattering mechanisms, including: acoustic phonon mismatch, phonon localization and attenuation, and alteration of phonon dispersion relations [18,164]. The following key results are published in:

➢ P.E. Hopkins, et al. "Controlling thermal interface conductance through quantum dot roughening". *Phys. Rev. B.* **84**, 035438 (2011).

from which, Figure A5-1 and Figure A5-2 are borrowed with permission of the authors.

By tailoring the composition of a Ge_xSi_{1-x} film, the deposition thickness, and temperature, one may precisely control the size, shape and distribution of QD species at the film surface. Figure A5-1(a-f) and Table A5-1 show AFM scans and growth details for five different Ge_xSi_{1-x} QD surfaces (along with representative linescans) used for thermal transport measurements in this study.
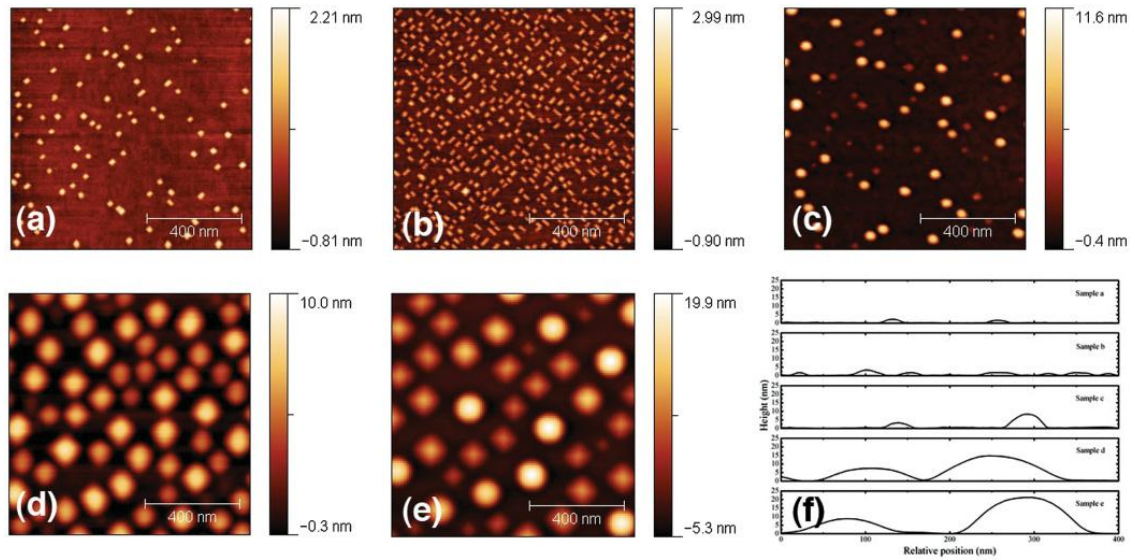
Figure A5-1: Atomic-force microscrope images and representative line scans of the QD roughened surfaces studied in this paper. These specific surfaces have rms roughnesses of (a) 0.28 nm from Ge QDs, (b) 0.53 nm from Ge QDs, (c) 1.38 nm from Ge QDs, (d) 2.16 nm from GeSi QDs, and (e) 4.46 nm from GeSi QDs. The representative line scans of each AFM are shown in (f). Further growth information is given in Table A5-1.

Table A5-1: Experimental growth parameters for QD surfaces shown in Figure A5-1.

Fig.	Features	Thickness (nm)	Growth Temp. (°C)	Growth Rate (nm s^{-1})	Density (QDs μm^{-2})	RMS Roughness nm
1a	Dilute Huts	0.70	550	0.010	96	0.28
1b	Dense Huts	0.85	550	0.010	590	0.53
1c	Huts/Domes	0.85	600	0.010	75	1.38
1d	Big Huts	2.60	740	0.017	55	2.16
1e	Huts/Domes	3.10	740	0.017	36	4.46

The interfacial thermal conductance of these surface is measured using time-domain thermal reflectance (TDTR) which has been thoroughly described elsewhere [165–168]. In brief, TDTR is a non-contact pump-probe technique wherein short optical pulses (~100 fs) deliver a heating event and subsequently measure the

temperature as a function of reflectivity. In the present study, the thermal conductivity is measured as a function of temperature for: $100K < T < 450K$. Numerical analysis is used to extract the QD interface component (h_k) of the total thermal conductivity, κ. Thermal boundary conductance of each QD surface is shown in Figure for measurements taken at 300K.
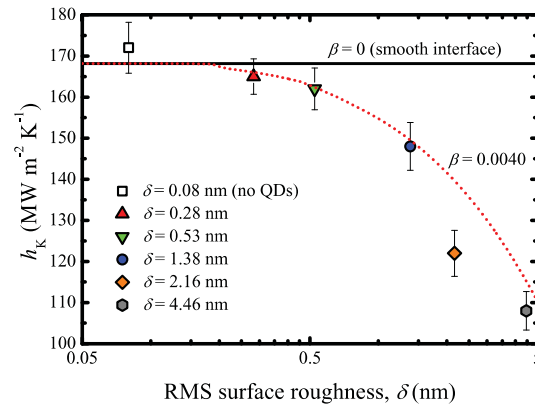

Figure A5-2: Thermal conductance as a function of RMS roughness across the series of structurally variant Al/Si interfaces at 300 K. Based on calculations by Hopkins, et al. [18], a single fitting parameter, $\beta = 0.0040$, for the phonon attenuation model shows good agreement with experimental data.

In general, the thermal boundary conductance at the Al – Ge QD interface is found to reduce with increasing QD size. Since the "flavors" of QDs vary with growth conditions, we directly compare the QD surface based on the general measurement of RMS roughness. Using analytical calculations based on the diffuse mismatch model and including a phonon-attenuation effect (details elsewhere [18]), one can lend insight into the mechanisms of interfacial phonon scattering. Based on simple fitting with this hybrid model, it is suggested that in addition to diffuse scattering at the Al/Si interface due to the multilayer vibrational mismatch, the phonons also experience local attenuation. The

reduction in heat transport is confined to a few-nanometer region at the interface suggesting that the phonons experience increased interfacial residency, e.g. confinement.

Ultimately, reduced thermal conductivity is observed with increased QD size. This implies that phonon confinement is achieved when the QD size approaches the phonon wavelength. The smallest interfacial QDs have no effect on interfacial transport since they are simply not "seen" by the phonons.